The Influence of Core Crystallization and Mantle Overturn on Ancient Dynamos

by

Aaron Lewis Scheinberg

Submitted to the Department of Earth, Atmospheric and Planetary Sciences
in partial fulfillment of the requirements for the degree of

Doctor of Philosophy in Planetary Science

at the

MASSACHUSETTS INSTITUTE OF TECHNOLOGY

June 2015

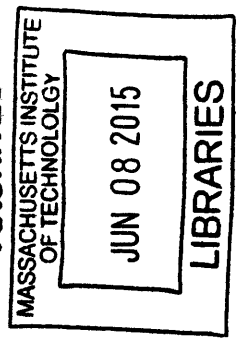

Signature redacted

Author .....
Department of Earth, Atmospheric and Planetary Sciences
May 21, 2015

Signature redacted

Certified by .....
Linda Elkins-Tanton
Director, School for Earth and Space Exploration
Arizona State University
Thesis Supervisor

Signature redacted

Accepted by .....
Robert van der Hilst
Schlumberger Professor of Earth Sciences
Department Head

The Influence of Core Crystallization and Mantle Overturn on Ancient Dynamos

by

Aaron Lewis Scheinberg

Submitted to the Department of Earth, Atmospheric and Planetary Sciences
on May 21, 2015, in partial fulfillment of the
requirements for the degree of
Doctor of Philosophy in Planetary Science

Abstract

This dissertation contributes to three unresolved problems in planetary science regarding potential dynamo action in asteroids, the Moon, and Mars. First, we examine the physical processes active during asteroid core crystallization. We model inward crystallization as well as crystal settling and the compaction of a possible cumulate inner core. We then explore the potential strength and longevity of a dynamo in the planetesimal's early history. We find that cumulate inner core solidification would be capable of sustaining a dynamo during the bulk of solidification, but that there may be insufficient power for a dynamo in an inward dendritic solidification scenario.

Next, we explore the origin of the magnetic field recorded in the lunar crust. Evidence suggests a core dynamo existed from 4.2 to 3.56 Ga, and possibly until near present day. Seismic measurements indicate the lunar core is partially solidified. Latent heat and concentrated light elements at the interface of a solidifying inner core could drive outer core convection. We demonstrate that core solidification can account for the observationally inferred duration of the lunar dynamo. However, it cannot explain the magnitude of the recorded magnetic field. A dynamo may also stop and restart due to heat flow fluctuations as convective vigor falls below the threshold for dynamo action.

Finally, we examine the early history of the Martian mantle. The solidification of a magma ocean may result in an unstable density profile prone to overturn. A long-wavelength instability could play a role in the stark contrasts observed between the northern and southern hemispheres of Mars, including the dichotomy in crustal thickness and magnetization. However, we find that cumulate overturn in the Martian scenario would likely have occurred with short wavelengths. In an isoviscous model, thermal convection ensues rapidly after overturn; however, when viscosity is temperature dependent, compositional stability suppresses the onset of convection.

Thesis Supervisor: Linda Elkins-Tanton
Title: Director, School for Earth and Space Exploration

Arizona State University

Prior Publication

The research presented in Chapter 4 was previously published in the Journal of Geophysical Research: Planets (Scheinberg et al., 2014). The research presented in Chapter 3 is in press with Icarus (Scheinberg et al., 2015b). The coauthors listed in those publications contributed to the development, direction, and interpretation of this work. The writing, modeling, and analysis presented in this dissertation was conducted by the author.

Acknowledgments

First and foremost I would like to acknowledge the unwavering support of my adviser, Lindy Elkins-Tanton. She has set an inspiring example for me as a scientist and as a human being. Many thanks also to my collaborators Gerald Schubert, Krista Soderlund, Shijie Zhong, and Dave Bercovici who were always there to consult with and ease my neuroses. Thanks to my thesis committee, Brad Hager, Ben Weiss, Gerald Schubert, and Rick Binzel, and to my generals committee, Taylor Perron, Brad Hager, Ben Weiss, Tom Herring, and Anthea Coster. I am thankful to Jack Wisdom for lending me his computational infrastructure.

Nothing would be possible without the administrative support of Brenda Carbone, Kerin Willis, Vicki McKenna, and Roberta Allard. They are all also just so caring and lovely to talk to when I need to get out of my head.

I cannot express my gratitude toward Frank Centinello, officemate and confidant of five years, for his extraordinary camaraderie and emotional support. Additional thanks for my fellow EAPS students' support, including but not limited to: Roger Fu, Stephanie Brown, Ben Black, Alex Evans, Jenny Suckale, Martina Coccia, Erin Shea, and Sonia Tikoo-Schantz. Thanks also to Nan Zhang, Matthieu Laneuville, and Maria Zuber for their help with the lunar project. And thanks to Rob van der Hilst for just being so darn friendly all the time.

My stay at MIT was extended by a year, partly due to a tentative venture into ionospheric physics. It was Lindy again who saw me through that experiment with resounding encouragement and wisdom. Advice from Tom Herring and Maita Schade on this question really helped bring clarity too.

I am glad that I was able to maintain a reasonably healthy social life while pursuing this degree. Thank you pika, for giving me a place to call home and helping me find a support network of fantastic friends, including (in order of appearance) Alorah Harman, Arathi Ramachandran, Galina Mamaliga, Kit Cali, Samira Daswani, Evan Lynch, Danny Manesh, and so many others! Thanks especially to Danny Clark for his friendship and his assistance in all things linux. We all had some amazing adventures

together and they are sure to continue. Thanks to anyone and everyone who called to check in on me. Yes, I am alive - and better still, I'm done with grad school. Last but certainly not least, I am beyond grateful for the constant encouragement and love from my family, Michael, Kathleen, Joe, Russell, and Miao Scheinberg. I like to think I have a good imagination, and I cannot imagine a better family to be a part of.

Contents

List of Figures

List of Tables

Chapter 1

Introduction

Planetary magnetism beyond Earth's own magnetic field was first confirmed in Jupiter when Burke and Franklin (1955) detected non-thermal radio emissions attributable to charged particles accelerating in a rotating magnetosphere. During the second half of the twentieth century, exploratory missions revealed that planetary magnetic fields were quite common and that the characteristics of each planet's magnetic field were remarkably diverse.

All four gas planets were found to possess an internally generated magnetic field. Of the terrestrial planets, only Mercury joins Earth in maintaining an observable internally generated field at present day (Connerney, 2007). It is believed that present-day heat transport out of Venus is too inefficient to drive the core convection necessary for magnetic field generation (Stevenson, 2003). Although no crustal remanent magnetization has been observed on Venus, it is possible that a magnetic field existed in the past and that any record of it was removed by a global resurfacing event (e.g., Strom et al., 1994).

Observations of remanent magnetization argue for the past existence of an internally produced magnetic field on Mars and the Moon despite the lack of such a field at present day. Constraints on the Martian magnetic history derive primarily from data collected by Mars Global Surveyor, which among other observations mapped the vector field of the local magnetic field across the surface (Connerney et al., 2005). The crustal magnetic anomalies of the Moon have also been mapped, most recently by

the Lunar Prospector (Mitchell et al., 2008) and SELENE (Tsunakawa et al., 2010). Additionally, samples returned to Earth by the Apollo missions provide information on the magnetic field dated to their formation (e.g., Wieczorek et al., 2006).

Similarly, the presence of magnetic fields recorded in meteoritic samples in early solar system history support the existence of internally driven dynamos even in some small early bodies (Scheinberg et al., 2015a). These small bodies (planetesimals) were the early building blocks of planets, some of which have survived, with varying degrees of structural damage, to present day as asteroids.

This dissertation investigates a set of open problems regarding the evolution of the paleofields that existed on planetesimals, the Moon, and Mars in early solar system history. We seek to better understand how these internally generated fields were powered, how conditions in the mantle affected them, and what influenced the timing of their initiation and led to their ultimate disappearance. A better understanding of the evolution of dynamo fields provides a context with which to interpret future observations, whether paleomagnetic, geochemical, or geophysical. Furthermore, increased understanding of these ancient geodynamos can in turn aid our understanding of and predictions for dynamos presently active in our solar system. It also informs modeling of potential exoplanetary dynamos as the accelerated pace of exoplanet discoveries in the present decade continues.

While these general dynamo questions constitute the unifying thread of this dissertation, we diverge substantially from this focus to investigate early planetary mantle dynamics. We explore scenarios for both the Moon and Mars in which energy of accretion and radiogenic heating contributed to the creation of a global magma ocean, which then solidified fractionally to form an unstable mantle density profile. Additionally, we explore models of core crystallization in the lunar and planetesimal cases. In the following section, we summarize the work presented in this thesis.

1.1 Summary of Thesis

For the remainder of Chapter 1, we focus on magnetism in planetesimals. First, we summarize magnetic field observations in meteorites and asteroids. Next, we discuss dynamo theory and modeling, and their application to planetesimals. We conclude with a discussion of alternative proposed explanations for meteorite magnetization.

In Chapter 2, we consider the viability of different proposed solidification scenarios in a molten metal planetesimal core. We suggest theoretical limitations on the ability of fractional core crystallization to proceed concentrically inward; dendritically inward; and by gradual accumulation of liquid-borne crystals into an inner core. We rule out concentric inward solidification. Then we use a finite-difference thermal model to examine the evolution and energetics in the remaining scenarios. We conclude that convection in an inward dendritic solidification scenario would have comparatively limited energy available to power a dynamo. The cumulate inner core scenario, on the other hand, could provide substantial energy to power a dynamo, although the field would be short-lived.

In Chapter 3, we examine the possibility that a compositionally driven core dynamo could explain the lunar paleomagnetic record. We use a finite-element mantle convection model coupled with a parameterized core model to investigate the longevity and magnitude of a thermochemical dynamo. We assume an initial mantle profile consistent with an overturned magma ocean cumulate. Although changes in physical properties such as mantle viscosity and core size do affect results, we find that thermochemical convection is not able to reproduce the magnetic field magnitudes reported by paleomagnetism studies. However, we find that dynamo longevity could be consistent with such a scenario. The timing is very sensitive to adiabatic heat flux, which is poorly constrained.

In Chapter 4, we depart from the focus on core modeling and more carefully study the mantle dynamics of an unstable density profile on Mars and the mantle's subsequent overturn. Using a finite-element mantle convection model, we determine the likely modes and timescales of instability for a selected parameter space. We

examine the hypothesis that a long-wavelength (degree-one) overturn event could occur. Such an event would impose hemispherically asymmetric heat flow boundary conditions on the core which could explain observed Martian crustal magnetization. We conclude that such an overturn event is unlikely.

In Chapter 5, we summarize the results of this work and suggest future topics of research.

1.2 Observations of Planetesimal Magnetism

1.2.1 Magnetic fields recorded in meteorites

As a ferromagnetic material cools below its Curie temperature, it records the ambient magnetic field. The discovery of paleomagnetism recorded in a variety of meteorite families and types suggests that strong magnetic fields, sufficiently stable to permit mineral magnetization, were common in early solar system bodies. Weiss et al. (2010) summarize the methodology and historical difficulty of interpreting meteoritic paleomagnetism. Here we summarize the latest and more definitive meteorite observations.

Meteorites are divided into two categories (of which there are many subdivisions): chondrites, which never underwent melting, and achondrites, which underwent at least partial melting. Remanent magnetization has been found in both chondritic and achondritic meteorites. The former is perhaps surprising. A dynamo field would have required large-scale melting in order to differentiate the body and form a conductive metal core capable of sustaining the field. Therefore, the parent body of a magnetized chondrite either underwent partial differentiation (melting only internally while leaving an unmelted outer shell), or was magnetized by an external mechanism. Alternate magnetization mechanisms are discussed in the final section of this chapter.

A remanent magnetic field, acquired in a field of > 20 μT, was observed in the carbonaceous chondrite Allende, both in bulk samples and in some chondrules (Carporzen et al., 2011). It likely was recorded only after accretion on the CV parent body since the ferromagnetic minerals in Allende, pyrrhotite, magnetite, and awaruite, were

probably produced by fluid-assisted metasomatism (Brearley and Krot, 2012). The magnetization also must have taken place after any significant heating, since substantial heating would have erased the remanent magnetization. Models suggest such heating would have subsided by 9-10 m.y. after CAI formation, suggesting a substantial magnetic field must have persisted in that time (Carporzen et al., 2011).

Angrites and howardite-eucrite-diogenite (HED) meteorites are two groups of basaltic achondrites that have been found to contain evidence of an early magnetic field. Three angrites have been found to record a field of $\sim$10 μT from 4564-4558 Ma (Weiss et al., 2008). Fu et al. (2012) determined that the Allan Hills A81001 eucrite meteorite recorded a field at 3.69 Ga of at least 2 μT. They suggested this magnetization occurred in the presence of a crustal remanent field that itself recorded a more ancient dynamo field. Although a potential parent body of the angrites has not yet been identified, HED meteorites have been tentatively associated with Vesta.

Fields have also been found in main group pallasites (Tarduno et al., 2012). Pallasites are stony-iron meteorites that consist of olivine in an iron-nickel matrix. They are typically believed to be samples of a planetesimal core-mantle boundary. However, it would be difficult for a core-mantle boundary to record a dynamo field. Due to the high thermal conductivity of iron, it would be difficult in a small body to have a core-mantle boundary near its Curie temperature and an active dynamo simultaneously, since the latter requires liquid metal. To explain the recorded fields, Tarduno et al. (2012) instead argue that the metal in pallasites originates from the core of an impactor which was injected into the mantle of a protoplanet.

Most recently, Bryson et al. (2015) derived a time-series paleomagnetic record for two main-group pallasite meteorites, Imilac and Esquel, assuming they originated somewhere in the mantle of the same body. They found a recorded magnetic field intensity of $119\pm12\mu$T and $131\pm13\mu$T for the former meteorite and a smaller intensity of $84\pm14\mu$T in the latter, with subsequent time periods recording lower field values.

1.2.2 Magnetic fields detected in asteroids

Considering the prevalence of magnetic fields in meteorites, it is likely that asteroids will also bear remanent magnetization from early solar system history. However, no such magnetization has been conclusively detected. When Deep Space 1 flew by 9969 Braille, a 0.78-km radius asteroid, it detected a 1-2 nT change from the ambient magnetic field at 28 km, but such a field was at the instrument's sensitivity limit and thus ambiguous (Kivelson et al., 1995; Richter et al., 2001). A possible magnetic field on 951 Gaspra was inferred from a Galileo flyby that detected a rotation in the magnetic field that could have been attributed to asteroidal magnetization. However, it could also be explained by solar wind alone (Blanco-Cano et al., 2003). Magnetic field measurements were also made during flybys of 21 Lutetia, 243 Ida, 433 Eros, and 2867 Steins, with no field detected (Acuña et al., 2002; Richter et al., 2012).

This lack of observed field could be explained by Runcorn's theorem. The theorem states that a uniform shell, magnetized from within by a centered field, will have zero external field once the original field is removed (Runcorn, 1975a,b). An asteroid that has avoided substantial disruption could thus be strongly magnetized even if this magnetization were undetectable. Parent bodies of meteorites could thus appear less magnetized at spatial scales larger than their meteoritic samples would suggest.

1.3 Planetesimal dynamos

1.3.1 Dynamo theory

A dynamo is a process that converts mechanical work produced by flow of an electrically conducting fluid into magnetic energy. The theory has been widely successful and is the commonly accepted explanation for the observed internally produced magnetic fields of stars and planets. The conducting fluid varies: plasma (for stars), metallic hydrogen (Jupiter and Saturn) (Russell, 1993), and water/ammonia/methane (Uranus and Neptune). In terrestrial planets and planetesimals, convection in a molten iron core is the most readily available explanation. However, the idea of a

silicate magma ocean dynamo has been proposed for Earth (Ziegler and Stegman, 2013). Porous volatile flow has also been considered as a source.

The field of magnetohydrodynamics (MHD) studies the behavior of such a system by considering Maxwell's equations, which describe the behavior of magnetic and electric fields, in tandem with equations describing conservation of momentum (the Navier-Stokes equations), mass, and energy in fluid flow. The time rate of change of the magnetic field $\vec{B}$ is described by the magnetic induction equation,

$$\left[\frac{\partial}{\partial t} + \vec{u} \cdot \nabla\right] \vec{B} = \lambda \nabla^2 \vec{B} + (\vec{B} \cdot \nabla)\vec{u} - \vec{B}(\nabla \cdot \vec{u}) \tag{1.1}$$

, where $\vec{u}$ is the velocity field and λ is the magnetic diffusivity. This equation can be derived by combining Maxwell's equations with Ohm's law in a moving reference frame and assuming displacement current is negligible. This assumption is accurate as long as fluid speeds are small compared to the speed of light. The left side of the equation is the material derivative of the field. The first term on the right side of the equation can be recognized as a diffusion term. The second and third terms are source terms accounting for the stretching of magnetic field lines due to fluid motion and the fluid's compressibility, respectively.

Using the magnetic induction equation, it can be shown that only certain fluid flow patterns (i.e., certain velocity field solutions) will support a magnetic field, while several of them cannot support a dynamo. Cowling (1934) presented, as the first of several "anti-dynamo" theorems, a proof that an axisymmetric magnetic field (such as a dipole) cannot be produced by an axisymmetric flow field. Therefore dynamos and the convection that drives them must be modeled in three dimensions rather than reducing the number of spatial dimensions; and resulting solutions to the equation are necessarily complex.

Not every flow field capable of producing a dynamo is also physical. The flow field is contained by equations describing conservation of momentum (the Navier-Stokes equations) and conservation of mass:

$$\rho\left[\frac{\partial}{\partial t}+\vec{u}\cdot\nabla\right]\vec{u}=-\nabla p+\frac{1}{\mu_0}(\nabla\times\vec{B})\times\vec{B}+\mu\nabla^2\vec{u}+\frac{1}{3}\mu\nabla(\nabla\cdot\vec{u})+\rho\vec{g}-2\rho\vec{\Omega}\times\vec{u} \quad (1.2)$$

$$\frac{\partial\rho}{\partial t}+\nabla\cdot(\rho\vec{u})=0 \quad (1.3)$$

where ρ is fluid density, p is pressure, μ_0 is the permeability of free space, μ is the dynamic viscosity, $\vec{g}$ is gravitational acceleration, and Ω is the body's angular velocity. The left side of the equation is the advective time derivative of the velocity. The terms on the right hand side represent, from left to right, pressure, Lorentz forces, viscous forces, buoyancy forces, and the Coriolis force. Under the Boussinesq approximation, ρ is assumed constant except in the buoyancy term. In a thermally-driven dynamo, buoyancy is due to thermal expansivity. The temperature field of the fluid is governed by:

$$\frac{\partial T}{\partial t}+\vec{u}\cdot\nabla T=\kappa\nabla^2T+\epsilon \quad (1.4)$$

where T is temperature, κ is thermal diffusivity, and ϵ is any volumetric temperature source or sink. Together, these four equations govern a convection-driven dynamo.

When the equations are nondimensionalized, four dimensionless parameters emerge that describe the system. A Rayleigh number, $Ra = \alpha g_0 \Delta T L/\nu\Omega$, compares the strength of buoyancy forces to viscous and Coriolis forces, where α is thermal expansivity, g_0 is a reference gravitational acceleration, ΔT is the temperature contrast across the fluid, L is the characteristic length-scale of convection, and ν is kinematic viscosity. The Ekman number, $E = \nu/\Omega L^2$, compares viscous to Coriolis forces. The Prandtl number, $Pr = \nu/\kappa$, compares momentum diffusion to thermal diffusion, and the magnetic Prandtl number, $Pm = \nu/\lambda$, compares momentum diffusion to magnetic diffusion.

1.3.2 Methods

Most numerical models of dynamos solve the above equations in a spectral framework. The unknown vector fields $\vec{B}$ and $\vec{u}$ are divided into toroidal and poloidal components, which allows them to be expressed in terms of scalar potential fields. These scalar potentials, along with the temperature field, T, are then laterally decomposed into spherical harmonic functions. These functions are orthogonal and their derivatives can be expressed analytically, allowing for the equations to be solved independently for each of them. In purely spectral codes, the radial component is also decomposed spectrally (Bullard and Gellman, 1954); however it was found more efficient to employ a "pseudospectral" method in which the radial component is solved locally with a finite difference method (e.g., Glatzmeier and Roberts, 1995).

Increasing availability of computational resources has allowed for finite-element dynamo modeling to become feasible (Chan et al., 2007; Zhan et al., 2011). In this scheme, a model core is divided into volumetric elements that are evaluated locally. This method allows for more parallelization since each element needs to communicate only with neighboring elements. Additionally, it does not require the computationally expensive conversions into and out of frequency space necessary for the pseudospectral method (Christensen and Wicht, 2007).

Numerical models are not capable of fully resolving core fluid motion for the dimensionless parameter values typically found in cores. Dynamo models are thus operated in an unrealistic parameter space. The Ekman number and magnetic Prandtl number attainable by numerical models are at least 8 and 4 orders of magnitude larger than their estimated physical values (Christensen and Wicht, 2007). In effect, a much larger viscosity is assumed in numerical models, which ignores the possible impact of small scale velocity field features.

Quite often, studies are concerned only with estimating the order of magnitude of a dynamo's magnetic field. This aim can be achieved by scaling estimates that forego the need for complex fluid dynamical modeling. This method typically relates total magnetic energy density to the energy density thermodynamically available to power

a dynamo:

$$\frac{B^2}{2\mu_0} \propto f_{ohm}\frac{L}{U}\phi \tag{1.5}$$

Here, B is the magnetic field magnitude within the core and f_{ohm} is the fraction of energy converted to magnetic energy and lost by ohmic dissipation. U is its characteristic velocity so that L/U represents the convective timescale. ϕ is the volumetric thermodynamically available power which can be determined from the thermal and composition buoyancy that may be driving convection. U is a more difficult parameter to constrain, since the characteristic velocity depends on which terms in the momentum equation are dominant. Various formulations are used in the literature. The constant of proportionality relating the two sides of the equation is estimated based on observation of known planetary fields and on dynamo modeling (Christensen, 2010).

In the present dissertation, we are only interested in field magnitude and duration and thus employ scaling laws rather than solving a full dynamo problem.

1.3.3 Planetesimal dynamos

Study of planetesimal dynamos in particular has been limited (Nimmo, 2009; Elkins-Tanton et al., 2011a; Sterenborg and Crowley, 2013; Bryson et al., 2015). They typically employ a scaling law to evaluate field magnitude. To evaluate longevity, they assume a critical magnetic Reynolds number, a critical core heat flux, or both. The magnetic Reynolds number is defined by $Re_m = UL/\lambda$. A critical threshold Re_m must be reached for there to be sufficient convective vigor to maintain a dynamo. Studies have placed this value variously from 10 to 100 (Christensen et al., 1999; Stevenson, 2003; Monteux et al., 2011). For purely thermal convection, total core heat flux must exceed adiabatic heat flux.

Nimmo (2009) examined the energetics of asteroidal cores and evaluated the minimum cooling rate required to produce a dynamo. He found that for purely thermal convection, production of a stable magnetic field would require a cooling rate of 1-100

K m.y.$^{-1}$. He also examined the effect of core solidification assuming an Earth-like inner core growing concentrically outward and enriching the liquid near the inner-core boundary in incompatible light elements. Such a core could produce a dynamo if cooling rates exceeded ~0.001-0.1 K m.y.$^{-1}$ - a heat flow one thousand times lower than that required to sustain a thermal dynamo. Further, he found that under these conditions a core greater than 50-150 km in radius would have a sufficiently high Re_m to support a dynamo. This calculation used a conservative threshold value for dynamo action, requiring that $Re_m > 100 - 1000$.

Elkins-Tanton et al. (2011a) investigated the conditions under which core heat flux in small bodies sufficed to produce a dynamo. They examined bodies from 50-500 km in radius, assuming a core radius at most half of the total radius, and determined core heat flux as a function of time, accounting for energy from accretion and ^{26}Al radiogenic heating in the mantle. They found that cores over ~50-100 km in radius would have had sufficient core heat flux to power a dynamo for more than 10 m.y.

Sterenborg and Crowley (2013) modeled the thermal evolution of a planetesimal with a convecting mantle and evaluated the potential for dynamo action assuming thermally driven convection (i.e., no core solidification). The magnetic Reynolds number was found to be the limiting factor. They used a critical Re_m of 10-100 and found that core convection in bodies smaller than ~500 km in radius could only produce a dynamo for less than 10 m.y.

1.4 Alternative magnetization mechanisms

A core dynamo is not the only proposed mechanism to explain the observed magnetization in meteorites. One proposed external origin is the solar magnetic field during the active T-Tauri phase (e.g., Cournede et al., 2015). However, such a field would only have a magnitude of 0.001-0.01 μT (Weiss and Elkins-Tanton, 2013). Crutcher (2012), however, predict a field of ~10 μT during gravitational collapse of the solar system's parent molecular cloud. Fu et al. (2014) reported the magnetization of chondrules in the Semarkona meteorite in a magnetic field of 5-54 μT. Since this mag-

netization predates accretion, it could only have formed in a solar nebula magnetic field.

Fu and Weiss (2012) discuss the possibility of detrital remanent magnetization in the solar nebula magnetic field. In this scenario, strongly ferromagnetic material can reorient itself to align with the local magnetic field as it accretes, reinforcing the field, rather than settling in a random orientation such that magnetization cancels locally. This magnetization mechanism could only function if its timescale is short compared to the frequency of disruptive processes.

Bland et al. (2014) examined effects of impacted-induced compaction on the temperature and pressure of chondritic material. They found that the temperature of the matrix in such an event would experience rapid heating before cooling within tens of seconds to the material's average temperature. Considering that impact-generated magnetic fields likely persisted for minutes, they concluded that it would be possible for the matrix of chondritic material to record an impact-generated field.

Measured cooling rates on the angrite Angra dos Reis suggest the body required thousands of years near its Curie temperature, requiring a stable field through this period to explain the magnetization observed (Weiss et al., 2008). This meteorite is too young to be explained by solar nebula fields. A dynamo is the more plausible explanation since dynamo fields could persist on timescales from several m.y. (Sterenborg and Crowley, 2013) up to 200 m.y. (Elkins-Tanton et al., 2011a; Tarduno et al., 2012; Weiss et al., 2008). The same requirement of a stable field makes a core dynamo the most plausible explanation for Allende's observed magnetization as well.

In this chapter, we introduced the topics of this dissertation and summarized current magnetic evidence in meteorites and asteroids. We described dynamo theory in general, numerical methods, and the recent applications to planetesimals. In the following chapter, we examine the magnetic and structural implications of a core in which crystallization occurs at the core-mantle boundary.

Chapter 2

Core solidification and dynamo evolution in a mantle-stripped planetesimal

Abstract

The physical processes active during the crystallization of a low-pressure, low-gravity planetesimal core are poorly understood but have implications for asteroidal magnetic fields and large-scale asteroidal structure. We consider a core with only a thin silicate shell, which could be analogous to some M-type asteroids including Psyche, and use a parameterized thermal model to predict a solidification timeline and the resulting chemical profile upon complete solidification. We then explore the potential strength and longevity of a dynamo in the planetesimal's early history. We find that cumulate inner core solidification would be capable of sustaining a dynamo during solidification, but less power would be available for a dynamo in an inward dendritic solidification scenario. We also model and suggest limits on crystal settling and compaction of a possible cumulate inner core.

2.1 Introduction

Planetesimals were the building blocks of the terrestrial planets. As the remnants of planetesimals that did not accrete into planets, asteroids provide a direct look into the origins of the solar system. Asteroids and the iron meteorites that derived from them are also a window into planetary cores including our own, which are rendered

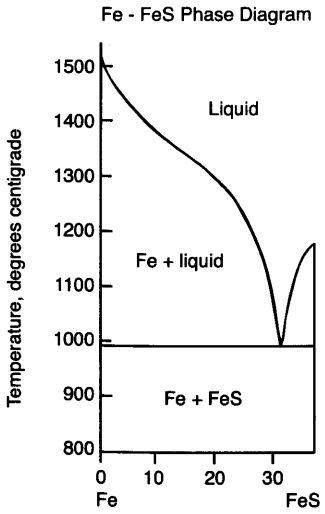

Figure 2-1: Phase diagram for the Fe-S system. As the liquid becomes enriched in sulfur, its solidus temperature decreases.

inaccessible to direct observation by thousands of kilometers of silicate mantle. Study of the early solar system will also influence our understanding of how different solar systems and their exoplanets may be similar or differ from ours.

In sufficiently large bodies, heating due to accretion and radioactive decay caused differentiation into a mantle and core by allowing relatively dense elements (predominantly iron) to sink to the center. These molten cores then solidified during subsequent cooling. The presence of sulfur, which has been inferred to range from 1 wt.% in the IVB parental core to 17 wt.% in the IIAB parental core (Chabot, 2004), would have slowed the solidification process. Melting temperature decreases substantially with sulfur content, dropping from 1811 K for pure iron to 1261 K at the Fe-S eutectic at 31 wt.% S (Fig. 2-1). Sulfur is incompatible with the crystallizing iron, so as crystallization proceeds, the residual melt is continually enriched in sulfur until it reaches the Fe-S eutectic, after which both solid iron and FeS (troilite) will form. Therefore significant secular cooling must have occurred during the solidification process. While solid iron is denser than the liquid, troilite is buoyant with respect to the expected liquid metal mixture and will thus will float to the top of a liquid core.

Pressures are much lower in planetesimals than in planets: the center of a 100-km metal body would be at $\sim$100 MPa. The solidus temperature increases with pressure,

but so does the temperature gradient of an adiabatically convecting liquid. In cores subjected to high pressures, the liquid temperature profile will first intersect its solidus at the planetary center, forming a solid inner core. Williams (2009) found that in bodies with core pressures less than 4 GPa, the adiabat is steeper than the solidus, suggesting that a cooling planetesimal core will reach its solidus at the core mantle boundary. We therefore expect crystals to nucleate at the core mantle boundary in a rapidly convecting system.

Iron meteorites can also provide information on the cooling rate experienced after solidification. Yang et al. (2008) examined several irons in the IVA meteorite family and found a large range of cooling rates within the body. They found a rate of ~6600 K m.y.$^{-1}$ at 7.57 wt.% Ni and ~100 K m.y.$^{-1}$ at 9.54 wt.% Ni while at 400-700 °C, the temperature range over which the Widmanstätten pattern forms. Since Ni content in the solid phase increases as fractional crystallization proceeds, the negative correlation of Ni concentration with cooling rate implies that solidification proceeded from the outside in. Yang et al. (2008) suggest that a 100-200 km body with a 1 km thick crust and 3-9 wt% sulfur would be consistent with the IVA parent body, and note that other iron meteorite families have similarly large cooling rate ranges.

On the other hand, Yang et al. (2010) found that nickel fraction correlated positively with cooling rate in IVB meteorites, suggesting the IVB parent body solidified outward. Cooling rates varied from 475 K m.y.$^{-1}$ for low-Ni (15.5 wt.%) meteorites to 5000 K for high-Ni (17.5 wt.%) meteorites. Both inward and outward solidification are thus possible scenarios for mantle-less core, although the authors propose that the core solidified while a silicate mantle was still present and that only after significant solidification was the mantle stripped away by an impact.

In some cases meteorites can provide gravitational orientation. The Cape York meteorite Agpalilik consisted of a single austenite crystal over 200 cm in diameter (Buchwald, 1971). Chromite and phosphate crystals in troilite inclusions in Agpalilik are always found at the same end, presumably due to buoyancy in a gravity field while the inclusion was liquid. A component of the inferred gravity field at the time of the troilite's solidification was perpendicular to the direction of crystal growth,

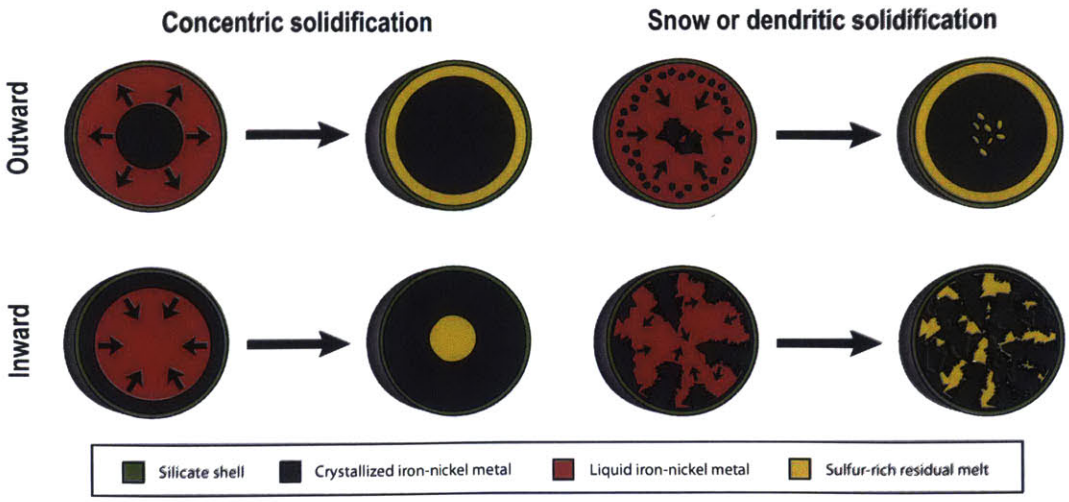

Figure 2-2: Four possible core solidification scenarios and their resulting end-states. (Top left) Concentric outward (Earth-like) solidification. (Top right) Solid inner core growth from accumulated iron "snow" and/or destabilized dendrites. (Bottom left) Concentric inward solidification. (Bottom right) Dendritic inward solidification.

suggesting that, at least locally, core solidification did not always proceed strictly outward or inward (Buchwald, 1975).

Haack and Scott (1992) distinguished between several modes of crystallization. They considered inward and outward crystallization proceeding both concentrically and dendritically. They conclude that inward dendritic solidification is most likely, although they note the possibility that crystals may form in the liquid and sink to form a cumulate inner core. Figure 2-2 shows a schematic of core crystallization scenarios.

Meteorites can provide information on the magnetic field present in the environment of the parent body when the material cooled below its Curie temperature. Study of the eucrite Allan Hills A81001 suggests the existence of an early core dynamo on Vesta (Fu et al., 2012). Iron meteorites are also capable of recording a magnetic field; however, this would require that iron at some depth be passing below its Curie temperature (1043 K) while convecting molten iron drives a dynamo beneath. Bryson et al. (2015) found remanent magnetization in two pallasites recording a field peaking at 131 ± 13 μT.

Several recent studies have modeled potential dynamo action in a planetesimal

core. Nimmo (2009) assessed the energetics of an asteroidal core dynamo assuming outward (Earth-like) core solidification. He found that the compositional buoyancy due to light element release during solidification reduced by three orders of magnitude the core cooling rate necessary to sustain a dynamo. They found that core convection in a body with core radius 50-150 km could drive a dynamo. Similarly, Elkins-Tanton et al. (2011a) found that core heat flow in bodies of radius as small as ~100 km was sufficient to sustain a dynamo for over 10 m.y and and for over 50 m.y. in bodies of radius ~300 km. However, an analysis by Sterenborg and Crowley (2013) found that core convection in bodies smaller than ~500 km in radius quickly fell below the critical magnetic Reynolds number necessary for dynamo action, and would only be capable of producing a weak dynamo for less than 10 m.y. Bryson et al. (2015) also modeled a planetesimal dynamo solidifying from the inside out. However, no work has yet been done examining the potential for dynamo action in an inwardly solidifying core. Nor has any work specifically modeled solidification and dynamo fields in a mantle-stripped planetesimal.

In the present study, we consider two scenarios in which solidification occurs near the core-mantle boundary (CMB). In the first scenario, newly solidified material is attached to the overlying silicate shell and that a solidification front proceeds downward concentrically or dendritically. In the second scenario, crystals form near but unattached to the CMB, settle out of the convecting liquid, and compact into a cumulate inner core. We use scaling analysis and a finite difference thermochemical core model with parameterized convection to 1) evaluate the dominant physical processes during planetesimal core solidification; 2) determine the characteristics of a planetesimal dynamo during solidification; and 3) determine the physical structure, mineral assemblage, and magnetization we could expect to find in asteroidal cores.

As a reference scenario, we examine a hypothetical planetesimal with an initially liquid core of radius 100 km whose mantle was stripped off in a grazing collision, leaving a 1 km silicate shell. Such a planetesimal would bear similarities to the IVA parent body described above and to (16) Psyche, the largest M-type asteroid. In all cases, we assume that solidification occurs at or near the upper boundary of the liquid

core. We also assume a simplistic liquid composition of pure Fe-FeS.

We define the outer-core boundary (OCB) as the upper boundary of the purely liquid convecting core region. Before solidification begins, this boundary is therefore equivalent to the core-mantle boundary (CMB). When inward solidification proceeds, the OCB refers to the lowest depth reached by dendrites. The inner-core boundary (ICB) refers to the bottom boundary of the purely liquid convecting core region, which is equivalent to the core's center if solidification is inward. The CMB, OCB, and ICB are located at radius R_c, R_o, and R_i, respectively.

2.2 Limitations on inward fractional solidification

We begin by examining the processes involved in inward fractional crystallization. Such fractionation almost certainly requires a well-mixed liquid reservoir beneath the solidification front. Therefore, the vigor of convection in the liquid core is critical to the system's evolution. If convection is sufficiently energetic, then the liquid will be chemically well-mixed and adiabatic, causing solidification to occur primarily at the upper boundary layer of the liquid where its solidus and thermal profile intersect. Following Haack and Scott (1992), we use a heat flux formulation to estimate the Rayleigh number, which describes convective vigor by comparing buoyancy forces to viscous forces: $Ra = g_0 \alpha q R_c^4 / \mu_l \kappa_c^2 c_P$, where g_0, α, μ_l and κ_c, and c_P are gravity at R_c, thermal expansivity, dynamic viscosity, thermal diffusivity, and specific heat capacity, respectively. (Parameters and their values are listed in Table 1.) Heat flux q out of the liquid is limited by the ability of the overlying solid material to conduct heat. In a spherically symmetric scenario, heat flux is thus given by:

$$q = -k \frac{\partial T}{\partial r} \tag{2.1}$$

where k is thermal conductivity and r is radius. Assuming a linear conductive profile across the thin silicate shell, heat flux at the onset of solidification is given by $q \approx k_m \Delta T / m = 6$ W m^{-2}, where k_m is the thermal conductivity of the silicate shell, ΔT is the temperature difference across the shell, and m is the shell's thickness. The

Fixed parameters	Description	Value	Unit
R_c	Core radius	100	km
m	Silicate shell thickness	1	km
k_m	Shell thermal conductivity	4	W K^{-1} m^{-1}
T_0	Initial temperature	1820	K
T_{surf}	Surface temperature	250	K
Material constants	Description	Value	Unit
ρ_{Fe}	Density, solid	7500	kg m^{-3}
ρ_l	Density, liquid[1]	7020	kg m^{-3}
β	Density parameter[2]	$1340 + 81.5\chi$	kg m^{-3} (wt.% S)$^{-1}$
μ_s	Viscosity, solid[3]	$1{\cdot}10^{13}$	Pa s
μ_l	Viscosity, liquid[4]	$1{\cdot}10^{-2}$	Pa s
c_P	Specific heat capacity, Fe[5]	835	J kg^{-1} K^{-1}
α	Thermal expansivity, liquid Fe[6]	$9.2{\cdot}10^{-5}$	K^{-1}
k_c	Thermal conductivity, solid Fe[7]	30	W K^{-1} m^{-1}
k_l	Thermal conductivity, liquid Fe[7]	40	W K^{-1} m^{-1}
κ_l	Thermal diffusivity, liquid Fe	$k_l/\rho_l c_P$	m^2 s^{-1}
L_{Fe}	Heat of fusion, iron[8]	$2.56{\cdot}10^5$	J kg^{-1}
L_{FeS}	Heat of fusion, troilite[9]	$1.33{\cdot}10^5$	J kg^{-1}
D_S	Sulfur diffusivity[10]	$5 \cdot 10^{-9}$	m^2 s^{-1}

Table 2.1: Parameters used in this study. [1]Anderson and Ahrens (1994); [2]Nishida et al. (2008); [3]Van Orman (2004); [4]Dobson et al. (2000); [5]Desai (1986); [6]Anderson and Ahrens (1994); [7]Touloukian et al. (1971); [8]Young (1991); [9]Fulton (1910); [10]Alfe and Gillan (1998)

resulting Rayleigh number of order $Ra \sim 10^{25}$ is more than sufficient for convection that occurs in spherical geometry above $Ra \sim 10^4$ (Zebib et al., 1983). On the other hand, as discussed in Section 2.3.1, if crystal fraction within the liquid later reduces effective viscosity, the decline in Rayleigh number would be self-enforcing since the resulting lower Rayleigh number would allow more crystallization within the liquid.

2.2.1 Crystallization

We treat solidification as the Stefan problem to derive an estimate of the maximum solidification rate. This maximum rate will occur at the onset of solidification since at that time the temperature contrast is highest and the conductive shell is thinnest. Latent heat of fusion of iron, L_{Fe}, must be removed for solidification to progress. Assuming all energy lost to conduction is latent heat, we obtain:

$$\rho_{Fe} L_{Fe} w = q A_c \tag{2.2}$$

where ρ_{Fe} is the density of solid iron, w is the volumetric rate of crystallization, $A_c = 4\pi R_c^2$ is the area of the core-mantle boundary. We thus find an upper limit on crystallization rate of $w \approx 12$ km^3 yr^{-1}. If solidification occurs from the outside in as a spherically symmetric growth front with no trapped liquid, the front would progress inward at a rate of 100 mm yr^{-1}. This is a high estimate since it ignores secular cooling by assuming all of the energy removed to the surface is latent heat.

2.2.2 The chemical diffusion timescale

To maintain a concentric inward crystallization growth front, sulfur excluded from the solid crystal structure must have time to diffuse away and thereby allow the nucleation of additional iron on the growth plane. The removal of sulfur is especially crucial because of its effect on the solidification temperature, with a decrease of some 20 K for every percent increase in sulfur. Latent heat must also be conducted away; however, due to iron's relatively high thermal diffusivity ($7 \cdot 10^{-6}$ m^2 s^{-1}), chemical diffusion is the limiting factor. Diffusion of sulfur in an FeS liquid has been estimated at $D_S = 5 \cdot 10^{-9}$ m^2 s^{-1} (Alfe and Gillan, 1998).

The diffusion gradient determines the mass flux toward the interface according to Fick's first law:

$$J = D_S \rho_l \frac{\partial \chi(r)}{\partial r}. \tag{2.3}$$

where J is the mass flux of sulfur and ρ_l is the density of the liquid core. $\chi(r)$ is the sulfur fraction of the liquid by weight. We define χ_l as the sulfur content within the well-mixed liquid. Near the solid interface, $\chi(r)$ exceeds this value. If the solidification front is at radius R_o and is progressing downward with speed $|\dot{R}_o|$, then the sulfur mass flux necessary for crystal growth is $J > \chi_l(1-f)\rho_l|\dot{R}_o|$, where we allow for a fraction f of the sulfur to become trapped in the solid. The solidification rate is therefore bounded by:

$$|\dot{R}_o| < \frac{D_S}{\chi_l(1-f)}\frac{\partial \chi}{\partial r}. \tag{2.4}$$

The concentration gradient, $\partial\chi/\partial r$, can be bounded because the gradient in sulfur content produces an associated gradient in solidus temperature. If the gradient in solidus temperature exceeds the thermal diffusive profile of the boundary layer, then solidification would occur away from the interface, under the reasonable assumption that sufficient impurities in the liquid are available to act as nucleation sites. Solidification at the interface therefore requires that

$$\frac{\partial T_s}{\partial r} > \frac{\partial T}{\partial r}. \tag{2.5}$$

Using Eq. (2.1) and the fact that

$$\frac{\partial T_s}{\partial r} = T_s'(\chi)\frac{\partial \chi}{\partial r} \tag{2.6}$$

where $T_s'(\chi) = \partial T_s/\partial\chi$, we find:

$$\frac{\partial \chi}{\partial r} < -\frac{q}{kT_s'(\chi)}. \tag{2.7}$$

Substituting this result into Eq. (2.4), we find the solidification rate is bounded by:

$$|\dot{R}_o| < -\frac{D_S q}{\chi_l(1-f)kT_s'(\chi)}. \tag{2.8}$$

Note that this expression does not depend on boundary layer thickness and is thus independent of convective vigor. For $q = 6$ W m^{-2} and $\chi_l = 3$ wt.%, we find a maximum inward growth rate of only $|\dot{R}_o| = 0.4$ mm yr^{-1} if all sulfur is excluded from the solidification front, i.e. $f = 0$.

This simple analysis does not address the possibility of sulfur being removed from a non-horizontal growth plane by buoyancy-driven advection and thus does not eliminate the possibility of large-scale dendritic growth.

2.2.3 Sulfur remixing and dendritic growth

If fractional crystallization is proceeding from the outside in, then secular cooling in the liquid beneath the solidification front is the only driver for convection. In order to maintain a well-mixed liquid inner core, there must be sufficient thermodynamically available convective power, Φ_o, to entrain the sulfur being excluded from the crystallizing solid at the solidification front. In equation form,

$$\Phi_o > \Phi_S \tag{2.9}$$

where Φ_S is the power required to remix sulfur uniformly throughout the remaining liquid.

Following Buffett et al. (1996), the thermodynamically available power can be expressed as:

$$\Phi_o = \frac{\alpha(Q_o - Q_{ad})}{c_P}\left[\psi(R_o) - \bar{\psi}\right] \tag{2.10}$$

where Q_o is outer-core boundary heat flow. $\psi(r)$ is the gravitational potential at radius r and $\bar{\psi}$ is the average gravitational potential in the liquid core. The gravitational potential difference terms therefore represent the change in gravitational potential during remixing. $Q_{ad} = 16\pi^2 G\rho_l \alpha T_l k_l R_c^3/3c_P$ is adiabatic heat flow out of the outer-core boundary, where T_l and k_l are the temperature and thermal conductivity of the liquid core, respectively. We neglect adiabatic heat flow here since $Q_{ad}/Q_o \sim 0.1\%$. The energy leaving the liquid inner core, Q_o, is due solely to secular cooling, i.e.,

$$Q_o = V_o \rho_l c_P \frac{\partial T}{\partial t} \tag{2.11}$$

where V_o is the volume beneath the inward solidification front. Since the liquid temperature is just near its solidus, $T = T_s(\chi_l)$ and therefore

$$Q_o = V_o \rho_l c_P \frac{\partial T_s}{\partial \chi_l}\frac{\partial \chi_l}{\partial V_o}\frac{\partial V_o}{\partial t} = V_o \rho_l c_P T_s' \frac{\partial \chi_l}{\partial V_o}\dot{V}_o \tag{2.12}$$

where $T_s' = \partial T_s / \partial \chi_l$ and $\dot{V}_o$ is the time rate of change of V_o. In a solidification front with no trapped liquid, $\dot{V}_o = -w$, where w is the volumetric rate of crystallization. If instead a fraction f_t of the solidification front remains liquid, then $\dot{V}_o = -w/(1 - f_t)$. χ_l can be expressed as

$$\chi_l(V_o)V_o = \chi_0 V_c - \int_V^{V_c} f(V_o)\chi_l(V_o)dv \tag{2.13}$$

where V_c and χ_0 are the total core volume and initial sulfur content, respectively. Applying $\partial/\partial V_o$ to both sides and rearranging, we find

$$\frac{\partial \chi_l}{\partial V_o} = -\frac{\chi_l}{V_o}(1 - f) \tag{2.14}$$

The power required to entrain the excluded sulfur is

$$\Phi_S = w(1 - f)\Delta\rho_c \left[\psi(R_o) - \bar{\psi}\right] \tag{2.15}$$

where $\Delta\rho_c = \gamma\chi_l$ is the density contrast due only to compositional differences between the liquid and solid. γ is an experimentally derived parameter with a low dependence of χ_l over the range of interest. f is the fraction of sulfur that is trapped above the solidification front and thus does not need to be dynamically remixed to allow the front to progress downward.

Combining Eq.s (2.9), (2.10), (2.12), (2.14) and (2.15), we find

$$f_t > 1 - \frac{\alpha T_s' \rho_l}{\gamma} \tag{2.16}$$

That is, in order for fractional crystallization to proceed downward, at least a fraction f_t of the material at a given depth must remain liquid. The right side of this inequality varies as solidification progresses since both T_s' and γ are functions of χ_l. It is positive when $\chi_l > 23$ wt.% S and has a maximum value of ~0.8 (Fig. 2-3). An inwardly solidifying core could thus only expect to see only a fraction of its fractional crystallization spectrum across its depth. Since this result depends on the material properties of the Fe-FeS system, changes in composition could lessen or remove this

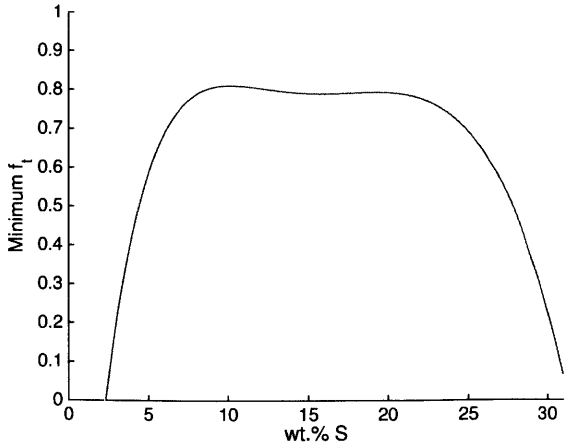

Figure 2-3: The minimum liquid fraction, f_t, as a function of χ_l. This liquid does not necessarily need to be immobile. Rather f_t refers to the fraction of material that must remain liquid at the solidification front to enable downward fractional crystallization.

limitation on dendritic growth.

Perhaps more interesting than which variables appear in (2.16) is which variables do not. Heat flux does not affect this inequality. Nor does core size until pressures are high enough to significantly affect solidus temperature. $(1 - f)$, the fraction of sulfur remixed into the liquid core convecting beneath the solidification front, does not matter. Note that if no sulfur were excluded, the solidus temperature within the inner core would not change. In this case, there would be no driving force for continued convection in the liquid core, and batch solidification would ensue rather than fractional solidification.

Finally, we suggest that inter-dendritic fluid would tend towards a stable stratification rather than large-scale convection. Fluid at the top of the layer would become more enriched in sulfur as the temperature there decreased, leading to local solidification. A conductive profile will be stable if $\alpha(T_s(\chi_l) - T_s(\chi_{eut}))/(\rho_l(\chi_l) - \rho_l(\chi_{eut})) < 1$. For $\chi_l < \chi_{eut}$, the left side of this inequality ranges from 0.25 to 0.63. This conclusion differs from Haack and Scott (1992), who suggest that inter-dendritic liquid would undergo chemical convection.

2.2.4 Stability of dendrites

Solidification from above will be gravitationally unstable and may sink into the planetesimal's interior. We estimate the timescale of this collapse by treating it as an Rayleigh-Taylor instability problem. The timescale of overturn of an unstable layer of thickness d is given by

$$\tau_{RT} = \frac{4\pi\mu_s}{\xi g_0 d^2} \tag{2.17}$$

where μ_s is the layer's viscosity and ξ is its density gradient (Hess and Parmentier, 1995). Viscosity of solid iron near its melting point is perhaps 10^{13} Pa s (Van Orman, 2004), although estimates vary. More accurately, the viscosity of this layer will depend by orders of magnitude on temperature, porosity, and composition. The activation energy for grain diffusion in solid iron has been estimated at 300 kJ mol^{-1} K^{-1} (Yunker and Van Orman, 2007). Assuming Newtonian rheology, this would indicate that viscosity at the Fe-FeS eutectic temperature is $\sim 10^{17}$ Pa s. A simple estimate of the density gradient assumes the density contrast between solid and liquid is spread across the layer and is reduced by the fraction of trapped liquid, so that $\xi = (\rho_{Fe} - \rho_{l0})(1 - f_t)/d$. For the values $g_0 = 0.2$ m s^{-2}, $d = 1$ km, $\xi = 96$ kg m^{-3} km^{-1}, we find $\tau_{RT} = 200$ yr - 2 m.y. It is therefore highly plausible that kilometer-sized dendrites would have become unstable within the $\sim 10^7$ years required for inward solidification.

2.3 Cumulate inner core formation

Rather than producing large-scale dendritic growth, the limit on planar growth may result in unattached crystallization near the top of the liquid. These crystals could accumulate in the body's center as an inner core. Alternatively, collapsed dendrites may similarly accumulate into an inner core. In this section we estimate the settling rate of these entrained crystals and the compaction of a cumulate inner core.

2.3.1 Crystal settling

The terminal settling velocity of a spherical particle is given by Stokes' Law:

$$v_s = \frac{2g\Delta\rho a^2}{9\rho_l \nu} \tag{2.18}$$

where $\Delta\rho$ is the density difference between the liquid and solid, ρ is the liquid density, and a is the crystal radius. This expression is valid for Reynolds number $Re = 2av_s/\nu < 0.1$, which is not necessarily true here. We therefore must use the more general set of equations which is valid while $Re < 3 \cdot 10^5$ (Zhang, 2008),

$$v_s = \sqrt{\frac{8ga\Delta\rho_l}{3\rho C_D}}, \tag{2.19}$$

$$C_D = \frac{24}{Re}(1 + 0.15Re^{0.687}) + \frac{0.42}{1 + 42500Re^{-1.16}}. \tag{2.20}$$

For $a = 1$ mm, $v_s \approx 1$ mm s^{-1}. When a crystal enters the lower boundary of convection, vertical fluid velocity approaches zero so the particle's Stokes velocity becomes dominant. Following Martin and Nokes (1989), we assume that crystal density is homogeneous due to rapid convection and low enough that the crystals are effectively non-interacting flow tracers. If no new solid material is introduced into the liquid, then the number of crystals in the liquid, N, will decrease exponentially due to settling such that its time rate of change is given by:

$$\dot{N} = -\frac{A_i v_s N}{V_l} \tag{2.21}$$

where $V_l = (4\pi/3)(R_o^3 - R_i^3)$ is the liquid volume, and $A_i = 4\pi R_i^2$ is the area of the bottom boundary. Crystal fraction by volume, $f_{cr} = NV_{cr}/V_l$, is a more useful measure of crystal content in the liquid. V_{cr} is the volume of an individual crystal.

V_l is not constant since settling increases inner core radius R_i and thus $\dot{V}_l = V_{cr}\dot{N}$. Making these substitutions in Eq. (2.21), the rate of change of crystal fraction within the liquid can be expressed as:

$$\dot{f}_{cr} = -\frac{A_i v_s f_{cr}(1 - f_{cr})}{V_l} + \frac{w}{V_l}, \tag{2.22}$$

where the second term on the right accounts for newly solidified crystals unattached to the core-mantle boundary. Unlike the case examined by Martin and Nokes (1989), V_l, A_i, and v_s are all dependent on R_i and therefore on time.

We note that the increase in solid inner core volume, V_i, is equal to the rate of crystal settling as described in Eq. (2.21) times the volume of each crystal.

$$\dot{V}_i = A_i v_s f_{cr} \tag{2.23}$$

Since, $\dot{V}_i = \partial V_i / \partial R_i \partial R_i / \partial t = A_i \dot{R}_i$ we find that

$$\dot{R}_i = v_s f_{cr}. \tag{2.24}$$

Note that v_s is proportional to gravity at the bottom boundary and thus to R_i. Eq.s (2.22) and (2.24) do not have an analytical solution, but solutions can be explored numerically. Figure 2-4 shows the numerical solution assuming the maximum solidification rate from Section 2.2.1 of $w = 12$ km^3 yr^{-1}. As expected, settling is negligible when the core is small so the crystal concentration grows linearly (assuming a constant crystal production rate). However, settling becomes dominant very abruptly, after which N plummets. If initial solid inner core radius $i_0 = 1$ mm (that is, we presume a single crystal at the center), then crystallization within the liquid increases only for ~8 kyr and the crystal concentration by volume reaches a maximum of ~2%, which is low enough not to invalidate the assumptions built into Eq. (2.22).

The maximum crystal percentage also depends on crystal size: smaller crystals will remain suspended for longer and thus are able to accumulate without settling (Fig. 2-4b).

If high crystal fraction is reached, it would increase liquid viscosity, thereby reducing or halting convection. In this scenario, the remaining liquid would solidify in bulk. Suckale et al. (2012) determined a critical crystal fraction of 13%, above which settling in a magma ocean would not proceed. However, the strong evidence for frac-

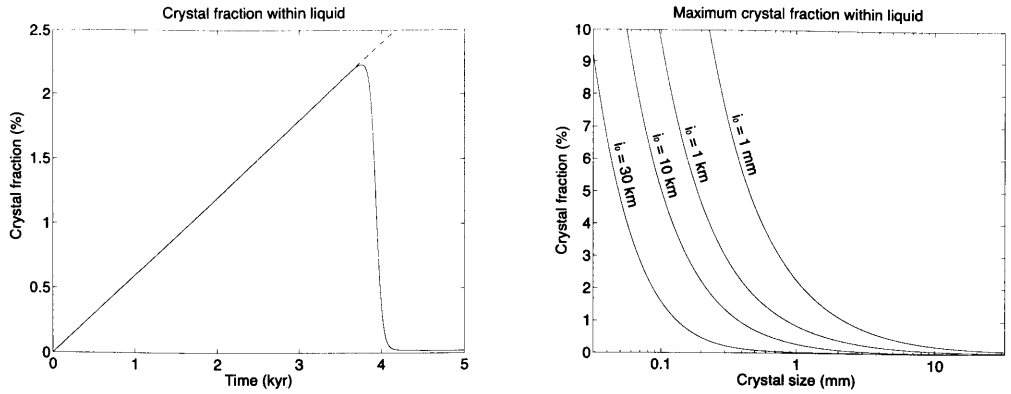

Figure 2-4: Build-up of suspended crystals in liquid. (a) Suspended crystal fraction vs. time. The liquid will become more enriched in crystallized iron with no significant settling until a critical point when settling becomes dominant. The dashed line shows the rate of crystallization if no settling were occurring. (b) Maximum crystal fraction (i.e., the peak of the curve in Figure 4a) as a function of crystal size a and initial solid inner core radius i_0.

tional crystallization in iron meteorites suggests this was not the case in planetesimal cores.

Small crystals may also remelt during convection. Such remelting would resemble the potential iron snow regimes recently discussed for Ganymede (Hauck et al., 2006; Christensen, 2015). In that scenario, free iron crystals are produced in an upper core that is stratified due to varying sulfur content, and melt upon reaching the convecting lower core, enriching the lower core in iron and extending the stratified layer downward. Bulk crystallization would proceed after convection stops, which again is inconsistent with meteoritic data. Therefore, in later sections, we assume that crystals are large enough to settle quickly and not remelt significantly.

In summary, Stokes settling will remove crystallized material from the liquid very efficiently once a substantial inner core is established. Since the solidification rate at the core-mantle boundary is too high to allow excess sulfur to diffuse away, crystals will instead nucleate deeper and contribute to an inner core until the solidification rate decreases due to thickening of the conductive shell and the decrease in the temperature contrast across it.

2.3.2 Compaction

A cumulate solid inner core forming in the microgravity environment of a planetesimal could be highly porous. High porosity could impact other internal processes and the resulting structure. First, it could lead to a secondary convective region beneath the inner-core boundary which could influence dynamo generation. Second, it could make heat transfer out of the solid inner core more efficient. Third, it could result in significant quantities of trapped liquid, which could produce significant contraction as the body cools further and trapped liquid solidifies.

Compaction of a solid matrix has been studied in magma chambers (McKenzie, 2011). Conservation of mass and momentum in such a system can be used to derive the following governing equations (see McKenzie (2011), Appendix A):

$$\frac{\partial \phi}{\partial t} + \frac{\Gamma}{\rho} = \nabla \cdot [(1-\phi)\mathbf{v}] \tag{2.25}$$

$$\nabla(\mu_s \nabla \cdot \mathbf{v}) = \frac{\mu_l}{\mathbf{k}}\mathbf{v} + (\mathbf{1}-\phi)\mathbf{\Delta}\rho\mathbf{g} \tag{2.26}$$

In this section ϕ is used to represent porosity. $\mathbf{v}$ is the velocity of the solid matrix, Γ is the interstitial fluid solidification rate, μ_s is the viscosity of the matrix, μ_l is the liquid viscosity, k_ϕ is permeability, $\Delta\rho$ is the density contrast between solid and liquid, and $\mathbf{g}$ is local gravitational acceleration.

We reduce the problem to a single dimension, letting $\mathbf{v}$=$v\hat{\mathbf{r}}$. Diverging from the magma chamber case, we work in spherical rather than cartesian coordinates. We also set $\Gamma = 0$ and thereby ignore the effect on porosity of possible solidification and melting within the inner core. The resulting equations are:

$$\frac{\partial \phi}{\partial t} = \frac{1}{r^2}\frac{\partial}{\partial r}\left[r^2(1-\phi)v\right] \tag{2.27}$$

$$\frac{\partial}{\partial r}\left[\frac{\mu_s}{r^2}\frac{\partial}{\partial r}(r^2 v)\right] - \frac{\mu_l v}{k} = (1-\phi)\Delta\rho g \tag{2.28}$$

A notable divergence from magma chamber compaction studies results from the

linear dependence of gravitational acceleration g on radius in the core. In a gravity field with negligible radial dependence within the length-scale of the compacting region, porosity will typically decrease at a rate dependent on depth; the liquid is thus pushed out from the bottom up. In a linearly increasing gravity field as found within a uniform sphere, porosity will decrease at the same rate regardless of depth (Sumita et al., 1996). One can verify that a uniform (and exponentially decreasing) ϕ and a v linearly increasing with radius are a stable solution to Eq.s (2.27) and (2.28) in such a gravity field.

The characteristic velocity of the above-described compaction is

$$v_0 = \frac{k_0}{\mu_l \phi_0}(1 - \phi_0)\Delta\rho g_0 \frac{r}{R} \tag{2.29}$$

where ϕ_0 is reference porosity by which k_0 is defined and g_0 is gravity at radius R (McKenzie, 2011). The timescale of compaction is thus dependent on several poorly constrained material parameters. If the timescale of compaction is significantly larger than that of solidification, no compaction will occur and pore space will remain in the inner core. If instead the timescale is significantly smaller, then compaction will be efficient and little fluid will remain trapped.

The characteristic velocity of compaction also depends on gravity and thus on radius. Since compaction is more efficient at larger radius, the outer region of a cumulate inner core would compact more quickly than the interior. The formation of a well-compacted shell could trap fluid in the less compacted interior of the inner core.

2.4 Numerical modelling

The preceding sections have discussed the conditions required for an inward growth front; and alternatively for crystal settling and compaction. We now present a model providing more detailed predictions for one scenario considered reasonable based on these discussions.

We use a radially symmetric finite difference model in spherical coordinates to

simulate the cooling of a planetesimal. The planetesimal is discretized into shells with thickness ~40 m. The surface temperature is set to a constant 250 K. The model begins with a linear temperature profile across the silicate shell and a uniform core temperature of 1820 K, just above the solidus of pure iron.

When a liquid shell cools to its solidus temperature, it remains at constant temperature until the latent thermal energy produced by the shell's solidification is conducted away. Sulfur is then partitioned such that the sulfur fraction of the solid shell is $\chi_s = \chi_l f$ corresponding to trapped melt in the case of inward solidification. The remaining fraction of sulfur is mixed evenly into the liquid inner core, reducing the solidus temperature and requiring additional secular cooling before another shell can solidify. Pressure effects on the solidus temperature are ignored as they are negligible for asteroid-sized bodies, especially compared to the effects of sulfur enrichment. Due to our choice of adiabatic and solidus temperature gradients, solidification will always occur at the outer-core boundary.

After the Fe-FeS eutectic is reached, a eutectic mixture of Fe and FeS begins to crystallize. This mixture, $\chi_{FeS} = 68.5\%$ troilite by weight, is buoyant and, since it does not exclude sulfur, is able to solidify concentrically inward. Its latent heat of fusion is given by:

$$L_{eut} = L_{Fe}(1 - \chi_{FeS}) + L_{FeS}\chi_{FeS} \tag{2.30}$$

where L_{FeS} is the latent heat of fusion of troilite.

Within the silicate shell and the solid portion of the core, temperature T is governed by a diffusion equation,

$$\rho c_P \frac{\partial T}{\partial t} = k\nabla^2 T + H, \tag{2.31}$$

H is a term accounting for the release of latent heat in the trapped melt of a dendritic layer as it cools and solidifies. Before reaching the eutectic, it is given by

$$H = L\rho_{Fe}\frac{1}{V}\frac{\partial V_t}{\partial t} \tag{2.32}$$

where V_t is the volume of a shell (of total volume V) that is still liquid. This term can be related to the change in temperature since $\partial T/\partial t = \partial T/\partial \chi_t \partial \chi_t/\partial V_t \partial V_t/\partial t$. $\partial T/\partial \chi_t = T_s'(\chi_t)$ since the liquid is assumed to be in equilibrium. Through mass conservation (neglecting the change in density), $V_t = V\chi_s/\chi_t$, so that

$$H = \frac{L\rho_{Fe}\chi_s}{\chi_t^2 T_s'(\chi_t)} \frac{\partial T}{\partial t} \tag{2.33}$$

and χ_t is the sulfur fraction such that $T_s(\chi_t) = T$. During final eutectic solidification, temperature is constant and thus H is determined from Eq. (2.31) until the remaining latent heat is removed.

Within the liquid portion of the core, temperature is presumed adiabatic, such that

$$T(r) = T(R_o) exp\left[\frac{R_o^2 - r^2}{D^2}\right], \tag{2.34}$$

where r is radius, R_o is the radius of the upper boundary of the liquid, and D is a length scale defined by $D^2 = 3c_P/2\pi\alpha\rho_l G$. G is the gravitational constant. $D \sim 3000$ km, so the adiabatic gradient across the core is ~ 2 K.

In the cumulate inner core scenario, the newly solidified volume is removed from the core-mantle boundary and immediately added to the inner core. Following Sumita et al. (1996), who found that the surface porosity value was not influential, surface porosity is assumed to be $\phi_i = 0.5$. In comparison, estimated surface porosity values vary from 0.2-0.29 for magmatic systems (Arzi, 1978; Toramaru and Fujii, 1986) to 0.7 for deep-sea sediments (Haq et al., 1990). Eq.s (2.27) and (2.28) are evaluated iteratively in parallel with the thermal model. The dependence of permeability on ϕ is uncertain; we use the relation $k_\phi \propto \phi^3$. Viscosity μ_s is assumed constant. We also ignore solidification within the inner core by setting $H = 0$.

Melting at the surface of the inner core is accounted for in the same way as solidification: if a solid layer is heated to the adjacent liquid's solidus temperature, it remains there until it has absorbed sufficient latent heat to re-melt.

2.4.1 Dynamo and magnetic field estimates

There are several formulations in the literature that provide estimates for the power thermodynamically available to maintain a dynamo (e.g., Lister and Buffett (1995); Nimmo (2007); Christensen (2010)). Several have been shown to be equivalent or approximately equivalent (Lister, 2003). Here we use a buoyancy-flux based formulation (Buffett et al., 1996; Buffett, 2002).

In the case where crystal settling causes a solid inner core to grow concentrically outward, the power thermodynamically available to a dynamo, Φ can be expressed as,

$$\Phi = \Phi_o - \Phi_S + \Phi_i + \Phi_{Fe} \tag{2.35}$$

Here Φ_o and Φ_S are the outer-core boundary heat flow and sulfur remixing terms from Eq.s (2.10) and (2.15), respectively. Φ_i and Φ_{Fe} are the available power due to inner core heat flow and crystal settling, respectively expressed by

$$\Phi_i = \frac{\alpha Q_i}{c_P}\left[\bar{\psi} - \psi(R_i)\right] \tag{2.36}$$

$$\Phi_{Fe} = w\Delta\rho\left[\psi(R_o) - \psi(R_i)\right] \tag{2.37}$$

where Q_i is inner-core boundary heat flow. $\Delta\rho$ is the density difference between liquid and solid, while $\Delta\rho_c$ is only the component of $\Delta\rho$ due to compositional differences between liquid and solid.

In the case of concentric inward solidification above a well-mixed liquid, crystal settling does not occur and there is no inner core, so Φ_{Fe} and Φ_i are both zero. During the eutectic phase of solidification, during which we assume crystallization occurs inward in either general scenario, Φ_{Fe} and Φ_S are both zero.

We can estimate the magnetic field by equating magnetic energy to a fraction of available power with

$$\frac{B^2}{2\mu_0} = cf_{ohm}\frac{L}{U}\phi \tag{2.38}$$

where B is the magnetic field strength within the core, μ_0 is magnetic permeability, c is a constant of proportionality, f_{ohm} is the fraction of dissipated power converted to magnetic energy, $L = R_c - R_i$ is the characteristic length scale, and U is the characteristic flow velocity. ϕ is the volumetric thermodynamically available power, $\phi = \Phi/V_l$, where V_l is the volume of the convecting liquid core. We assume $f_{ohm} \approx 1$, which is the case when viscosity is negligible as is usually assumed in planetary cores (e.g., Christensen and Aubert (2006); Roberts and Aurnou (2012)).

We use the mixing length scaling laws derived in Christensen (2010) to estimate velocity U. Although the scalings are derived for thermal convection, they are applicable to a thermochemical dynamo as well since the difference in buoyancy source only affects the available power for convection, not the form of the force balance equations. Mixing length theory assumes a balance between inertial and buoyancy forces. Following Christensen (2010) but generalizing from thermal convection, we find $U = (\phi L/\rho_l)^{1/3}$ so that

$$B^2 = 2\mu_0 c(\rho_l R_c^2 \phi^2)^{1/3} \tag{2.39}$$

Dynamo action can occur only if the system's magnetic Reynolds number, $Re_m = LU/\lambda$, where λ is magnetic diffusivity, is sufficiently large. This critical value has been various estimated between 10 and 100 (Stevenson, 2003).

Poloidal components of the magnetic field will reach the surface while toroidal components will not. Although the partitioning of energy into these components is not known, we apply a multiplier of one seventh to estimate the dipole component of the magnetic field B at the CMB (Christensen and Aubert, 2006). In typical planetary problems, only the dipole reaches the surface since multipolar components fall away more steeply with radius. In a mantle-less planetesimal, other components would also be present. For simplicity and for consistency with other studies, we report only the dipole component of the predicted surface field, $B_{dip} = (1/7)B(R_c/R)^3$.

2.5 Results and discussion

The direction of solidification was found to have a profound influence on magnetic field generation, solidification timescales, and the final distribution of troilite. We now compare these two scenarios for an initial sulfur concentration of $\chi_{l0} = 6$ wt.%. In the inward case, we assume a trapped liquid fraction of $f_t = 0.8$ at the solidification interface. This value was chosen since it is approximately the lowest value that permits a well-mixed liquid inner core throughout solidification, as discussed in Section 2.2.3. Figure 2-5 shows the inward solidification scenario, where an increasingly thick solid outer core slows heat flow out of the underlying liquid and consequently reduces the solidification rate as time progresses. The core takes about 10.5 m.y. to completely solidify.

The thickness of the dendritic region, defined as the region where dendrites have extended but inter-dendritic material has not yet solidified, depends on the thermal gradient and heat flow across it. The thickness grows initially as heat flow reduces due to the insulating outer core, but reduces as inner core cooling reduces the thermal gradient. When the remaining liquid inner core reaches the Fe-FeS eutectic, all overlying material is solid. Since almost all of the sulfur has been trapped between dendrites in the outer core, the remaining eutectic melt is a small fraction of the core's total volume. The final eutectic melt region is only 6.5 km in radius, about .028% of total core volume. Lowering f_t or increasing χ_{l0} increases this fraction but does not substantially affect the solidification timescale.

Figure 2-5b shows that much of the outer core of a planetesimal would have cooled below its Curie temperature while the inner core was still liquid and thus be potentially capable of recording a dynamo field. Prior to solidification, our scaling estimate suggests a dynamo field of 160 μT. However, due to the reduction in inner core heat flow after solidification begins, dynamo strength quickly reduces to ~10 μT. As the length-scale of convection decreases due to ongoing solidification, The magnetic Reynolds number falls below its critical value and the dynamo shuts off (Fig. 2-5d).

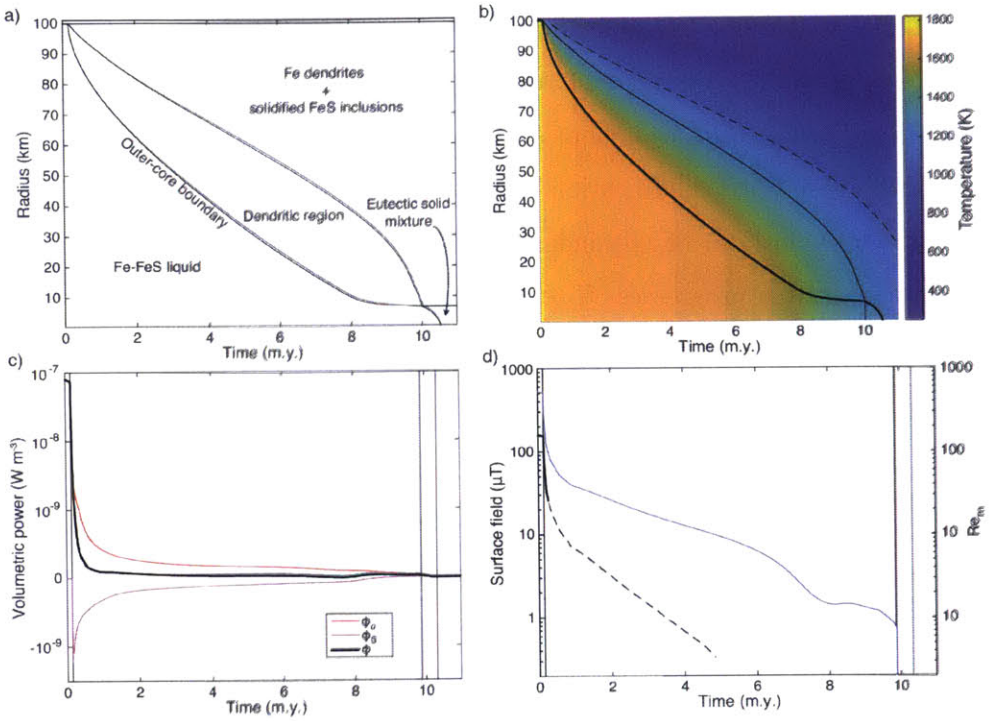

Figure 2-5: Inward solidification. a) Schematic of solidification over time. b) Temperature as a function of time. The thick solid line shows the inner-core boundary, while the thin solid and dashed lines follow the eutectic and Curie isotherms, respectively. c) Volumetric power available for a dynamo. The plot is linear between -10^{-9} and 10^{-9}, and logarithmic beyond this region. The three horizontal dashed lines mark the initiation of solidification, the onset of eutectic solidification, and the completion of solidification. d) The surface magnetic dipole field (thick black line) and the magnetic Reynolds number (blue line). The horizontal dashed line shows the critical magnetic Reynolds number of 50 and the vertical lines are the same is in part c).

In comparison, Figure 2-6 shows a cumulate inner core solidification scenario. Solidification is complete in the scenario of a cumulate inner core in about 0.6 m.y., about 18 times faster than an inwardly solidifying core. This accelerated timescale occurs for two reasons. First, the overlying conductive layer never thickens (until the eutectic is reached) and instead allows for a consistently high heat flow from the core through the course of solidification. Second, rather than requiring that the planetesimal's center be cooled to the eutectic in order to complete solidification, the solid inner core can remain at temperatures above the eutectic while the residual liquid at the top of the core continues to cool. The result is a predominantly metallic inner core with a eutectic mixture located just beneath the surface rather than at the center. This eutectic mixture composes $\sim$19% of the total core volume.

Of the power sources available to power a dynamo in the cumulate core scenario, iron crystal settling is by far the most dominant term; however, inner core cooling becomes significant as the rapid liquid cooling creates a large temperature contrast across the solid inner core. Rather than the reduction in magnetic field strength at the onset of solidification seen in the inward solidification case, the field increases to a peak of 270 μT. However, the reduction in convective length-scale again reduces the magnetic Reynolds number below its critical value as solidification progresses.

The timing of a shutoff due to insufficient magnetic Reynolds number is poorly constrained for two reasons. First, its calculated value falls between the lowest and highest estimates of critical Re_m for nearly the entire solidification process. Second, the characteristic velocity used to estimate Re_m is derived from a scaling law and thus only an order-of-magnitude estimate of velocity.

It is thus difficult to conclude whether a dynamo field could be sustained during this period and be recorded in a solid outer core. However, this analysis only includes power available due to thermochemical convection. A dynamo driven by precession, for example, could also have its field recorded by a solid outer core.

A dynamo surrounded by a solid outer core may also differ from a typical Earth-like dynamo in more subtle ways. Vilim et al. (2013) found that when the inner core is small, magnetic field strength is raised by as much as 20% in the presence of an

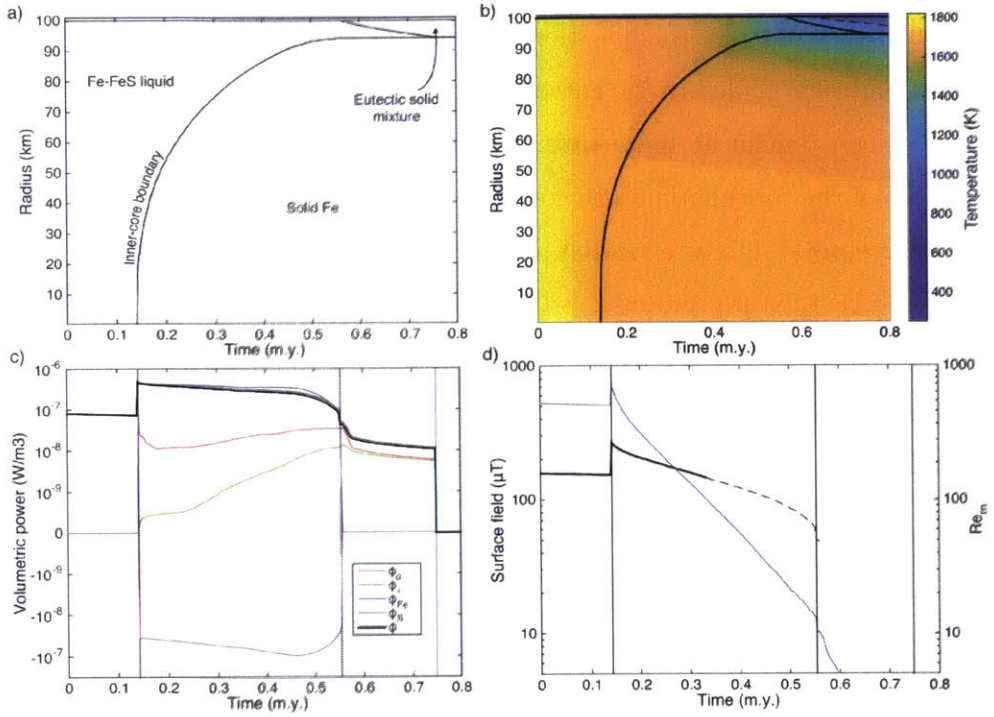

Figure 2-6: Cumulate inner core solidification. a) Schematic of solidification over time. b) Temperature as a function of time. The thick solid line shows the inner-core boundary, while the dashed line follows the Curie isotherm. c) Volumetric power available for a dynamo. The plot is linear between -10^{-9} and 10^{-9}, and logarithmic beyond this region. The three horizontal dashed lines mark the initiation of solidification, the onset of eutectic solidification, and the completion of solidification. d) The surface magnetic dipole field (thick black line) and the magnetic Reynolds number (blue line). The horizontal dashed line shows the critical magnetic Reynolds number of 50 and the vertical lines are the same is in part c).

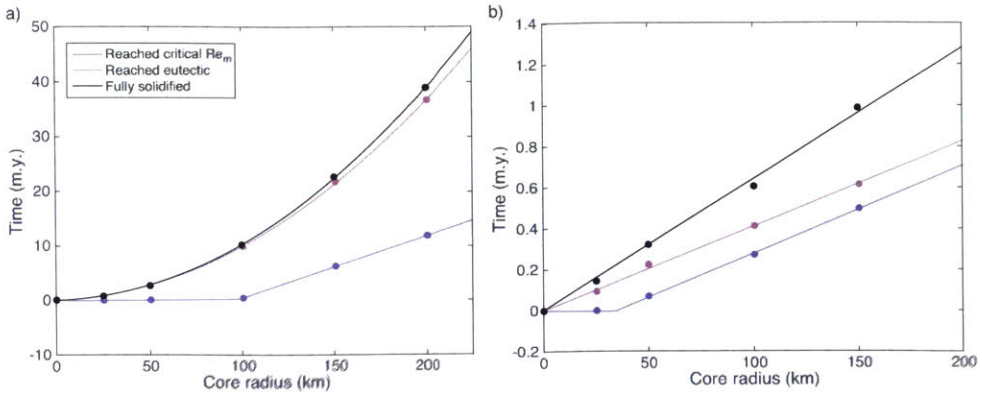

Figure 2-7: Dependence of timescales on core radius. The magnetic field shut-off times are plotted for a critical Re_m of 50 (e.g., Christensen et al., 1999). a) Inward solidification. The time required from the onset of solidification to reach the eutectic liquid composition and fully solidify is proportional to radius squared. A dynamo is able to continue operating during inward solidification in bodies larger than ~100 km. Its duration is directly proportional to radius. b) Cumulate inner core solidification. All timescales scale directly with radius.

electrically conducting lower mantle overlying a convecting core. A solid outer core may have a similar impact.

Dependence of the timescales of solidification on core radius are shown in Figure 2-7. In the inward solidification scenario, the time necessary for solidification to and beyond eutectic composition scaled with the radius squared. In the outward scenario, these timescales depended directly on radius. This difference is expected since in the former case conduction is the primary mode of heat transfer, while in the latter case convection is. The time at which the critical Re_m is reached, on the other hand, scales linearly with radius in both scenarios. A larger core could thus record a magnetic field in a larger proportion of its volume in an inward solidification scenario. However, dendrites would be less stable in a larger core due to higher gravity.

2.5.1 Inner core porosity structure

Figure 2-8 shows the porosity of a cumulate inner core using a reference permeability of $k_0 = 10^{-10}$ m^2 when $\phi = 0.5$. This permeability was sufficiently high that almost all trapped liquid was ejected from the inner core. However, a small amount of liquid

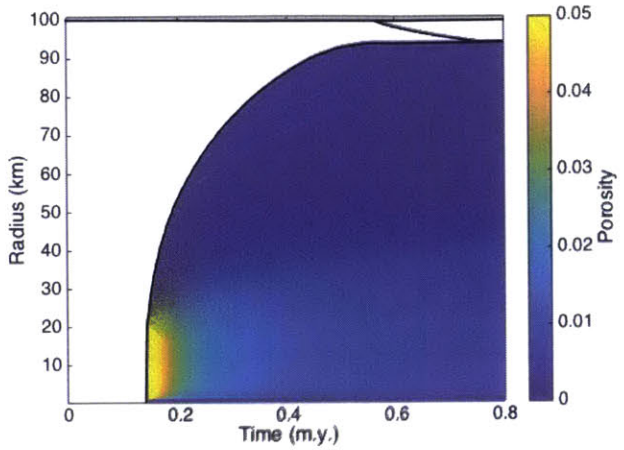

Figure 2-8: Porosity of the growing inner core for permeability $k_0 = 10^{-10}$ m^2. The structures in the more compact upper section are solitary waves of liquid migrating toward the surface. Apparent downward migration is an image artifact that occurs when the sills become very closely packed.

remained in the central ~10 km, where gravity was too weak to compress the solid matrix and expel the liquid. Porosity is independent of depth near the center of the planetesimal, but subsequent crystal settling produces a highly compacted layer above it. Liquid migrates upward towards the surface in solitary waves, depleting the lower layer, but at a very low rate.

When permeability is smaller, compaction proceeds less efficiently. Figure 2-9 shows the average liquid fraction (porosity) of the cumulate inner core as a function of time for various values of permeability. For $k_0 < 10^{-14}$ m^2, significant compaction of the inner core does not occur during the period needed for solidification of the purely liquid core above. For such high porosity, the assumption of perfect compaction in the thermal model and of no solidification or melting in the compaction model become invalid.

It appears the transition from a well-compacted inner core to an uncompacted inner core is between $k_0 \sim 10^{-11} - 10^{-14}$ m^2 for the parameters assumed in Table 1. Permeability estimates in other materials range from 10^{-10} m^2 for magma chambers to 10^{-20} m^2 for some sediments (Sumita et al., 1996). Although better constrained, liquid viscosity could also vary by several orders of magnitude. Since in the equations

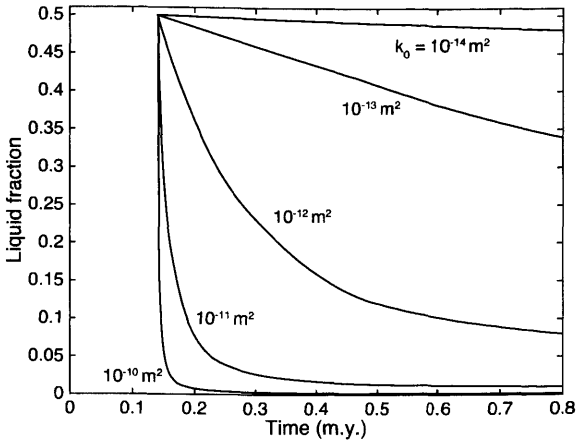

Figure 2-9: Average liquid fraction (porosity) in the cumulate inner core as a function of time for various values of reference permeability k_0, defined as the permeability when $\phi = 0.5$. For permeability below 10^{-14} m^2, practically no compaction occurs. Compaction is almost complete efficient for permeabilities above 10^{-11} m^2.

governing compaction k_0 and μ_l only appear together, a higher liquid viscosity would be equivalent to a lower permeability. If significant liquid remained in the core, then additional processes not accounted for here could influence core evolution - for example, liquid convection, melting, and chemical exchange within the inner core.

On the other hand, a one-dimensional approach to the compaction problem does not allow for potential "chimneys" or other laterally heterogenous structures. Such chimneys would significantly enhance fluid flow, resulting in a higher effective porosity and more efficient compaction.

2.5.2 Gravitational instability in an inner core

The inverse correlation of Ni fraction to cooling rate in some meteorite families implies that nickel fraction increased with depth in some parent bodies. However, this is only necessarily true at the time the cooling rate was recorded, well below the solidus. Such an inverse correlation, which is typically explained by inward solidification, could potentially also be explained by an overturn event within a cumulate inner core due to thermal or compositional gradients.

Assuming a linear change in density between taenite end-members of pure Fe

and pure Ni yields a density contrast of $\Delta\rho = (\rho_{Fe} - \rho_{Ni})\Delta f_{Ni}$, where Δf_{Ni} is the difference in Nickel fraction. Within the IVA meteorites, a difference of $\Delta f_{Ni} \sim 3\%$ has been observed, yielding a density contrast of ~ 30 kg m^{-3}. Assuming an overturn timescale of $\tau_{RT} = 4\pi\mu_s/\Delta\rho g_0 R_c$ yields ~10 yr if viscosity μ_s is taken to be its near-solidus value of 10^{13} Pa s, and ~0.1 m.y. if the viscosity has increased to 10^{17} Pa s.

This mechanism could render outward core growth compatible with the observed inverse correlation of some parent bodies. However, considerable scatter in the cooling rate vs. Ni wt.% correlation would be expected in the event of an overturn event, which is not evident in observation.

2.6 Conclusions

We have discussed and modeled aspects of several processes that would have occurred in a solidifying core. For the most part, these discussions are applicable to small cores within a mantle, although in that case additional time-dependent processes control heat flow from the core.

A fractional solidification growth front proceeding concentrically inward from the core-mantle boundary is difficult to explain from both energy and chemical diffusion perspectives. If the thermal gradient is the only driver for convection in a liquid inner core, then a theoretical minimum on the amount of inter-dendritic liquid can be derived based solely on the liquid's composition and its influence on the liquid's solidus and density. If dendrites did form, then their size would likely have been limited by their gravitational instability.

With these considerations, it is difficult to explain how a 100-km core could have solidified fractionally inward as suggested by the negative correlation of cooling rate to nickel fraction in the IVA meteorites. Overturn of a core that solidified outward could potentially explain such a negative correlation without inward solidification. Alternatively, buoyant, sulfur-rich fluid could potentially be expelled through fractures formed in the solid outer shell, easing the limitations on inward solidification. Fur-

ther modeling could examine the consistency of such scenarios with the fractionation trends observed in meteorites.

A cumulate inner core could potentially develop if crystals form freely in the liquid unattached to the core-mantle boundary. The fate of these crystals depends on a number of unknown variables: their size distribution, liquid viscosity, and the presence of any larger solid iron crystal (perhaps a collapsed dendrite) to function as a seed for an inner core. If crystal settling was not efficient, high crystal fraction would have increased liquid viscosity, reducing convection and potentially causing solidification of the remaining liquid to proceed in bulk. If a cumulate inner core did form, then poorly constrained parameters such as liquid viscosity and matrix permeability would determine the degree to which compaction occurred, with implications for the trapped liquid content and later contraction.

Inward solidification and outward growth of a cumulate inner core are two end-member possibilities of planetesimal core solidification. However, these processes could have been operating in tandem, with nonlinear results. For example, if we allow that crystal settling may help drive convection, then the limit on dendritic solidification would be relaxed.

In both scenarios examined here, dynamo action during solidification is possible if the body is sufficiently large and the assumed critical magnetic Reynolds number is sufficiently small. In an inwardly solidifying body, such a field could have been captured by the overlying solid iron shell.

Acknowledgements

Thanks to coauthors L.T. Elkins-Tanton, G. Schubert, and D. Bercovici. We also thank S. Brown, R. Fu, and K. Soderlund for thoughtful discussions and comments.

Chapter 3

Magnetic field generation in the lunar core: The role of inner core growth

Abstract

The source of the magnetic field recorded in the lunar crust remains an unresolved problem. The field was most likely produced by a self-sustaining dynamo in the Moon's electrically conducting metal core, but heat flux across the core-mantle boundary was probably insufficient to power a dynamo for the field's currently known duration from 4.2 to 3.56 Ga. Since seismic measurements indicate the existence of a solid iron inner core in addition to a still-liquid iron alloy outer core, inner core solidification and its associated thermochemically driven convection in the outer core could have been responsible for extending the dynamo's lifetime even in the absence of superadiabatic heat flux. Here we present a coupled mantle-core thermal evolution model of the Moon and show that core solidification could explain the onset and shutoff of the lunar dynamo consistent with the global magnetic field inferred from the paleomagnetic record.

3.1 Introduction

Snapshots of planetary magnetic history are recorded into crust when ferromagnetic minerals cross a critical (Curie) temperature in the presence of a magnetic field. Paleomagnetic observations of the lunar crust from the Lunar Prospector and Kaguya

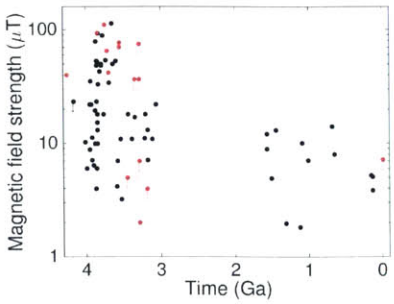

Figure 3-1: Summary of lunar paleomagnetic evidence. Black points represent Apollo-era measurements (Fuller and Cisowski, 1987; Wieczorek et al., 2006). Red points indicate modern more reliable data produced using the IRM and Thellier-Thellier methods (Weiss and Tikoo, 2014); these measurements have a two-sigma uncertainty factor of approximately five. Arrows indicate that a data point only provides an upper limit in field strength and/or age.

(SELENE) missions as well as laboratory analyses of returned Apollo samples indicate the likely presence of a core dynamo producing surface fields of approximately 70 μT at least between 4.2 and 3.56 Ga (Suavet et al., 2013; Shea et al., 2012). Tikoo et al. (2014) present paleomagnetic data suggesting that the surface field declined to less than 4 μT by 3.19 Ga. This relatively weak field appears to have persisted until <200 Ma (Wieczorek et al., 2006); however, paleomagnetic evidence beyond 3.19 Ga is also consistent with a null field (Weiss and Tikoo, 2014). The low fields (<0.2 nT) observed in some locations on the lunar surface indicate the dynamo is not active in the present day (Mitchell et al., 2008; Weiss and Tikoo, 2014). Figure 3-1 shows a summary of current paleomagnetic evidence.

Models of thermal convection-driven dynamos typically demonstrate sufficient heat flow to produce a dynamo for perhaps 100 million years (Stegman et al., 2003; Laneuville et al., 2013), although a low adiabatic heat flow value can result in heat flow being sufficient to sustain a dynamo for nearly two billion years in some cases (Evans et al., 2014). However, these models can account for neither the late-stage dynamo nor the high magnitudes of the early field.

Several alternative mechanisms have been recently proposed to provide kinetic energy to power fluid motion necessary for dynamo action. The Moon is believed to

have originated in a giant impact and gradually migrated away from Earth (Canup and Asphaug, 2001); a smaller orbital distance would correspond to a larger tidal forcing in the liquid core, which could have deposited enough precessional energy in the core to produce a dynamo until the Earth-Moon distance became too great (Dwyer et al., 2011; Tian et al., 2014). Impacts large enough to alter the Moon's rotation rate could also have been responsible for short bursts of dynamo action by causing a differential rotation between the mantle and the poorly coupled liquid core, which would gradually adjust to the new rotation rate (Le Bars et al., 2011). Similarly, Cebron and Hollerbach (2014) and Cebron et al. (2014) show that latitudinal libration can drive a dynamo through the excitation of inertial instabilities in the lunar core. Large impacts may also produce locally strong magnetic anomalies due to the magnetization of highly conducting projectile materials (Wieczorek et al., 2012). These different mechanisms may all have been working at the same time in the Moon and other small bodies, suggesting an early solar system history replete with active dynamos.

A dynamo powered by solidification of the inner core is beginning to receive consideration. In this scenario, solidification of iron at the center of the core would enrich the local liquid in light elements, which would then rise to the core mantle boundary, driving convection. Konrad and Spohn (1997) discussed, but ultimately rejected, the possibility. They cited Conzelmann (1994) who used a thermal model of the Moon and found that, unlike a purely thermally driven dynamo, a dynamo partly driven by chemical convection in fact provided sufficient energy to power the dynamo to the present day. Since no lunar dynamo has been detected at present, they concluded that the core must be entirely liquid or entirely solid, and that a chemical dynamo therefore could not have played a significant role.

Stegman et al. (2003) discussed a thermochemical dynamo but concluded that there were not sufficient constraints on key core parameters to consider such a dynamo explicitly. With more recent constraints on core size, Zhang et al. (2013) used numerical mantle convection models coupled with inner core growth models. While noting the potential for a thermochemical dynamo, their work focused on explaining

the asymmetric distribution of radioactive heat sources and mare basalts.

Most recently, Laneuville et al. (2013, 2014) used a similarly coupled mantle and core convection model, and the latter explored the possibility of a chemically driven dynamo. They found that sufficient energy would have been supplied by inner core solidification to produce a maximum magnetic field of 0.36μT and suggested that the dynamo shut down as a result of a change in the solidification process: late-stage solidification would have occurred at the core-mantle boundary rather than at the inner-outer-core interface, resulting in an iron snow regime with limited ability to power the dynamo.

Reanalysis of Apollo seismological data together with moment of inertia measurements suggest that at present the Moon, like Earth, has both a solid inner core and a liquid outer core (Weber et al., 2011; Khan et al., 2013; Garcia et al., 2011). Thus, even at present, solidification of the inner core is presumably continuing and thus producing some convective instability, albeit at too low a rate to produce a dynamo. Much uncertainty remains in core size estimates. Weber et al. (2011) suggest an inner core radius of 240 ± 10 km and an outer core radius of 330 ± 20 km with $\lesssim$6 wt.% sulfur. Recent work incorporating GRAIL measurements finds that the ranges of 0-280 km and 200-380 km for the inner and outer core, respectively, are compatible with current knowledge, although these variables are not independent; a smaller inner core would require a larger outer core to explain the same observations (Williams et al., 2014). These ranges are also consistent with the Fe-S equation of state measurements of Jing et al. (2014); their preferred core model has a radius of 290 km with 4 ± 3 wt.% sulfur and a 200 km solid inner core.

In this study, we estimate the magnitude of compositionally driven convection over the course of lunar evolution and its contribution to magnetic field production. We further investigate the implications that core sulfur content, mantle rheology, and a heterogenous mantle chemical profile would have on the dynamo's strength and longevity.

3.2 Methods

3.2.1 Mantle model

We use the spherical finite-element model CitcomS to simulate mantle convection coupled to a core model which is assumed to consist of a well-mixed fluid and, after the temperature profile cools to the solidus at the body's center, a solid inner sphere. Since the fluid is well-mixed, the mantle model views the core-mantle boundary as a uniform-temperature thermal reservoir. At each model timestep, we determine the inner core growth and temperature as heat is drawn into the mantle, and update the thermal boundary condition to the new core-mantle boundary temperature for the next timestep.

The model assumes that the mantle is an incompressible anelastic shell and that variations in density affect the equations of motion only through changes in buoyancy (the Boussinesq approximation). Mantle evolution is computed by iteratively solving the conservation equations for mass, momentum, and energy. (See Zhong et al. (2008) for details.) The code divides the mantle into 12 caps, each of which we resolve into $36 \times 36 \times 48$ elements, providing a vertical and average horizontal resolution of 30 km. Chemical density information is contained in entrained tracer particles distributed throughout the model that track fluid flow.

We assume a Newtonian Arrhenius rheology in the mantle such that viscosity is given by

$$\mu = \mu_0 \exp\left[\frac{E}{R_g T} - \frac{E}{R_g T_{ref}}\right], \tag{3.1}$$

where E is the activation energy, R_g is the ideal gas constant, and reference temperature T_{ref} is 1300° C. To avoid numerical problems, viscosity is not permitted to exceed $\mu_{max} = \mu_0 \cdot 10^5$. While experimentally determined mineral activation energies are around 300 kJ/mol (Karato and Wu, 1993), Christensen (1984) demonstrated that a prefactor of 0.3-0.6 is realistic when ignoring non-Newtonian effects. In this study we adopt an effective activation energy of 150 kJ/mol. We choose a reference

Symbol	Description	Value
R	Lunar radius	1737 km
R_c	Core radius[1]	330 km
L_B	Blanket thickness	300 km
G	Gravitational constant	$6.67{\cdot}10^{-11}$ m^3 kg^{-1} s^{-2}
ρ_m	Bulk mantle density[2]	3400 kg m^{-3}
ρ_{ic}	Inner core density[3]	7800 kg m^{-3}
g_o	Surface gravity[2]	1.6 m s^{-2}
Ω	Rotational velocity	$2\pi/27.3$ rad d^{-1}
$c_{P,m}$	Specific heat, mantle[3]	1250 J kg^{-1} K^{-1}
$c_{P,c}$	Specific heat, core[4]	850 J kg^{-1} K^{-1}
L	Core latent heat of fusion[5]	300 kJ kg^{-1}
κ_m	Thermal diffusivity, mantle[3]	$1{\cdot}10^{-6}$ m^2 s^{-1}
k_c	Thermal conductivity, core[3]	50 W m^{-1} K^{-1}
α_m	Thermal expansivity, mantle[3]	$3{\cdot}10^{-5}$ K^{-1}
α_c	Thermal expansivity, core[3]	$9{\cdot}10^{-5}$ K^{-1}
T_{m0}	FeS solidus parameter[6]	1809 K
T_{m1}	FeS solidus parameter[6]	$1.99{\cdot}10^{-11}$ Pa^{-1}
T_{m2}	FeS solidus parameter[6]	$1.84{\cdot}10^{-22}$ Pa^{-2}
α_χ	FeS solidus parameter[6]	1.6
T_{surf}	Surface temperature	273 K
E	Activation energy	150 kJ mol^{-1}
U	Uranium concentration[2]	25.7 ppb
Th/U	Thorium/uranium ratio[2]	4
c	Proportionality constant[7]	0.63

Table 3.1: Fixed model parameters. [1]Weber et al. (2011); [2]Stegman et al. (2003); [3]Zhang et al. (2013); [4]Braginsky and Roberts (1995); [5]Stevenson et al. (1983); [6]Hauck et al. (2006); [7]Christensen (2010)

viscosity of $\mu_0 = 10^{20}$ Pa s consistent with a wet mantle (Hirth and Kohlstedt, 2003) in light of recent conclusions that the Moon may not be as dry as previously thought (Karato, 2013). We also examine the effect of assuming $\mu_0 = 10^{19}$ Pa s and $\mu_0 = 10^{21}$ Pa s.

The Rayleigh number, which describes the ratio of buoyancy to diffusion, is defined here for mantle convection as $Ra = \rho_m g_0 \alpha_m \Delta T R^3 / \kappa_m \mu_o$, where ρ_m is a reference density, g_0 is surface gravity, α_m is the thermal expansivity, ΔT is the initial temperature difference across the mantle, R is the radius, κ_m is the thermal diffusivity, and μ_o is the reference viscosity (see Table 3.1). In our reference case, the Rayleigh number is $1.45{\cdot}10^7$.

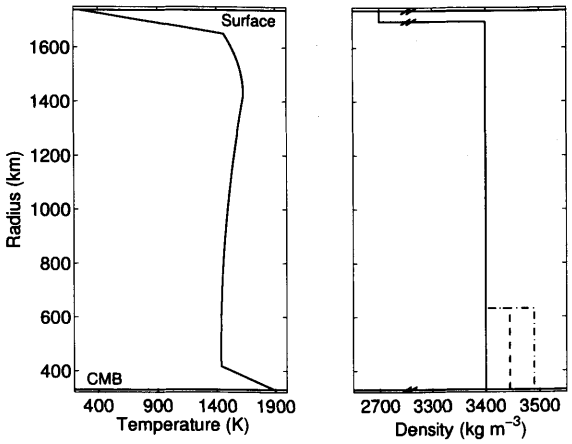

Figure 3-2: Initial lunar mantle conditions. a) Initial thermal profile, defined by an inverted solidus resulting from mantle overturn. b) Initial chemical density profile. Three initial mantle composition profiles are considered underneath a buoyant crust: 1) a homogenous profile (solid line), 2) one with a thermal blanket resulting from mantle overturn with a density contrast of 90 kg m^{-3} (dash-dot line), used by Zhang et al. (2013), and 3) one with a thermal blanket 45 kg m^{-3} more dense than the surrounding mantle (dashed line).

3.2.2 Initial conditions

The initial conditions of our model, illustrated in Figure 3-2, are based on considerations of an early magma ocean. The primordial Moon likely had a global magma ocean as deep as 1000 km which would have undergone fractional crystallization, as evidenced by isotopic comparisons between its anorthite plagioclase lid and the mare basalts (Ryder, 1982), and experimental evidence indicates that plagioclase is not present on the liquidus of mare basalts (Green et al., 1971). While plagioclase precipitates would have been buoyant and risen to form the lid, the remaining magma ocean material would have solidified from the bottom up, producing a solid mantle at its solidus temperature, which increases with depth.

During this process, elements in the magma ocean that were incompatible with the solidifying minerals would have been continually concentrated in the residual melt, resulting in a dense layer just under the buoyant lid (Elkins-Tanton et al., 2011b). At least part of this layer, kept warm by its high concentration of radiogenic elements,

would sink to the core-mantle boundary and remain there until hot enough that its thermal buoyancy would overcome its excess chemical density. This phenomenon, called a thermal blanket effect, would keep the core warm until the layer is removed as a plume. After that, the core would begin to lose heat rapidly, resulting in a short-lived thermally driven dynamo (Stegman et al., 2003; Takahashi and Tsunakawa, 2009), and potentially a long-lived chemical dynamo.

Our reference model assumes no thermal blanket to more readily understand the influence of other parameter choices. In this case, half of the radiogenic heating budget is trapped in the stagnant lithosphere between 60 and 90 km depth, while the other half is distributed evenly in the mantle below. In models which include a thermal blanket, we partition half of radiogenic heating into the dense thermal blanket, while the other half remains in the lithosphere as before (Stegman et al., 2003; Zhang et al., 2013).

We begin our convection model immediately after overturn has taken place. There is large uncertainty in the timing of both magma ocean solidification and its subsequent overturn, but this only enters our model slightly through radiogenic heating estimates. We assume overturn finished at 4.3 Ga (Meyer et al., 2010), but examine the implications of earlier overturn. Any hot material that crossed its solidus during the overturn process by rising to a shallower depth would quickly have melted and resolidified; thus the initial temperature for our model is an inverted solidus in the lower mantle and the solidus in the upper mantle.

3.2.3 Core model

As in other planets, the core is expected to be an alloy of iron, nickel, and siderophile light elements. As the core solidifies from the inside out, the remaining liquid is continually enriched in light elements. We assume a simple core composition of iron and sulfur (Murthy and Hall, 1970; Hauck et al., 2006). The solidus temperature of the Fe-S system decreases with increasing sulfur content and therefore decreases with time as the core crystallizes, extending the lifetime of the liquid outer core up to the present day. For simplicity we assume a linear relationship between temperature and

sulfur content from 0-24 wt. % sulfur (Hauck et al., 2006).

Energy balance in the core can be expressed as

$$Q_{CMB} = Q_c + Q_l + Q_g, \tag{3.2}$$

where Q_{CMB} is the heat flow into the mantle, Q_c is the energy lost due to secular cooling, Q_l is the rate of latent heat production as the core solidifies, and Q_g is the rate of release of gravitational energy due to solidification.

To solve for the core-mantle boundary temperature as heat is removed from the core into the mantle, we follow the approach in Labrosse et al. (2001) and Labrosse (2003) by noting that each term on the right side of Eq. (3.2) can be expressed as a function of the product of known variables and the radial growth rate of the inner core. We can thus use the equation to solve for this growth rate and the core-mantle boundary temperature, and iteratively increase inner core size as the model cools.

Secular cooling Q_c can be expressed as

$$Q_c = \int_V \rho_{avg} c_{P,c} \frac{\partial T(r)}{\partial t} dV = \int_V \rho_{avg} c_{P,c} \frac{\partial T(r)}{\partial R_i} dV \frac{\partial R_i}{\partial t} \tag{3.3}$$

where R_i is the radius of the inner core. The core model assumes that temperature variation in the entire core is adiabatic and radially symmetric, and that the inner-outer core boundary will be at the liquid's solidus, $T_s(R_i)$:

$$T(r) = T_s(R_i) exp\left[\frac{R_i^2 - r^2}{D^2}\right] \tag{3.4}$$

where D is a length scale defined by $D^2 = 3c_{P,c}/2\pi\alpha_c\rho_{oc}G$ and is approximately 3100 km. $c_{P,c}$, α_c, ρ_{oc}, and G are core heat capacity, thermal expansivity, outer core density, and the gravitational constant, respectively. Integrating Eq. (3.3) and substituting Eq. (3.4), we find that

$$Q_c = \rho_{avg} c_{P,c} \left[\frac{\partial T_s}{\partial R_i} + \frac{2R_i T_s}{D^2}\right] \frac{T(R_i)}{T(R_c)} V_{eff} \frac{\partial R_i}{\partial t}, \tag{3.5}$$

where V_{eff} is a constant resulting from the integral of Eq. (3.3). It is within 0.1% of

core volume V for lunar characteristics; the difference accounts for the slight change in adiabatic slope as the core cools.

Assuming the inner core contains no sulfur, the concentration of light elements by mass in the liquid outer core χ depends on the size of the inner core according to:

$$\chi(R_i) = \chi_0 \left(1 - \frac{\rho_{ic} R_i^3}{\rho_{avg} R_c^3}\right)^{-1}, \tag{3.6}$$

where χ_0 is the initial concentration of light elements, and ρ_{avg} is the average density of the core.

The solidus temperature depends on both pressure and sulfur concentration, although the latter effect increasingly dominates as inner core growth proceeds. We use a solidus temperature consistent with Hauck et al. (2006),

$$T_s(r) = T_{m0}(1 + T_{m1}P + T_{m2}P^2)(1 - \alpha_\chi \chi) \tag{3.7}$$

where T_{m0}, T_{m1}, and T_{m2} are experimentally derived constants. α_χ relates solidus temperature to sulfur concentration assuming a linear fit between the pure iron melting temperature and the eutectic point in an Fe-FeS system. We assume a constant α_χ, though more accurately it varies by about 5% over the $\lesssim$1 GPa pressure range found in the lunar core. Pressure is described by $P(r) = P_0 - 2\pi r^2 \rho_{ic}^2$ G/3, where the pressure at the core's center, P_0, is assumed to be 4.8 GPa in line with literature estimates (e.g., Garcia et al., 2012; de Pater and Lissauer, 2015).

The rate of latent heat release can be written

$$Q_l = 4\pi R_i^2 \rho_c L \frac{\partial R_i}{\partial t} \tag{3.8}$$

where L is the latent heat of fusion of iron. Gravitational potential energy of the core can be written

$$E_g = 4\pi \int_0^{R_c} g(r)\rho(r) r^3 dr. \tag{3.9}$$

Integrating a two-layer core where density ρ is modeled as ρ_{ic} in the inner core,

and a depth-independent but time-dependent value ρ_{oc} in the outer core, we obtain

$$E_g = \frac{16\pi^2}{3} G \left[\rho_{ic}^2 \frac{R_i^5}{5} + (\rho_{ic} - \Delta\rho)^2 \frac{R_c^5 - R_i^5}{5} + (\rho_{ic} - \Delta\rho)\Delta\rho \frac{R_i^3 R_c^2 - R_i^5}{2} \right], \quad (3.10)$$

where $\Delta\rho = \Delta\rho_o/(1-\xi^3)$, where $\Delta\rho_o$ is the initial density difference between the inner and outer cores and $\xi = c/R_c$. The gravitational energy release rate is thus described by

$$Q_g = \frac{8\pi^2}{15} G R_c^2 R_i^2 \Delta\rho_o \frac{\rho_{ic} F_1 - \Delta\rho_o F_2}{(\xi^2 + \xi + 1)^3} \frac{\partial R_i}{\partial t}. \quad (3.11)$$

where the form factors $F_1 = 3 + 9\xi + 13\xi^2 + 12\xi^3 + 6\xi^4 + 2\xi^5$ and $F_2 = 3 + 9\xi + 3\xi^2$ are introduced for legibility. Combining Eq.s (3.2), (3.5), and (3.8) and (3.11) with the core-mantle boundary heat flux output from the mantle model, we can solve for the growth rate of the inner core $\partial R_i/\partial t$. We can then solve for the core's temperature and feed it back into the mantle model as its lower thermal boundary condition.

3.2.4 Magnetic field estimates

Several requirements must be satisfied to sustain a dynamo. First, convection must be occurring with sufficient excess energy to power magnetic field generation. Second, the magnetic Reynolds number, $Re_m = U\mathcal{L}/\lambda$, must remain above a critical value of around 50 (Christensen and Aubert, 2006). (Here U is the fluid's characteristic velocity, $\mathcal{L}$ is its length-scale, and λ is the magnetic diffusivity.)

There are several formulations in the literature that provide estimates for the power thermodynamically available to maintain a dynamo (e.g., Lister and Buffett, 1995; Nimmo, 2007; Christensen, 2010). Several have been shown to be equivalent or approximately equivalent (Lister, 2003). Here we use a buoyancy-flux based formulation (Buffett et al., 1996; Buffett, 2002) for its clarity:

$$\Phi = \frac{\alpha_c Q_{CMB}^*}{c_P} \left[\psi(R_c) - \bar{\psi} \right] + \dot{V}_{ic} \left(\Delta\rho_c + \frac{\alpha\rho_{ic} L}{c_P} \right) \left[\bar{\psi} - \psi(R_i) \right] \quad (3.12)$$

where ψ is gravitational potential, $\bar{\psi}$ is average gravitational potential in the outer core, $\dot{V}_{ic}$ is the rate of change of inner core volume, $\Delta\rho$ is the difference between inner and out core density due to composition (i.e., excluding state change), ρ_{ic} is inner core density, and L is latent heat of fusion. Superadiabatic heat flow across the core-mantle boundary is given by $Q^*_{CMB} = Q_{CMB} - Q_{ad}$, where $Q_{ad} = 16\pi^2 G\rho_{oc}\alpha_c T_c k_c R_c^3/3c_{P,c}$ and k_c is thermal conductivity.

Following Christensen (2010), we estimate the dynamo's magnetic field strength by assuming a balance between Ohmic dissipation and available power:

$$\frac{B^2}{2\mu_0} = cf_{ohm}\frac{R_c}{U}\phi \tag{3.13}$$

where B is the magnetic field strength within the core, μ_0 is magnetic permeability, c is a constant of proportionality, f_{ohm} is the fraction of dissipated power converted to magnetic energy, and U is the characteristic velocity. ϕ is the volumetric thermodynamically available power, $\phi = \Phi/V_{oc}$, where V_{oc} is the volume of the liquid outer core. We assume $f_{ohm} \approx 1$, which is the case when viscosity is negligible as is usually assumed in planetary cores (e.g., Christensen and Aubert, 2006; Roberts and Aurnou, 2012).

We use three scaling laws derived in Christensen (2010) to estimate velocity U. Although the scalings are derived for thermal convection, they are applicable to a thermochemical dynamo as well since the difference in buoyancy source only affects the available power for convection, not the form of the force balance equations.

Mixing length (ML) theory assumes a balance between inertial and buoyancy forces. Following Christensen (2010) but generalizing from thermal convection, we find $U = (\phi R_c/\rho_{oc})^{(1/3)}$. Combining this expression with Eq. (3.13), we find

$$B^2_{ML} = 2\mu_0 c(\rho_{oc}R_c^2\phi^2)^{1/3} \tag{3.14}$$

The MAC (Magneto-Archimedes-Coriolis) scaling assumes a balance between Lorentz, gravitational and Coriolis forces. This balance yields a characteristic velocity $U = (\phi/\rho_{oc}\Omega)^{1/2}$, where Ω is the Moon's angular velocity, and magnetic field magnitude

Name	wt. % S	μ_0 (Pa s)	$\Delta\rho$ (kg m^{-3})	B_{ML} (μT)	B_{CIA} (μT)
Reference model	5	10^{20}	0	0.53	0.90
LS2μ20$\Delta\rho$0	2	10^{20}	0	0.54	0.89
LS8μ20$\Delta\rho$0	8	10^{20}	0	0.43	0.75
LS5μ19$\Delta\rho$0	5	10^{19}	0	0.64	1.0
LS5μ21$\Delta\rho$0	5	10^{21}	0	0.37	0.63
LS5μ20$\Delta\rho$45	5	10^{20}	45	0.52	0.87
LS5μ20$\Delta\rho$90	5	10^{20}	90	0.33	0.58

Table 3.2: Varied model parameters and the resulting maximum magnetic field amplitudes for the ML and CIA velocity scalings. Reference viscosity refers to viscosity at 1300° C.

$$B_{MAC}^2 = 2\mu_0 c(\rho_{oc} R_c^2 \Omega\phi)^{1/2} \tag{3.15}$$

Finally, assuming a balance of Coriolis, inertial, and gravitational forces (the CIA scaling) yields $U = (\phi/\rho_{oc})^{2/5}(R_c/\Omega)^{1/5}$ and

$$B_{CIA}^2 = 2\mu_0 c(\rho_{oc}^2 R_c^4 \Omega\phi^3)^{1/5} \tag{3.16}$$

Poloidal components of the magnetic field will reach the surface while toroidal components will not. Although the partitioning of energy into these components is not known, we apply a commonly used multiplier of one seventh to estimate the dipole component of the magnetic field B at the CMB (Christensen and Aubert, 2006). The surface field is thus estimated as $B_{surf} = (1/7)B(R_c/R)^3$.

3.3 Results and discussion

We discuss seven core models run to present day. First we discuss the core heat flux budget, and compare surface flux with observations. Then we discuss the effects sulfur content and mantle parameters have on the core and dynamo. Finally, we consider the sensitivity of dynamo estimates to small changes in heat flow and in assumed adiabatic heat flow values.

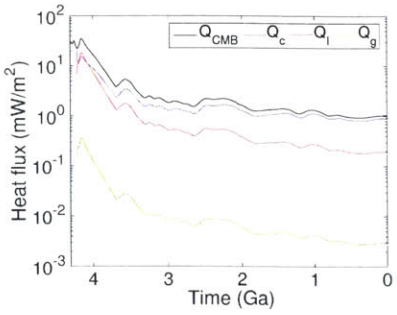

Figure 3-3: Core-mantle boundary heat flux and the contributions to it from secular cooling (Q_c), latent heat (Q_l), and gravitational energy release (Q_g) for the reference model. Note these terms, expressed in the Methods section in dimensions of power, are converted to power per area for ease of comparison with similar studies. When core solidification begins, the latent heat contribution is comparable with secular cooling; however, the latter becomes dominant as sulfur concentration increases. With higher sulfur concentration, the solidification of a unit volume of inner core increases outer core sulfur content more quickly, thus requiring a larger concurrent temperature decrease.

3.3.1 Core and mantle heat fluxes

Figure 3-3 exemplifies the typical evolution of heat flux across the core-mantle boundary and the amount of heat provided by secular cooling, latent heat, and release of gravitational potential energy. The last of these is negligible in all cases. At the onset of core solidification, the power budget from secular cooling and latent heat are roughly comparable. However, solidification proceeds quickly initially, and later solidification is slow since it can only proceed after the core has cooled due to the strong dependence of solidus temperature on sulfur content. Thus after the initial stage of solidification, most heat flux out of the core comes from secular cooling, and the resulting temperature decrease in turn lowers core-mantle heat flow.

Our results differ significantly from those of Laneuville et al. (2014). In their model, latent heat composes the vast majority of the heat flow budget out of the core during its solidification, while secular cooling contributes little. In contrast, our core temperature and heat flow decrease quickly, predicting a dynamo shutoff due to lack of available power. The discrepancy between our results occurs because the authors neglected the partial derivative of the solidus with respect to sulfur content in their

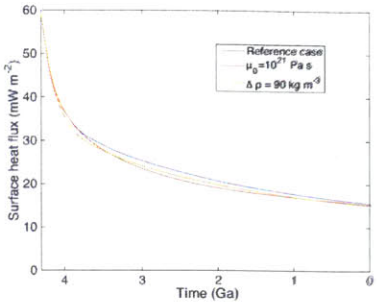

Figure 3-4: Surface heat flux for various model parameters. The present-day model heat flux of 15 mW m^{-2} is consistent with the Apollo heat flow measurements of 21 and 16 mW m^{-2} (Langseth et al., 1976; Grott et al., 2010), though it has been argued these measurements are above the global average, which may be as low as 12 mW m^{-2} (Rasmussen and Warren, 1985). Our result does not vary significantly in the parameter space explored.

equation for inner core growth rate. This led to a large underestimate of core growth. When the dependence was included, they found larger inner cores and no present-day dynamo (Laneuville, personal communication). Laneuville et al. (2014) also discuss the possible transition from an outwardly solidifying core to an iron snow regime that would disable the dynamo. Such a transition could result in an earlier shutoff time than we otherwise predict. However, as they note, the timing of this transition is not well-constrained.

Present-day surface heat flux can be compared with Apollo measurements at the Apollo 15 and 17 sites that produced values of 21 and 16 mW m^{-2} (Langseth et al., 1976; Grott et al., 2010). Rasmussen and Warren (1985) argue that these locations were not representative and instead estimate a global average value of 12 mW m^{-2} after adjusting for the measurement sites' proximity to the highlands/mare boundary. Our models result in a present-day heat flow of 15 mW m^{-2}, consistent with these values (Fig. 3-4). Our value does not vary significantly in the parameter space explored.

3.3.2 Effect of core sulfur content

Mantle dynamics are not significantly affected by changes in initial core sulfur content. Figure 3-5 shows core temperature, inner core growth, thermodynamically available power for the dynamo, and the resulting magnetic field estimates for initial core sulfur contents of 2, 5, or 8 wt.%. For the same mantle conditions, a low-sulfur core will begin solidification earlier due to its higher solidus temperature. Such a core will initially solidify more quickly since its higher temperature results in a larger CMB heat flux than a high-sulfur core. This difference results in later thermal evolution of the core being independent of initial sulfur content (Fig. 3-5b). However, since inner core size is strongly controlled by initial sulfur content, the power Φ available to a dynamo is still affected.

Maximum field strength, which occurs at the onset of core solidification, is affected by initial sulfur content in two ways. First, when sulfur content is high, solidification begins at a lower temperature. The lower heat flux in this scenario results in a weaker dynamo. However, since the inner core contribution scales with density contrast, higher sulfur content results in an increased inner core contribution to the total available power. Combined, these effects resulted in a 20% weaker field for the 8 wt.% model, while the 2 and 5 wt.% models showed negligible difference. Dynamo longevity was not significantly affected.

3.3.3 Effect of mantle parameters

Increasing mantle viscosity reduces the mantle's ability to convect away its radiogenic heating. Compared to the reference case, using a reference viscosity of $\mu_0 = 10^{21}$ Pa s results in a later peak mantle temperature, which suppresses core heat flow (see Fig. 3-6). When the mantle begins cooling, a brief increase in core heat flow could potentially revive a short-lived dynamo. However, the warmer, more viscous mantle present in this scenario limits core heat flow and dynamo potential. Conversely, a low-viscosity mantle with $\mu_0 = 10^{19}$ Pa s results in high heat flow and a cooler core.

Introduction of a 300-km layer in the lower mantle 45 kg m^{-3} more dense than

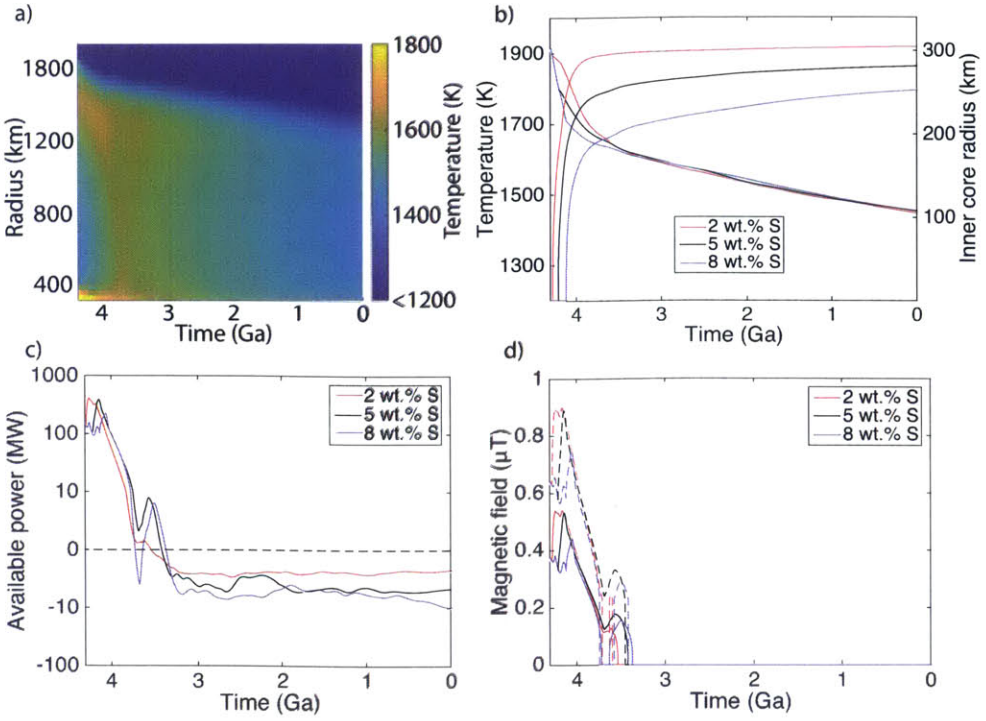

Figure 3-5: Effect of initial core sulfur content on core evolution. a) Thermal evolution of the mantle for the reference model. Sulfur content does not significantly affect mantle evolution. b) Inner core radius and CMB temperature. A larger sulfur content results in a smaller inner core but does not ultimately affect temperature. c) Power available to a dynamo. Note that the plot is distorted. To display both detail near $\Phi = 0$ and the full range observed, the plot is linear between -10 and 10 MW, and logarithmic outside this range. d) Predicted surface fields using the ML (solid) and CIA (dashed) scalings. Lower sulfur content results in a higher peak because the initiation of solidification occurs at a higher temperature and thus coincides with high heat flux.

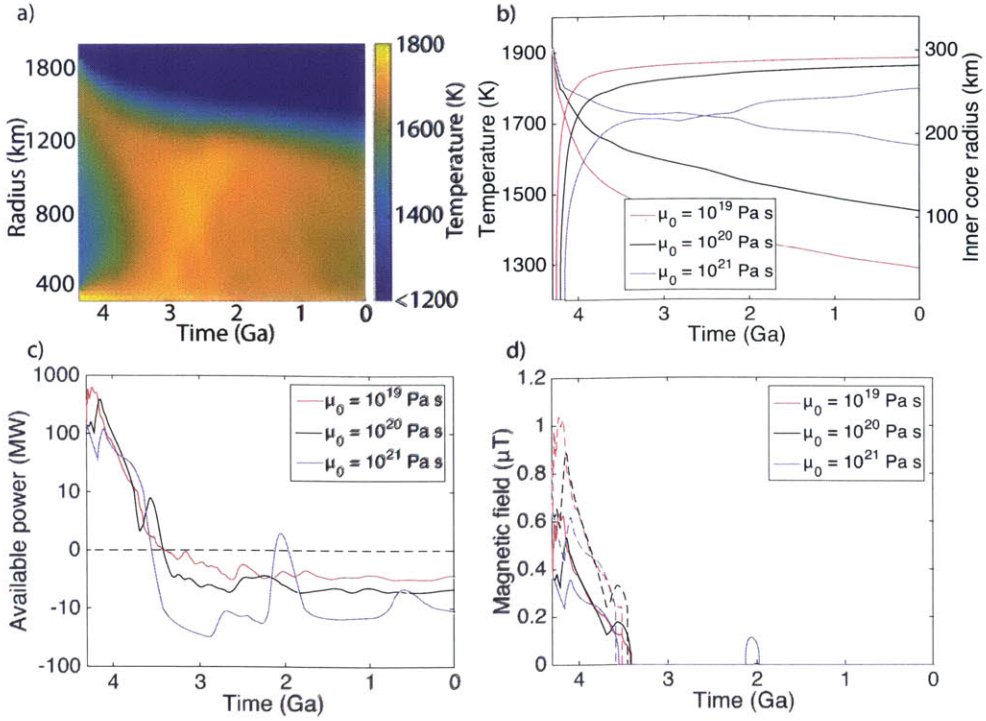

Figure 3-6: Effect of mantle viscosity on core evolution. a) Thermal evolution of the mantle for a reference viscosity of 10^{21} Pa s. b-d) See Figure 3-5 for explanation. Higher viscosity delays cooling and heats the mantle by radiogenic decay. When cooling begins again, a surge in core heat flow can produce a brief resurgence of the magnetic field. Lower viscosities result in overall higher heat flow and thus lower core temperature.

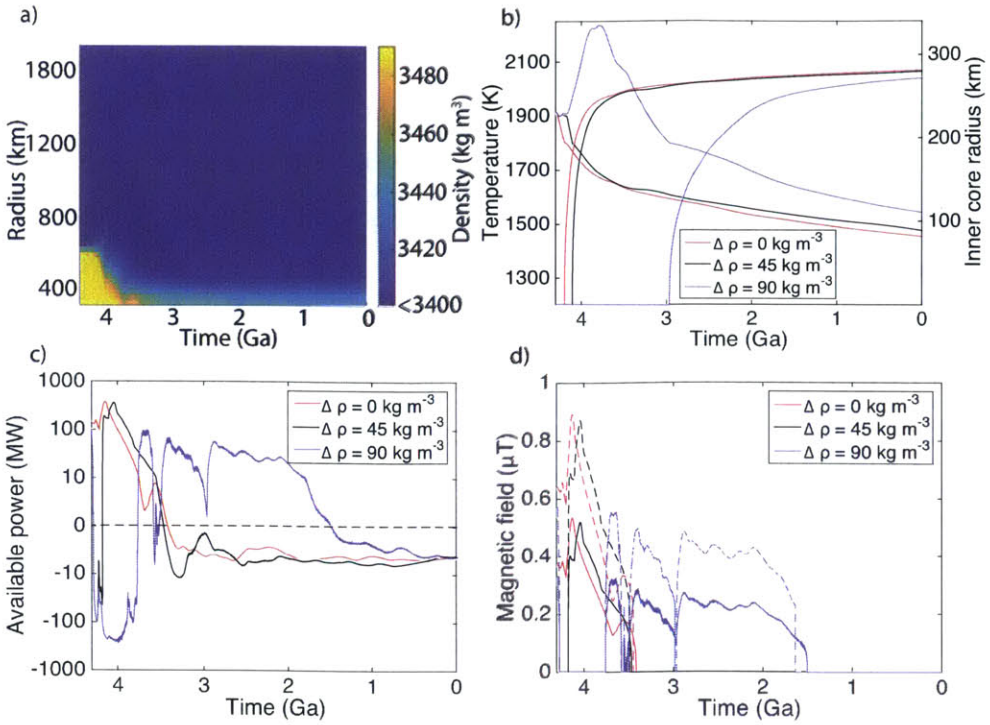

Figure 3-7: Effect of a thermal blanket on core evolution. a) Density evolution of the mantle with a lower layer of 90 kg m^{-3} excess density. b-d) See Figure 3-5 for explanation. While a layer of $\Delta\rho = 45$ kg m^{-3} makes little difference, $\Delta\rho = 90$ kg m^{-3} inhibits heat flow out of the core. Even once most of the layer has become well-mixed with the mantle, the subsequent gradual heat flow results in a prolonged dynamo lifetime.

the surrounding mantle causes minor changes to core behavior (Fig. 3-7b-d). Radiogenic heating and its consequent thermal expansion make the layer buoyant within 100 million years. The layer delays the onset of core solidification, but does not noticeably affect the dynamo in any other way in comparison with a homogenous mantle composition.

A thermal blanket of density 90 kg m^{-3} greater than the surrounding mantle produces more stark differences. Consistent with Zhang et al. (2013), it delays the onset of a core dynamo by ~500 million years. Furthermore, even after the majority of this layer is able to mix with the surrounding mantle, enough remains behind at the core-mantle boundary to limit heat flow, distributing core growth over time and enabling a relatively long-lived dynamo. Although this model looks promising, the

high temperatures reached in the thermal blanket due to radiogenic heating, over 2200 K, would produce widespread melting. Our solid-state mantle model does not account for this effect. The primary result of melting would be a significantly more efficient heat flow and cooling within the mantle while the temperature is above the layer's solidus. This increase in early mantle heat loss would reduce the delay in dynamo onset.

While our model begins at 4.3 Ga presuming a long-lived magma ocean (Meyer et al., 2010), the assumption of faster magma ocean solidification (Elkins-Tanton et al., 2011b) would shift the mantle timeline and thus core evolution backward by as much as 200 m.y. Although shifted in time, model evolution would be almost identical: the timing affects the model only by altering the magnitude of radiogenic heating by a few percent, which was found to have a minimal impact. An earlier magma ocean solidification time could better align the dynamo produced in the dense thermal blanket scenario with the timing of the observed early magnetic field.

3.3.4 Magnetic field magnitude

The maximum magnetic field estimates in our models were 0.64 and 1.0 μT using the ML and CIA scalings, respectively. The MAC scaling produced magnetic Reynolds numbers that were insufficient to ever produce a dynamo. The ML value is consistent with field strength estimates made by Laneuville et al. (2014) and Evans et al. (2014), who employ a similar scaling.

However, all scaling estimates fall far short of the likely 70 μT inferred from paleomagnetic samples during the high-field epoch recorded between 4.2 and 3.19 Ga. Even when our models result in a long-lived dynamo, model field strength is an order of magnitude lower than paleomagnetic estimates of the field after 3.19 Ga. As noted in the Introduction, however, paleomagnetism in this low-field epoch is consistent with a null field and thus also with our results.

A larger core (e.g., Evans et al., 2014) would help reduce the discrepancy in magnetic field strength during the high-field epoch somewhat, since the surface field scales with the cube of core size. Additionally, while we assume that the magnitude

of the dipole field was one seventh of total field magnitude, the partitioning of the field into the dipole and other components is not well-constrained. However, most parameters used in the scaling estimates are raised to fractional powers and thus uncertainties in them do not dramatically affect field strength estimates. For example, one significant unknown in the CIA scaling is rotation rate Ω, but the magnetic field scales as $B \sim \Omega^{0.1}$, meaning that even if rotation rate were an order of magnitude higher than present day, the field would increase by only 26%. Similarly, since field strength is proportional to the cubic root of power in the ML scaling, a 1000x increase in power would only raise the field estimate by a factor of ten.

The reliability of the scaling laws adopted here is a significant unknown and may not apply to the early lunar dynamo. However, the difficulty in matching the complete set of lunar paleomagnetic data faced in our and similar studies suggests that a core dynamo driven solely by thermochemical convection is not the only source of the magnetic field during the early high-field epoch.

3.3.5 The sensitivity of dynamo scaling models to adiabatic heat flow

Lunar core-mantle models commonly feature an early rapid decrease in core heat flow, after which Q_{CMB} decreases only very slowly up to present day (Evans et al., 2014), or even increases (Laneuville et al., 2014). In the case of purely thermal convection, the threshold heat flow needed to provide nonzero power for a dynamo is $Q_{CMB} = Q_{ad}$. If Q_{CMB} is relatively constant and near Q_{ad} over a long time range, then a change in the assumed parameters that determine adiabatic heat flow can drastically influence the timing of dynamo shutoff. For example, in some instances in Evans et al. (2014), doubling the adiabatic heat flux estimate would reduce the field's longevity from 1.8 b.y. to 200 m.y. The same sensitivity will exist in a thermochemical dynamo, though an expression for the threshold heat flow value must include an effective heat flow accounting for solidification.

Adiabatic heat flux (in power per area) is given by:

$$q_{ad} = \frac{4\pi G \rho_{oc} \alpha_c T_{CMB} k_c R_c}{3 c_{P,c}}. \tag{3.17}$$

A range of values is used within the literature. Stegman et al. (2003) use ~5-9 mW m^{-2}. (However, they assume a 450-km core; all other parameters unchanged, a 330-km core would yield ~4-7 W m^{-2}.) Laneuville et al. (2014) use ~10 mW m^{-2}, while Zhang et al. (2013) find a similar ~9 mW m^{-2}. Evans et al. (2014) find an adiabatic heat flux of 2.3 mW m^{-2}. Our adiabatic heat flux ranges from 5-6.5 mW m^{-2}, depending on temperature.

The differences in these values result primarily from choice of thermal conductivity and thermal expansivity. Assumptions of thermal conductivity vary from 25 to 50 W m^{-1} K^{-1}. The lower value is supported experimentally by Anderson (2003), who suggests 28-44 W m^{-1} K^{-1} in the Earth's outer core. de Koker et al. (2012) calculate a value of ~50-60 W m^{-1} K^{-1} for the lunar pressure and temperature range.

Choices of thermal expansivity range from $5.85 \cdot 10^{-5}$ to $1.12 \cdot 10^{-4}$ K^{-1}. Typical experimental values range from $8.2 \cdot 10^{-5}$ K^{-1} to $1.32 \cdot 10^{-4}$ K^{-1} (Hixson et al., 1990; Nasch and Steinemann, 1995; Assael et al., 2006) for molten iron. Introduction of light elements may lower this value significantly. However, it seems unlikely to lower thermal expansivity below the thermal expansion coefficient of solid FeS, $6.85 \cdot 10^{-5}$ K^{-1} (Fei et al., 1995; Riner et al., 2008). Note that $5.85 \cdot 10^{-5}$ K^{-1} has also been employed in recent studies (Dwyer et al., 2011; Evans et al., 2014); this value follows from Williams and Nimmo (2004) to ensure that inner core solidification occurs in their Mars model, and does not appear to be supported experimentally at lunar temperatures and pressures.

Figure 3-8 compares available power and the resulting magnetic field for our reference model using the thermal conductivity and expansivity assumed throughout this study (50 W m^{-1} K^{-1} and $9 \cdot 10^{-5}$ K^{-1} respectively; see Table 3.1) with the same model adopting the lower values of $k_c = 25$ W m^{-1} K^{-1} and $\alpha_c = 7 \cdot 10^{-5}$ K^{-1}. Using the latter parameters, the lifetime of our reference model's dynamo extends nearly to present day.

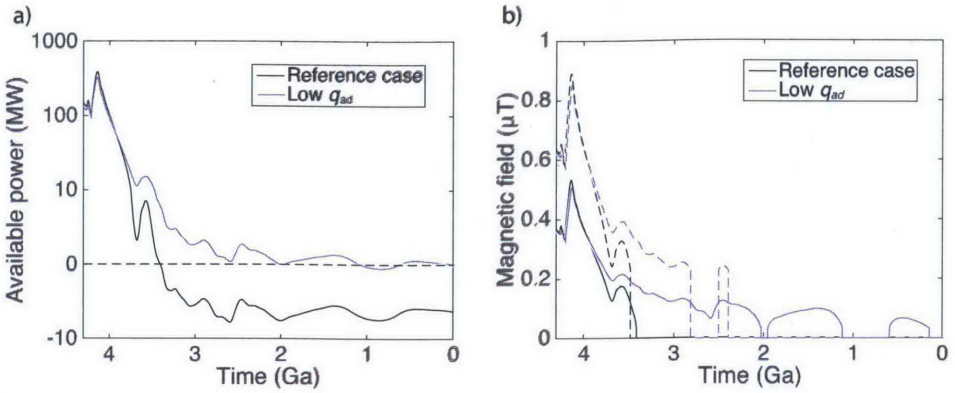

Figure 3-8: Effect of adiabatic heat flow parameters on magnetic field evolution for the reference model. See Figure 3-5 for explanation. The low q_{ad} case demonstrates the impact on the magnetic field of using $\alpha_c = 7 \cdot 10^{-5}$ K^{-1} and $k_c = 25$ W m^{-1} K^{-1}. See text for details.

3.3.6 Possibility of a 'start-stop' dynamo

If adiabatic heat flow is near a value such that available power for the dynamo remains near zero for a long period of time, the existence of a dynamo may also be sensitive to small variations in heat flow. Changes in convection pattern as mantle convection adjusts to the thickening lithosphere and decreasing heat flow cause bumpiness in the heat flow (Fig. 3-3). Convective velocity, and the magnetic Reynolds number and magnetic field strength into which it factors, is sensitive to small changes in heat flow.

This presents an interesting possibility in the system's evolution. As core convection slows, a small short-term reduction in heat flow could temporarily inhibit the dynamo, causing a temporary disappearance of the field before heat flow returns to a sufficient value (Fig. 3-9). These gaps in field presence could complicate interpretation of the paleomagnetic record. It may also offer some explanatory power. Weiss and Tikoo (2014) note that the records of an extremely recent (<200 Ma) lunar magnetic field require that we be in a "special time window" occurring just after the dynamo's cessation. A 'start-stop' dynamo would lessen the need to consider the present time period special. This hypothesis also opens the possibility that the lunar dynamo may reactivate in the future.

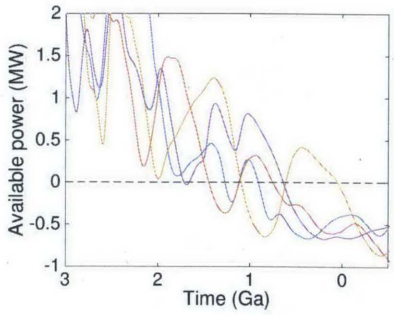

Figure 3-9: Power available to a dynamo in several randomly perturbed runs of the reference model using the core parameters $\alpha_c = 7 \cdot 10^{-5}$ K and $k_c = 25$ W m^{-1} K^{-1}. Heat flow does not necessarily decrease steadily. Minor variation in heat flow rate has little effect on core temperature or solidification as a function of time, but causes fluctuations in the power available to a dynamo that become significant near the threshold for dynamo action.

3.4 Conclusion

Our coupled mantle-core evolution models demonstrate that convection driven by inner core growth can explain the longevity of the Moon's dynamo without appealing to additional mechanisms or solidification regimes to excite core flow or deactivate the dynamo. Using our preferred values for thermal expansivity and thermal conductivity, the dynamo was found to extend to 1.6 Ga. The field duration can be extended nearly to present day if less probable, but still realistic, thermal expansivity and conductivity values are assumed for the core. Mantle characteristics may also impact the duration of the dynamo. High mantle viscosity can cause a warmer mantle that inhibits heat flow, potentially allowing dynamo action later as the mantle cools. In contrast, a thermal blanket extends the dynamo lifetime, but also delays its onset.

Paleomagnetic measurements suggest an ancient, high intensity ($\sim$70 μT) lunar dynamo and subsequent reduction in amplitude to $\lesssim$10 μT later in lunar history. Our results are consistent with observations of a weak-field epoch following a strong-field epoch, but a substantial discrepancy exists between our field magnitude in both epochs. Although there is uncertainty in core composition, physical parameters, and scaling laws, it is difficult to reconcile this difference, which renders it unlikely that thermochemical convection alone can explain the early field intensity.

High sensitivity to an uneven heat flow rate at the core-mantle boundary could cause the dynamo to stop and restart in its late stages. Future paleomagnetism studies investigating the demise of the dynamo could reveal any start-stop field behavior in the paleomagnetic record.

Acknowledgements

Thanks to coauthors K. Soderlund and G. Schubert. We also thank N. Zhang, M. Laneuville, A. J. Evans, L. T. Elkins-Tanton, and our reviewers for thoughtful discussions and comments. This work was funded with NSF grant no. 0909206.

Chapter 4

Timescale and morphology of Martian mantle overturn following magma ocean solidification

Abstract

Energy of accretion in terrestrial planets is expected to create liquid silicate magma oceans. Their solidification processes create silicate differentiation and set the initial mantle structure for the planet. Solidification may result in a compositionally unstable density profile, leading to cumulate Rayleigh-Taylor overturn if a sluggish rather than stagnant lithosphere existed in the early stages of planetary history. The pattern and timescale of overturn, in which cold, dense surface material sinks to the core-mantle boundary, have implications for core dynamo production, volatile escape and fundamental differences among differently sized bodies. Our fully spherical mantle models reaffirm previous work suggesting that harmonic degree of overturn is dependent on viscosity contrast and layer thickness. We find that cumulate overturn would likely have occurred with short wavelengths. In an isoviscous model, thermal convection ensues rapidly after overturn; however, when viscosity is temperature dependent, compositional stability in the mantle suppresses the onset of whole-mantle thermal convection. For a viscosity of 10^{18} Pa s, the mantle could fully overturn in as little as 3 Ma.

4.1 Introduction

Estimates of gravitational potential energy converted into heat during Martian planetary accretion are as high as $4 \cdot 10^{30}$ J, more than sufficient to melt the entire silicate mantle and produce a magma ocean (Wetherill, 1990). Given the short time period over which accretion may have occurred ($\sim 10^5$ years, Wetherill, 2000) and further heating from radioactive decay and core differentiation, Mars's mantle may have become wholly or partially molten (e.g., Solomon, 1979). The depth of this magma ocean is still not well-constrained, with estimates based on geochemical evidence varying from 700 km (Righter et al., 1998) to greater than 1350 km (Debaille et al., 2008). Isolated magma ponds due to large impacts are also a possibility (Tonks and Melosh, 1993). In this study we consider the endmember case of a completely melted mantle.

A magma ocean is likely to become homogenous and adiabatic through convection. As the mantle's adiabatic temperature profile cools, the mantle will begin to crystallize. This will occur where the temperature profile intersects the solidus, initially at the base of the mantle and moving upward as the mantle continues to cool. These newly formed minerals are denser than the homogenous liquid and will thus precipitate out of the magma ocean and form layered cumulates (Martin and Nokes, 1989; Marsh, 1995). The change in bulk composition in the liquid as cumulates solidify will result in a nonuniform density profile by the time the entire mantle has resolidified (Elkins-Tanton et al., 2003). Magnesium-bearing minerals will crystallize preferentially, enriching the remaining melt in iron and, to a lesser extent, titanium and chromium. As the remaining progressively enriched melt solidifies, the resulting minerals will be progressively denser; this will result in a gravitationally unstable density profile.

At least until its later stages, the solidification of the magma ocean would likely occur before the solid material begins to equilibrate gravitationally, since the timescale of large-scale solid mantle advection is greater than that of fractional crystallization (Elkins-Tanton et al., 2005). Since heat advection has not significantly progressed,

temperatures immediately after solidification can be assumed to be the same as when the material solidified. The resulting temperature profile is the fractional solidification solidus. This temperature profile will enhance the gravitational instability and would possibly lead to overturn even in the absence of fractionation (Solomatov, 2000).

Provided a sufficiently low viscosity, the gravitationally unstable profile will result in spontaneous overturn of the mantle to reach a more gravitationally stable state. This process proceeds by Rayleigh-Taylor instability. Insights into the process can be made by considering the basic scenario in which a homogenous fluid is overlain with another homogenous fluid of higher density.

Computational and analytic studies in spherical geometry demonstrate that, for a given density structure, high viscosity contrast between layers results in a longer overturn wavelength (Parmentier et al., 2002; Zhong and Zuber, 2001; Ke and Solomatov, 2006). In a planetary interior, the longest wavelength, degree-one overturn, would correspond to a single large downwelling of dense material. Low viscosity contrasts result in higher degree overturn, with multiple smaller downwellings. However a full three-dimensional model calculation has not yet been performed to confirm that those cases could be relevant to planetary mantles. Layer thickness also influences wavelength of overturn (Zhong and Zuber, 2001). The thinner either layer becomes, the more difficult it is to acquire long-wavelength, degree-one instabilities.

Overturn and resulting mantle behavior could help explain puzzling characteristics of Mars. Degree-one overturn is of particular interest for Mars since the Martian crust demonstrates a degree-one dichotomy in (among other things) its remanent magnetization. While no dynamo is currently active in the Martian core, the northern hemisphere's crust is weakly magnetized, while the southern hemisphere's crust contains regions of both strong and weak magnetization (Zuber, 2001). Degree-one overturn may potentially explain these features. A degree-one cold downwelling which arrives at the core-mantle boundary (CMB) could result in a high heat flux from the core in a single hemisphere. It has been shown that this heat flux distribution on the CMB could force the liquid outer core into a mode of convection leading to the production of a single-hemisphere dynamo (Stanley et al., 2008). If it was active in

the southern hemisphere, such a dynamo could explain the observed remanent field. A giant impact has also been proposed as an alternative mechanism responsible for the dichotomy (e.g., Andrews-Hanna et al., 2008).

Chemical observations may also be explained by the overturn process. Isotopic studies of the SNC meteorites, believed to be of Martian crustal origin (e.g., Treiman et al., 2000), indicate that separate source reservoirs differentiated early on and remain separate (Jones, 1986; Borg et al., 1997). The nakhlite and chassigny meteorites point to a source region depleted in incompatible elements, while the source region inferred from several shergottites would have been enriched in them. Fractional crystallization of a magma ocean could explain the creation of these isotopic reservoirs. An overturn event could then separate and maintain them (Elkins-Tanton et al., 2005); however details of their formation, structure and behavior have yet to be understood.

Cumulate overturn will result in a more gravitationally stable mantle, which will initially stifle thermal mantle convection until the buoyancy force due to the thermal gradient is great enough to overcome compositional stability (Zaranek and Parmentier, 2004). The early stages of mantle history, from solidification to the eventual initiation of convection, may have a profound influence on the future development of a planet. Mantle behavior will govern the production of an early atmosphere through volatile escape and define the properties of an early crust (Elkins-Tanton, 2008). When and how thermal convection becomes dominant over chemical convection will vary greatly from planet to planet, as different fundamental characteristics (size, composition, etc.) determine how fractional crystallization will proceed and thus determine the relative strengths of chemical and thermal buoyancy.

This study simulates mantle dynamics in Mars from the completion of magma ocean solidification to a compositionally stable state and considers the lifetime of such a stably layered system. We will test previous two-dimensional work done on two-layer Rayleigh-Taylor overturn scenarios using a fully spherical geometry, and then explore possible overturn scenarios with more realistic planetary characteristics. In particular, we seek to (1) determine the spherical harmonic degree with which colder surface material advects downward during initial Rayleigh-Taylor overturn,

(2) estimate the increase in core heat flux due to the overturn, (3) determine the resulting distribution of chemically distinct zones within the mantle, and (4) constrain the timescale of overturn and of subsequent convection-driven compositional homogenization for different possible viscosity profiles.

4.2 Methods

4.2.1 Governing Equations

We model the mantle as an anelastic, incompressible viscous shell without phase transitions. We also make the Boussinesq approximation, which simplifies the equations by assuming that variation in density enters into them only through the buoyancy term (e.g., Christensen and Yuen, 1985; Roberts and Zhong, 2006). The mantle dynamics are thus governed by the following nondimensionalized equations for conservation of mass, momentum, and energy.

$$\nabla \cdot \vec{u} = 0 \tag{4.1}$$

$$-\nabla p + \nabla \cdot [\mu(\nabla \vec{u} + \nabla^T \vec{u})] + Ra(T - BC)\hat{r} = 0 \tag{4.2}$$

$$\frac{\partial T}{\partial t} + \vec{u} \cdot \nabla T = \nabla^2 T + H_{int} \tag{4.3}$$

where $\vec{u}$ is the velocity, p is the pressure, μ is the dynamic viscosity, and $\hat{r}$ is the radial unit vector. T is temperature nondimensionalized to be zero at the top surface and one at the bottom surface. We define the thermal Rayleigh number Ra as

$$Ra = \frac{\rho_o g \alpha \Delta T R^3}{\kappa \mu_o} \tag{4.4}$$

where ρ_o is a reference density, g is gravitational acceleration, assumed here to be constant, α is the thermal expansivity, ΔT is the superadiabatic temperature difference across the entire model, R is the radius, κ is the thermal diffusivity, and

μ_o is the reference viscosity at the core-mantle boundary of the model. Note that our nondimensionalizations use R as the characteristic length scale rather than mantle thickness.

The buoyancy ratio B describes the relative size of density differences due to thermal expansion versus variation in chemical density,

$$B = \frac{\Delta\rho_{ch}}{\rho_o \alpha \Delta T}. \tag{4.5}$$

where $\Delta\rho_{ch}$ is the density range due to composition alone. C is a nondimensional material property between 0 and 1, where $C = 0$ denotes the least dense material and $C = 1$ denotes the most dense material. The transport equation for the chemical composition field is described by

$$\frac{\partial C}{\partial t} + \vec{u} \cdot \nabla C = 0. \tag{4.6}$$

H_{int} is the internal heating term, given by

$$H_{int} = \frac{QR^2}{c_P \Delta T \kappa}, \tag{4.7}$$

where Q is the volumetric heating rate. For simplicity, a constant internal heating is used. However, fractional crystallization would have concentrated radiogenic elements in the upper layer of the mantle, thereby reducing near-surface viscosity and facilitating the overturn process. We consider both the isoviscous case and a temperature- and pressure-dependent viscosity with an Arrhenius rheology, given by

$$\mu = \mu(T, z') = \mu_o exp\left(\frac{E' + V'z'}{T + T_{off}} - \frac{E' + V'(1 - R'_{CMB})}{1 + T_{off}}\right) \tag{4.8}$$

where $T_{off} = \frac{T_{surf}}{\Delta T}$, T_{surf} being surface temperature, and E', V', and z' are nondimensionalized activation energy, activation volume and depth, respectively (Roberts and Zhong, 2006). R'_{CMB} is the nondimensionalized radius of the core. μ is capped at $\mu = \mu_o \cdot 10^6$. Tables 4.1 and 4.2 record the fixed and varied input parameters, respectively.

Parameter	Description	Value	Unit
R	Radius	$3396{\cdot}10^3$	m
R_{CMB}	Core radius	$1396{\cdot}10^3$	m
ρ_o	Reference density	3350	kg m^{-3}
$\Delta\rho_{ch}$	Chemical density variation	130	kg m^{-3}
g	Reference gravity	3.71	m s^{-2}
c_P	Specific heat	1250	J kg^{-1} K^{-1}
κ	Thermal diffusivity	$1{\cdot}10^{-6}$	m^2 s^{-1}
α	Thermal expansivity	$3{\cdot}10^{-5}$	K^{-1}
V	Effective activation volume	$1.7{\cdot}10^{-6}$	m^3 mol^{-1}
T_{surf}	Surface temperature	573	K
T_{CMB}	CMB temperature	2467	K
H	Radiogenic heating rate	$4{\cdot}10^{-8}$	W m^{-3}
B	Buoyancy ratio	0.818	-

Table 4.1: Mars model parameters

4.2.2 Model

The governing equations are solved with the finite element method using CitcomS, which performs these calculations in 3-D spherical geometry (Zhong et al., 2008). The model, a spherical shell, is divided into 12 identically shaped caps. Each cap is divided into a $48 \times 48 \times 48$ grid, at every node of which the equations are solved. For the Mars geometry assumed here, this results in a vertical resolution of about 40 km and a horizontal resolution of about 30 km at the CMB and 80 km at the surface. Calculations are distributed across 24 processors. Tracers, tracked particles spread throughout the model that are entrained in and move with the fluid flow, contain compositional density information used to calculate chemical buoyancy. Tracers also contain information on their initial position in the model, in order to differentiate between two materials with equal density but diverse mineralogy.

Both the bottom and the top boundaries of the shell are isothermal and free slip. These model boundaries correspond to the physical boundaries with atmosphere and liquid outer core, respectively, both of which are considered low-viscosity isothermal reservoirs over the timescales of interest. Thus, the model is cooled from above while being heated basally and internally. No crust is modeled.

4.2.3 Initial Conditions

Two sets of calculations are made. The first set models two-layer Rayleigh-Taylor overturn to test the results by Zhong and Zuber (2001) that predict an increased overturn wavelength with larger viscosity contrast and layer thickness. The second set models a more complex Rayleigh-Taylor instability scenario that could have arisen after the fractional solidification of a whole-mantle Martian magma ocean.

Two-layer Rayleigh-Taylor Overturn

In the two-layer calculations, an isoviscous high-density layer is initially underlain with an isoviscous low-density layer. All thermal aspects of the model are removed, such that all buoyancy is chemical. In this manner we can study the simple case of a two-layer Rayleigh-Taylor instability in three-dimensional spherical geometry. Two parameters that can affect wavelength of overturn are μ_u/μ_l, the ratio of viscosities of the top and bottom layers, and r_i, the radius of the interface between the layers.

First, calculations are run in which the interface is given an initial perturbation of varying degree l (order $m = 0$). The fastest growing of these perturbations is the most unstable wavelength for the given viscosity and thickness parameters. Then, calculations are run which have no initial perturbation in the interface apart from small variations in density due to the randomized nature of tracer placement. These variations serve to initiate motion but do not appear to influence the resultant degree of overturn. μ_u/μ_l and r_i are varied independently and the most unstable wavelength is recorded for each case.

Overturn Model with Thermal and Chemical Profiles

Next we use the full model which includes thermal buoyancy and a range of chemical densities. The initial chemical density is uniform laterally but varies continuously with depth. This initial density profile (Fig. 4-1a) is the result of calculations of simple fractional crystallization reported by Elkins-Tanton et al. (2003) assuming that the entirety of the mantle was molten. The entire mantle is assumed to be at its

solidus temperature after magma ocean solidification (Fig. 4-1b). These two initial conditions can be made assuming the bulk of mantle ocean solidification occurs much quicker than convective and conductive timescales.

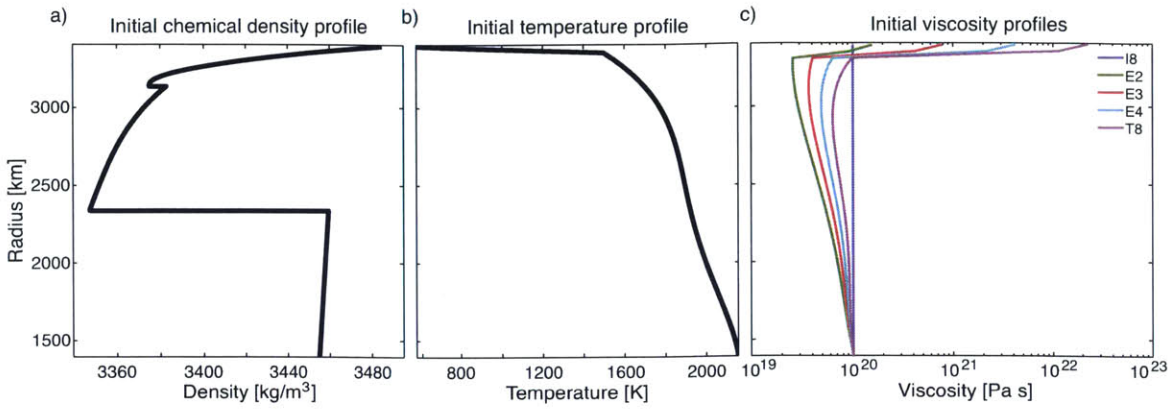

Figure 4-1: Initial conditions for the Martian mantle. (a) The thermal profile is the superadiabatic solidus temperature with a constant surface condition of 573 K. (b) The chemical density profile is the result of magma ocean solidification as calculated by Elkins-Tanton et al. (2005). c) Several viscosity rheologies were used to study the initial overturn. I8 (blue) and T8 (magenta), the isoviscous case and the case with the highest viscosity contrast, respectively, were continued and repeated with different Rayleigh numbers.

First we determine the harmonic degree of initial overturn that occurs provided five different viscosity profiles (Fig. 4-1c) created by adjusting activation volume V' and activation energy E' in Eq. (4.8). The degree is calculated by making a spherical harmonic analysis of radial velocity at each depth and averaging their powers weighted by velocity magnitude.

There are many possible metrics with which to measure the timescale of overturn. Here we choose to consider the density instability in the upper half of the mantle. We determine the time required for the density contrast across the unstable region to be reduced by 80%, and to be reduced by 98%. Thus overturn is 80% complete when

$$d\rho_{ch} \leq 0.2\Delta\rho_{ch}, \tag{4.9}$$

where $d\rho_{ch}$, the chemical density instability, decreases with time as overturn progresses.

The choice of rheology will fundamentally impact results. Experimentally determined mineral activation energies for diffusion creep range from 300-375 kJ/mol (Karato and Wu, 1993; Hirth and Kohlstedt, 2003). However, Christensen (1984) showed that when assuming a Newtonian rheology, the effective activation energy should be lowered by multiplying a prefactor of 0.3-0.6 to approximate non-Newtonian effects. In the case of the early Martian mantle, several other factors could work to temporarily reduce viscosity in the upper mantle. First, since the material is at its solidus, some degree of partial melt could likely be present, reducing viscosity. Second, the presence of water can also lower viscosity by several orders of magnitude (e.g., Hirth and Kohlstedt, 1996). Third, the gravitationally unstable upper layer would be enriched in radiogenic heat-producing elements. To demonstrate the effect of concentrated radiogenic heating, we construct a one-dimensional half-space diffusion model of the surface with concentrated radiogenic heating in the following section. As shown, cooling of the dense layers is significantly delayed. Combining these effects, a small viscosity contrast is plausible. We employ effective activation energies ranging from 0 kJ/mol (constant viscosity) to 78 kJ/mol in order to study the results of the low viscosity contrasts shown in Figure 4-1c. A larger viscosity with a stagnant lid will effectively prevent the gravitationally unstable layer from overturning altogether.

We choose a constant surface temperature of 300° C since the recently solidified magma ocean will be about 1200° C, but will cool quickly. Surface temperature was varied and found to affect the overall dynamics minimally (Fig. 4-2).

It is important to note that current models are unable to resolve systems with Rayleigh numbers corresponding to the viscosities possibly present in a recently solidified magma ocean. To address this issue, we use a scaling approach. We run models with more manageable Rayleigh numbers (10^6-10^8), which for fixed R and κ correspond to higher reference viscosities, and then extrapolate to higher Rayleigh numbers (lower viscosities). Thus, while the models use a large dimensional timescale over which assumptions of constant boundary temperature and low surface viscosity are not valid, the results can be scaled to apply to small timescales over which they

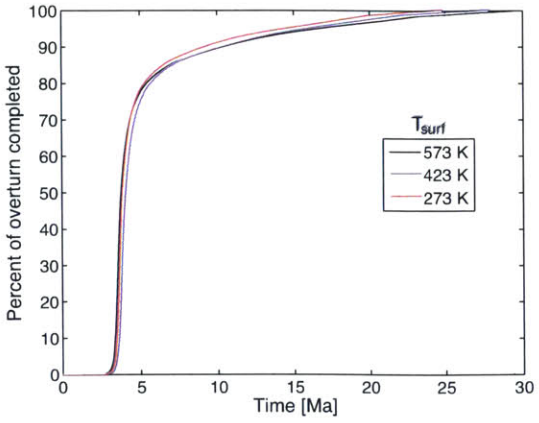

Figure 4-2: Normalized size of density instability as a function of time for the isoviscous case I8 for varied surface temperature. Changes in the surface boundary condition do not significantly alter the resultant timescales and scaling properties.

are valid.

Figure 4-3 demonstrates the dependence of overturn time on resolution. Timescales differed slightly between high-resolution and low-resolution results. While resolution may cause the prefactor to differ, the observed scalings are robust.

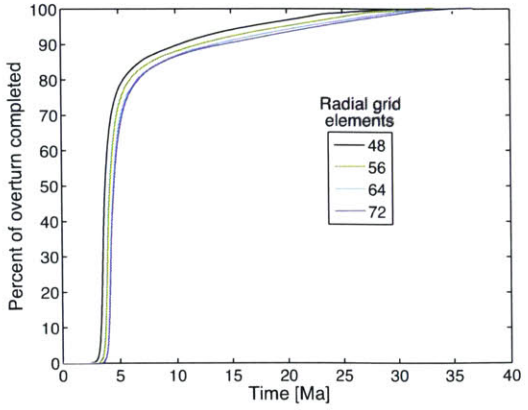

Figure 4-3: Normalized size of density instability as a function of time for the isoviscous case I8. Increasing resolution of each of the twelve model caps from a $48 \times 48 \times 48$ grid to a $72 \times 72 \times 72$ grid alters results slightly, but the change is convergent. While resolution may cause the prefactor to differ, the observed scalings are robust.

4.2.4 One-Dimensional Thermal Code

To demonstrate how radiogenic heating can maintain a high temperature in a lid produced by magma ocean solidification, we construct a 1-D conductive finite difference model of the upper 250 km of Mars governed by

$$\frac{\partial T}{\partial t} = \nabla^2 T + H_{int}. \tag{4.10}$$

The surface temperature is fixed at 300 K. The initial temperature everywhere else is 1600 K, and the base of the model at 250 km is fixed at this value. We assume initial chondritic values of radiogenic elements K, Th, and U, which become concentrated into the residual melt as fractional crystallization proceeds. If distributed evenly into the upper 250 km of Mars, they would be about 4.9 times chondritic abundance. We consider an even distribution and a distribution increasing monotonically with radius.

The results are shown in Figure 4-4. Without internal heating, the solution is an error function. If concentrated radiogenic heating is present, high temperatures, and thus low viscosities, will persist for hundreds of Ma.

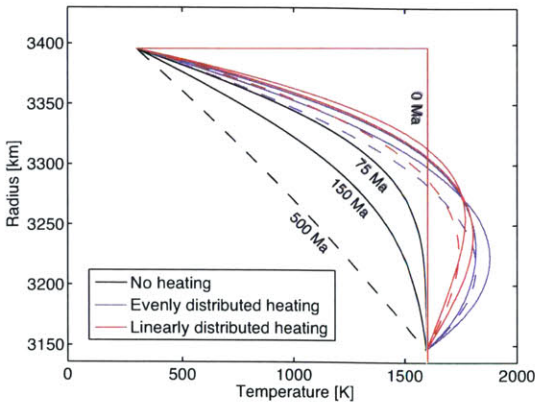

Figure 4-4: Temperature profiles for a 1-D finite difference model of the upper 250 km of the mantle. In the absence of concentrated radiogenic heating, conductive cooling quickly creates a stagnant lid. With radiogenic heating accounted for, high temperatures are prolonged enough that the high-density surface material will likely sink.

4.3 Results

Figure 4-5a shows example runs of the two-layer case in which a specific initial wavelength is introduced. These results are quantitatively and qualitatively consistent with the analytic solutions (Fig. 4-5b, from Zhong and Zuber, 2001). Wavelengths were somewhat shorter than found by Ke and Solomatov (2006), who mapped characteristic wavelengths assuming a thin unstable layer near the core-mantle boundary (CMB). Figure 4-6a shows the dominant harmonic degree of overturn as a function of interface radius and viscosity ratio. Degree-one overturn occurs only when significant viscosity contrast exists between adjacent layers. The thinner a layer, the more contrast is necessary for degree-one. For the case of $\mu_u/\mu_l = 1$, $l = 3$ overturn is the lowest achievable degree of overturn, but only if the layers are sufficiently thick (Fig. 4-6a). This is different from the analytical solution (Fig. 4-6b), which predicts $l = 4$ is the minimum achievable degree for those viscosity conditions; overall, however, our model matches the analytical solutions well qualitatively. Figure 4-6a was constructed from model calculations with a random initial perturbation, validating the assumption that the most unstable wavelength will generally come to dominate an overturn event.

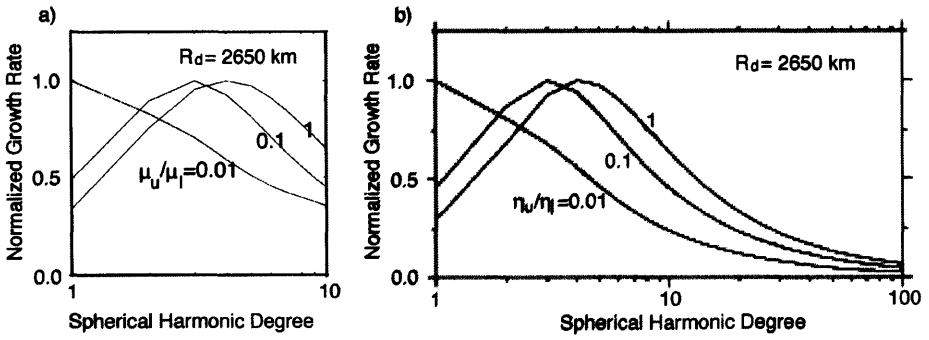

Figure 4-5: (a) The dependence of growth rate on degree of perturbation and viscosity contrast for an interface located at $R = 2650$ km. (b) Zhong and Zuber (2001) results for comparison.

For the predicted Martian thermal and chemical profiles, degree of overturn was more difficult to define than in the two-layer case, since there existed no well-defined

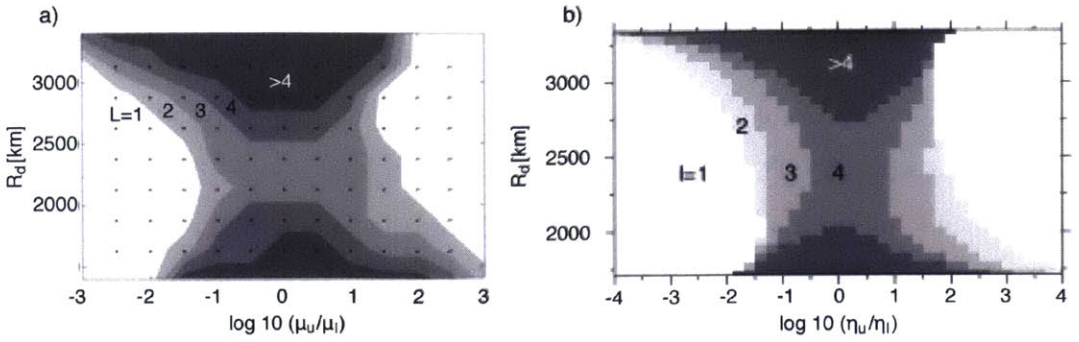

Figure 4-6: (a) The observed degree of overturn as a function of viscosity contrast and interface radius. At each black point, two calculations with randomized initial tracer location were made, and the average of their spherical harmonic decompositions were recorded. The contour lines are interpolated around those 77 points. (b) Zhong and Zuber (2001) results for comparison.

interface on which to perform a spherical harmonic analysis, and since degree also tended to vary with time. However, degree-one overturn was not observed for any of the viscosity parameters used in Figure 4-1. Rather, as recorded in Table 4.2, surface material arrived at the CMB in several cold, dense downwellings with a pattern of high degree (l = 5-9). In all cases, a perturbation initiated at the depth at which the local ratio of buoyancy forces to viscous resisting was highest, then expanded to other depths. In the isoviscous case, overturn initiated at the surface. In the temperature- and pressure-dependent viscosity cases, it initiated where viscosity was lowest, at near 400 km depth (Fig. 4-7b).

Models using a higher activation energy (300 kJ/mol) resulted in a stagnant lid in the enriched upper 250 km that did not overturn. The upper mantle beneath the lid was able to invert and homogenize, but this inversion did not cause any notable effect on CMB heat flow.

In the isoviscous calculations, the dense surface material was able to descend directly to the CMB, causing a surge of heat flux from the core (Fig. 4-8). For temperature-dependent rheologies, however, the high viscosity near the surface slowed the process. Material gradually seeped down, resulting in a smaller but more persistent overturn-induced heat flux. After initial overturn, the models stabilized into a dense lower mantle and a light upper mantle. Over time, convection in the upper

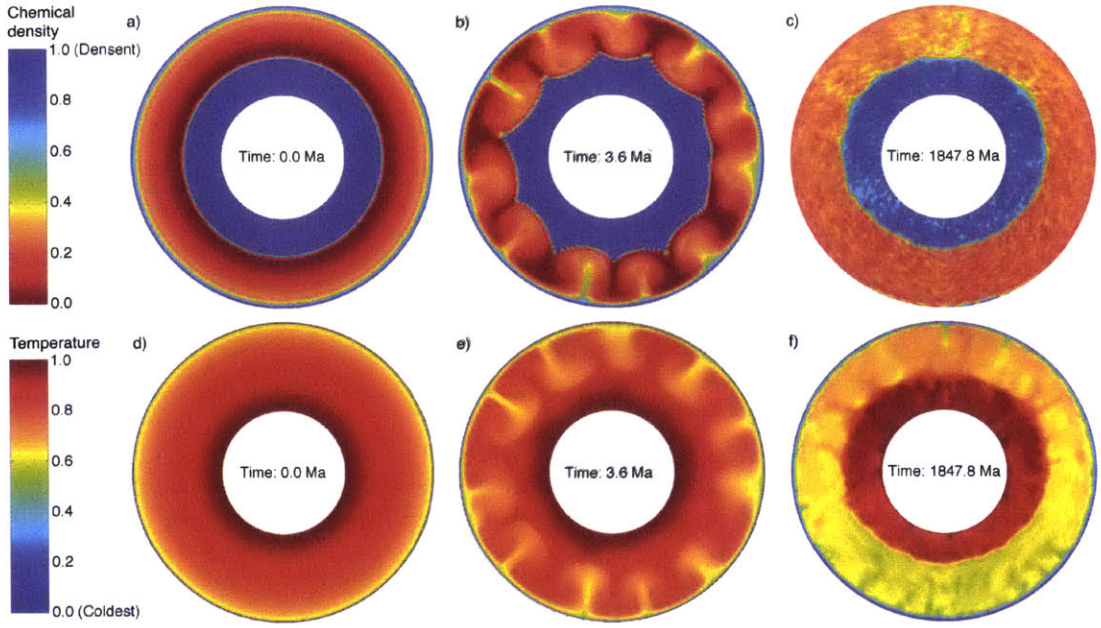

Figure 4-7: Overturn cross-sections in (a-c) chemical density and (d-f) temperature for temperature- and pressure-dependent rheology case T8. The cross-sections show the model at three times: initiation (a and d), early overturn (b and e), and completion of overturn (c and f).

region entrained dense material from underneath, eventually mixing the entire mantle (Fig. 4-9). During the entrainment period, convection occurs independently in the lower mantle as well, but the boundary between them is effectively conductive (Fig. 4-10), i.e., layered convection (e.g., Davaille, 1999).

Short-wavelength convection patterns dominated during the entrainment phase in all models (Fig. 4-11). In the isoviscous cases, small convection cells persist as the model continues into thermal convection. However, for the temperature- and pressure-dependent rheology, the transition to whole-mantle thermal convection was associated with the emergence of a degree-one convection pattern that persisted with stability as far as the model was run.

Figure 4-12 demonstrates overturn reaching the defined stages of completion in the isoviscous model. Because of its low temperature, some chemically light material was able to descend into the lower mantle despite having lower density. This effect

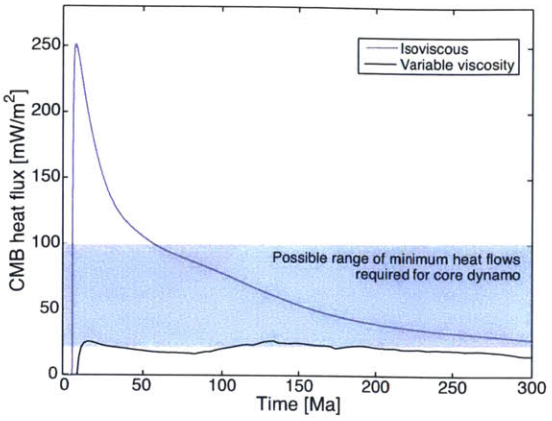

Figure 4-8: The initial impact on heat flux across the core-mantle boundary due to overturn for the temperature- and pressure-dependent rheology case T8 and the isoviscous case I8.

created a small chemical density instability in the lower mantle, which reequilibrated gradually as the material was heated conductively to the temperature of its new surroundings. Figure 4-13 shows the timescales observed for overturn of the upper mantle. Three scalings with reference viscosity were noted. First, 80% of overturn was complete in the isoviscous cases with timescale directly proportional to μ_0. Second, 98% was complete with timescale proportional to $\mu_0^{2/3}$. Third, in the temperature- and pressure-dependent viscosity cases, both overturn timescales scaled as $\mu_0^{4/3}$. While the bulk of the high-density material descended quickly, the rate of this process slowed significantly as the density instability lessened.

4.3.1 Entrainment and Whole-Mantle mixing

Although we show the entrainment process in Figure 4-9 for qualitative understanding, the actual entrainment rate is difficult to model with a global 3-D finite element framework since prohibitively high spatial resolution of upwellings is required for accurate results (van Keken et al., 1997; Zhong and Hager, 2003). Even using models with adaptive mesh refinement to several km grid resolution, it is difficult to resolve entrainment rate for temperature-dependent viscosity (Leng and Zhong, 2011). Both laboratory and numerical experiments have been used to understand the mechanisms

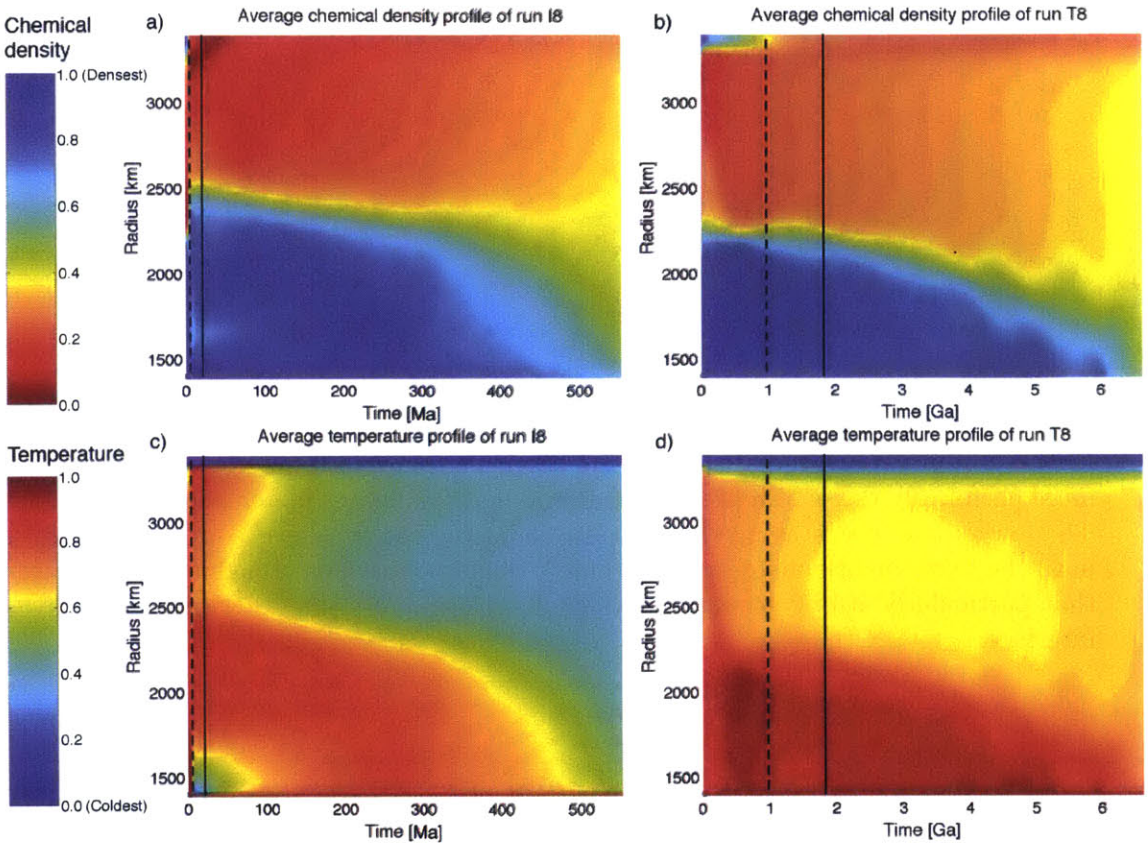

Figure 4-9: Horizontally averaged (a and b) chemical density and (c and d) temperature for two runs. The dashed vertical line marks the point at which the chemical density instability is 20% of its original size, while the solid line marks the point at which the instability is reduced to 2% its original size. The entrainment rate is poorly resolved in the numerical model and shown here for qualitative demonstration, although the timescale is fairly similar to that produced by scaling estimates.

and timescale with which a convecting upper layer entrains underlying denser material (Davaille, 1999; Gonnerman et al., 2002; Jellinek and Manga, 2002; Zhong and Hager, 2003). Using the compositional and thermal profiles of our isoviscous model immediately after overturn, we use an experimentally derived scaling law to estimate the timescale over which the lower dense layer would survive.

Davaille (1999) experimentally derived a scaling theory for entrainment rate, further corroborated by later laboratory work (Gonnerman et al., 2002), finding that

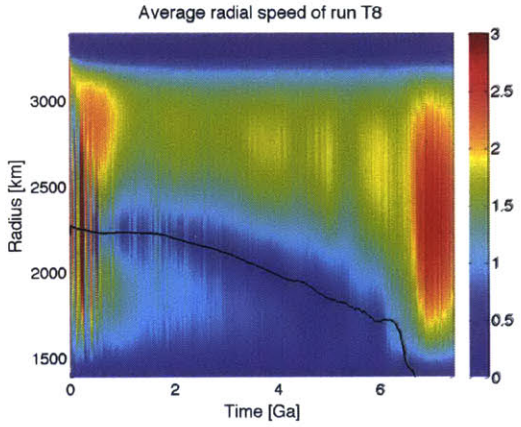

Figure 4-10: Average radial speed. The black line shows the interface between the more chemically dense lower mantle material and the lighter upper mantle material. The low radial speeds along the interface indicate that two-layer convection occurs until the lower mantle material is entrained. The brief periods of high speed indicate that particularly strong advective activity is able to cross the otherwise conductive interface.

$$q = 0.2\kappa d^{-1} B_D^{-2} Ra_d^{1/3} \frac{1}{1 + \gamma B_D^{-1}}, \tag{4.11}$$

where q is entrainment flux per unit area and viscosity contrast γ is the viscosity ratio between the two layers. The buoyancy ratio defined by Davaille (1999), B_D, includes the thermal buoyancy across the entire model, so equals $B\,C_e$ (Fig. 4-14). Ra_d is the Rayleigh number, with the subscript added to clarify that in this equation Rayleigh number is defined by mantle depth, not planetary radius. Applying this equation to our postoverturn profile, we estimate a lifetime of 500 Ma for an isoviscous ($\gamma = 1$) scenario, and 3.8 Ga for $\gamma = 10$. The entrainment timescales of our numerical models, albeit insufficiently resolved, were a similar magnitude.

4.4 Discussion

The absence of degree-one overturn pattern suggests that cumulate overturn may not play the hypothesized role of initiating a hemispherical core dynamo or contributing to the crustal dichotomy. We can understand the difficulty in creating a degree-one

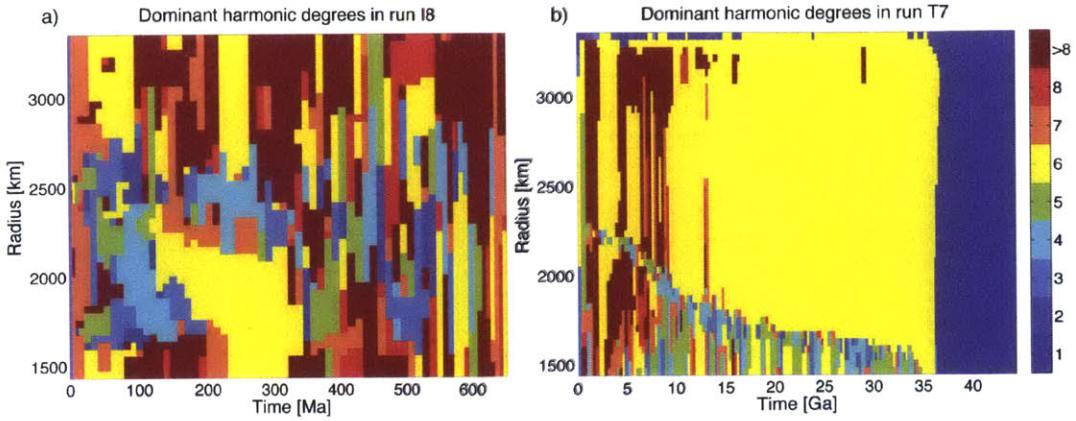

Figure 4-11: Most dominant harmonic degrees (in radial velocity) for (a) an isoviscous case (I8) and (b) a temperature- and pressure-dependent viscosity case (T7). Viscosity contrast resulted in degree-one convection but only after entrainment was complete.

pattern by closer consideration of the two-layer case. Long-wavelength instabilities occur more easily when viscosity contrast is high and when both layers are of a substantial thickness compared with total model thickness. Although these conditions can be easily reached in a two-layer system, any scenario in which viscosity and chemical density vary continuously and gradually with depth will not satisfy those requirements. Parmentier et al. (2002) found that for the Moon, degree-one overturn is possible when a large viscosity contrast occurs over a small depth range when a high-density layer is placed on a uniform density mantle. In our scenario however, the density instability was gradual across a large range. Because overturn initiates wherever buoyancy forces face the least resistance from viscosity, any large contrast in viscosity between two layers will, rather than increasing wavelength, force the overturn to occur at some other depth at which both the upper and lower layers are of relatively low viscosity. Additionally, the initially overturning layers will tend to be thin, since material surrounding the minimum in viscosity is by definition of higher viscosity, and therefore slower to join in the overturn. Thus, the initial overturn will always occur in a thin layer of a region with low viscosity contrast, and will always invert in a short-wavelength pattern.

Although degree-one overturn may be unlikely, previous work (Zhong and Zuber, 2001; Roberts and Zhong, 2006) has demonstrated the tendency toward degree-one

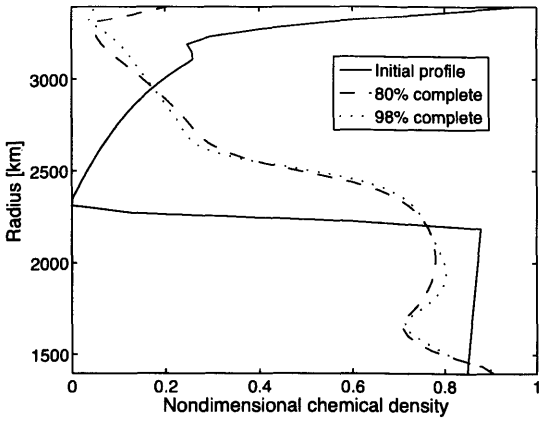

Figure 4-12: Profiles of the horizontally averaged nondimensionalized chemical density from an isoviscous model (I8) initially and after the density instability in the upper layer of the mantle is reduced by 80% and 98%. The lower mantle develops a chemical density instability that is resolved slowly as cold but chemically light material that has fallen to the lower mantle warms conductively and rises back into the upper mantle. This late lower mantle process is not included in our assessment of overturn timescales.

convection when a more realistic asthenosphere and lithosphere rheology is included. In this study, we found that subsequent single-cell convection was a consistent result after complete entrainment of the dense lower layer when viscosity varied with temperature, but the hemispherical dichotomy on Mars would have predated the completion of entrainment even using our shortest estimates of entrainment timescale. Ke and Solomatov (2009) suggest an independent mechanism for degree-one convection, a superplume originating from a thermal Rayleigh-Taylor instability at the core-mantle boundary, which could also potentially induce and sustain degree-one convection.

Rheological assumptions play a large role in determining the rate of overturn. While our temperature-dependent model had a viscosity contrast of around 1000:1, a higher contrast would extend the lifetime of a gravitationally unstable lithosphere, delaying mixing and permitting a relatively isolated chemical reservoir enriched in incompatible elements by fractional crystallization.

There are three end-member scenarios for the fate of the heavy-element-enriched layer resulting from late-stage fractional crystallization: that it was not able to over-

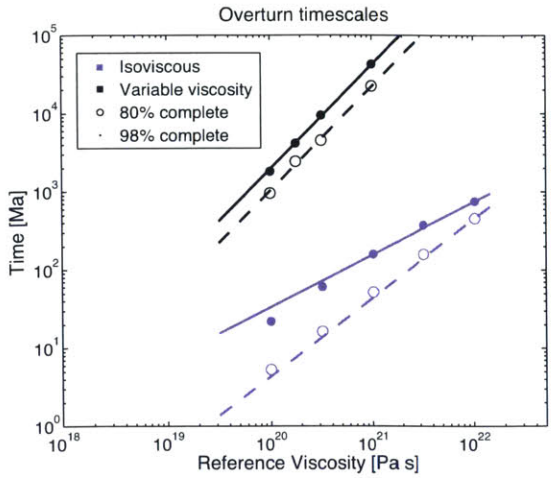

Figure 4-13: Overturn timescales. Advection in early planetary history was likely too rapid to be resolved by present models. We can extrapolate to higher Rayleigh numbers (lower viscosity) using the trends determined from high-viscosity calculations. For example, assuming a realistic viscosity profile lies between isoviscous (I) and variable viscosity (T) as bounds and assuming a reference viscosity of 10^{18} Pa s, overturn would have taken about 3-4 Ma.

turn at all; that overturn occurred and the stable density stratification was not overcome by convection; or that the whole mantle became well-mixed. However, gravity and moment of inertia observations do not support the possibility of an extant high-density stagnant lid (Pauer and Breuer, 2008; Sohl and Spohn, 1997).

Assuming overturn did occur, the lower layer could have been entrained significantly, creating isotopic heterogeneities throughout the mantle. Later melting events responsible for crustal formation would therefore have access to the full range of isotopic signatures formed during fractional solidification, accounting for the differences in isotopic signatures found between SNC meteorites. Mixing would bring small-scale reservoirs near the surface where that would be more readily possible.

The extent to which mixing has occurred is poorly constrained. Employing empirically derived scaling laws, we calculated the lifetime of a dense lower layer after overturn in an isoviscous mantle to be 500 Ma and 3.8 Ga if the upper mantle were ten times more viscous than the lower mantle. Since these results do not scale strongly with Rayleigh number, uncertainty in Ra should not affect them significantly. However, a stagnant lid and secular cooling across long timescales will slow later entrain-

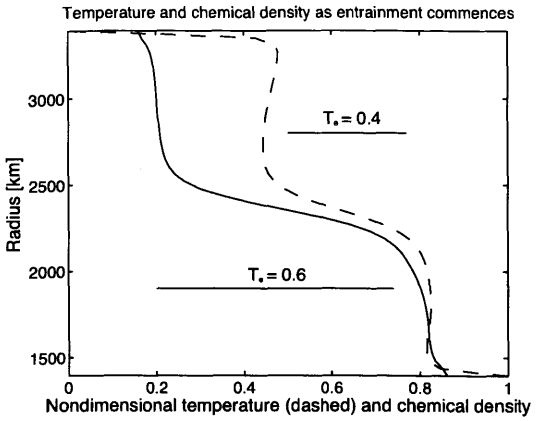

Figure 4-14: Horizontally averaged nondimensionalized chemical density and thermal profiles from an isoviscous model (I8). These profiles occur after overturn is complete and when thermal convection has homogenized the upper mantle enough to produce a well-defined two-layer system to which scaling arguments can be applied. The density and thermal contrasts in this figure are used to compute the buoyancy ratios used in our entrainment estimates.

ment and extend the lifetime of the dense lower layer significantly. Tosi et al. (2013) showed that for a Mars overturn scenario with an inverted linear density gradient, complete mixing by present day is unlikely.

The scaling properties evident in Figure 4-13 are of particular interest. In a Rayleigh-Taylor overturn process with no thermal processes, timescale is directly proportional to mantle viscosity μ_0. The $\mu_0^{2/3}$ and $\mu^{4/3}$ time scalings observed in isoviscous and temperature-dependent models, respectively, suggests that thermal mechanisms play a large role in opposing or reinforcing the gravitational instability.

Our results suggest in an isoviscous mantle, the bulk of overturn occurs quickly enough that thermal diffusion is not an important process for it, resulting in a μ_0^1 time scaling, while the remaining 20% takes several times longer (Fig. 4-13). However, the descent of the final 20% of the chemically dense upper layer will scale with $\mu_0^{2/3}$ since the surface material has time to become more negatively buoyant through conductive cooling. For lower viscosities, thermal diffusion should become less relevant, and the final 20% of overturn should occur with the same Rayleigh number dependence as the initial 80%.

In contrast, when viscosity is temperature dependent, thermal diffusion slows

Morphology calculations				
Name	Ra	E'	Degree of overturn	
I8	$2.3 \cdot 10^8$	0	6	
E2	$2.3 \cdot 10^8$	2	8	
E3	$2.3 \cdot 10^8$	3	8	
E4	$2.3 \cdot 10^8$	4	10	
T8	$2.3 \cdot 10^8$	5	8	
Timescale calculations				
Name	Ra	E'	Time at 80% overturn completion (Ma)	98% completion (Ma)
I8	$2.3 \cdot 10^8$	0	5.38	22.2
I7.5	$2.3 \cdot 10^{7.5}$	0	16.5	61.5
I7	$2.3 \cdot 10^7$	0	51.9	159
I6.5	$2.3 \cdot 10^{6.5}$	0	156	369
I6	$2.3 \cdot 10^6$	0	443	733
T8	$2.3 \cdot 10^8$	5	960	1820
T7.75	$2.3 \cdot 10^{7.75}$	5	2440	4160
T7.5	$2.3 \cdot 10^{7.5}$	5	4520	9450
T7	$2.3 \cdot 10^7$	5	22400	42700

Table 4.2: Mars model results

down the overturn process rather than accelerating it. If the reference viscosity is raised, the upper layer has more time to cool conductively before advection of the unstable material occurs. This increased cooling raises the local viscosity (Fig. 4-15), slowing advection further. A theoretical derivation of this $\mu_0^{4/3}$ scaling is needed but beyond the scope of this study. We expect that for high Rayleigh numbers, diffusion will again no longer play a significant role, resulting in a μ_0^1 timescale. However, for Rayleigh numbers that we were able to resolve, we did not reach this regime.

Surface temperature and core temperature were constant in our model. In reality, both these variables decrease with time, so that this assumption, although valid for timescales on the order of 100 Ma, may be less valid with larger timescales. Cooling will increase viscosity with time, while a decrease in the temperature contrast across the mantle will reduce thermal buoyancy. Thus if thermal convection is unable to overcome a chemical density profile early on, complete entrainment might not be possible.

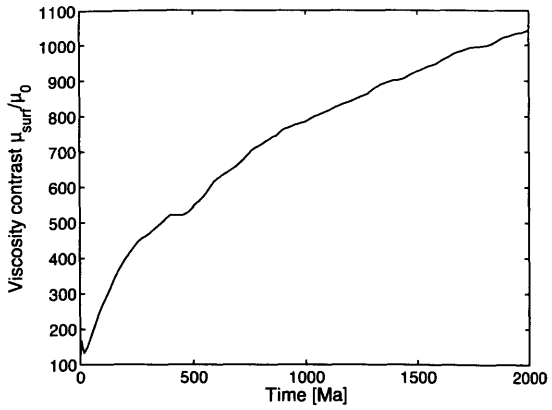

Figure 4-15: The ratio of viscosity in the uppermost element of the model to reference viscosity for the temperature-dependent viscosity model T8 with reference viscosity $\mu_0 = 10^{20}$ Pa s. As the lithosphere cools conductively, viscosity in the surface elements increases. The larger the reference viscosity, the more pronounced the effect of this viscosity increase on overturn timescales, producing timescales proportional to $\mu_0^{4/3}$.

4.5 Conclusion

We present four broad conclusions:

- The harmonic degree of overturn varies between 6 and 10 for the cases examined here that assume a sluggish rather than stagnant lid. We therefore conclude that degree-one overturn is unlikely to have resulted from magma ocean fractional crystallization in Mars or other planets with the characteristics explored here.

- An initial overturn event could create an added core heat flux in excess of tens of mW during the period of stability prior to the onset of thermal convection.

- For an isoviscous mantle with $\mu_o = 10^{20}$ Pa s, a dense lower layer produced by fractional crystallization and subsequent overturn would persist on the order of 500 Ma. A viscosity contrast of 10 between the lower and upper mantle would increase this lifetime to 3.8 Ga. Secular cooling and a stagnant lid will extend timescales further. Complete mixing of chemically homogenous has therefore likely not occurred, but there would have been sufficient entrainment to permit smaller-scale domains of isotopically distinct material to participate in melting

and crustal formation.

- Thermal processes strongly impact the Rayleigh-Taylor problem in most scenarios. Overturn timescales in models assuming constant viscosity scale with μ_0^1 for the bulk of overturn but $\mu_0^{2/3}$ for the remainder. Overturn times scale as $\mu_0^{4/3}$ when using a temperature- and pressure-dependent rheology. Provided the range of rheologies examined here and given $\mu_o = 10^{19}$ Pa s, 98% of overturn would have taken 7-90 Ma. For $\mu_o = 10^{18}$ Pa s, the process would have required about 2-4 Ma.

Acknowledgements

Thanks to coauthors L.T. Elkins-Tanton and S. Zhong, and to our anonymous reviewers.

Chapter 5

Conclusion

The ease with which self-sustaining magnetic fields are produced within planets, small bodies, and stars has become apparent as direct observation and paleomagnetic evidence has amassed. However, explaining the morphology, duration, and magnitude of these magnetic fields is an open challenge.

Some planetesimals are known to have differentiated and formed a metallic core. The high heat flux from such small bodies would have been capable of driving a core dynamo, and such fields have been recorded in a number of meteoritic samples. However, the impact of core solidification on the internally produced magnetic field of these bodies has not been explored.

In this dissertation, two core solidification scenarios were examined and the energy available to power a dynamo was estimated. In one scenario, the core solidifies inward in dendritic growth patterns. In the second scenario, crystals forming in the liquid settle to form a cumulate inner core. In either scenario, it appears that three factors work together to make dynamo action more difficult during solidification than during super-solidus cooling. First, the shrinking of the convective region as the core solidifies necessarily reduces the length-scale of the problem, which affects the power available to a dynamo as well as the threshold in convective vigor that must be reached to ensure a magnetic field reinforces itself rather than diffusing away. Second, the necessity of re-entraining light elements reduces the ability of thermal heat flux to otherwise drive a dynamo. This effect is more than compensated for if the settling of solid iron crystals

also occurs, as in the 'cumulate inner core' scenario. Finally, in either scenario, the latent heat of fusion released near the core-mantle boundary during solidification produces a thermal buffer the reduces heat flux out of the underlying liquid, further reducing the strength of convection and its capacity to drive a dynamo field.

We also examined the difficulty of explaining the scientific community's empirical understanding of the lunar magnetic field in terms of a coherent core evolution model. Paleomagnetic observations indicate a surface magnetic field of approximately 70 μT between 4.2 and 3.56 billion years ago. Paleomagnetic evidence beyond this "high field" epoch is more ambiguous, but it appears a "weak field" epoch continued until less than two hundred million years before present day. This secondary epoch had fields as high as 4 μT, but those measurements are also consistent with a zero field. Purely thermal dynamo modeling has been unable to account for the either the strength or longevity of the field. Previous studies have suggested that tidal forces or precession could supply sufficient energy to explain the large magnitude during the high field epoch, but not the late field's duration.

The present work hypothesized that thermochemical core convection, which had not been thoroughly investigated in the Moon in prior literature, could explain some or all aspects of the field's magnitude and duration during one or both of these epochs. We modeled heat flow from the lunar core under a wide variety of mantle conditions and determined the energy available to power a dynamo in each scenario. Under no circumstances was our core dynamo scaling model able to produce a magnitude matching that of the recorded lunar field. Rather than 70 μT, we obtained maximum fields of $\sim$1 μT.

Two indicators are typically used in modeling to evaluate the longevity of a dynamo-powered field. First a dynamo will shut down if the magnetic Reynolds number falls below its critical value. Second, a dynamo will shut down if there is no power thermodynamically available to drive a dynamo. In our analysis of planetesimals, where length-scales are small, this first requirement was the limiting condition on dynamo duration. However, in the lunar case the second condition was critical. This difference occurs partly because total power is determined by summing thermal

and compositional energy sources and subtracting the adiabatic heat flux. In a small body with little insulation, adiabatic heat flux is a trivially small component of total heat flux. In the lunar scenario, on the other hand, adiabatic heat flux is the same order of magnitude as total heat flux for most of lunar history.

In our models, this similar order of magnitude rendered the existence and stability of a late-stage lunar magnetic field very sensitive to assumptions made about material parameters that determine adiabatic heat flux. While typically used parameters yielded a field that shut down after the "high field" epoch, we found that using values in the low range for the thermal expansion coefficient and the thermal conductivity value yielded a field lasting until or near present day. Although this field was substantially smaller than the estimated 4 μT of the "weak field" epoch, the thermochemical dynamo model reproduced the transition from high to low field reasonably well. Perhaps most interestingly, some ranges of adiabatic heat flux yielded a "start-stop" regime in which the field was deactivated temporarily and then reactivated due to irregularities in heat flow. If the dynamo were currently in such a regime, it could explain why there appears to be evidence for a recent field despite no active dynamo today.

The final component of this thesis focused on the early history of the Martian mantle, with attention, as with the lunar study, to the impact that mantle dynamics had on core heat flow and the resulting dynamo. Using estimates of the density profile expected to occur as a result of fractional magma ocean solidification, we examined the timescale and morphology of the collapse of the gravitationally unstable early mantle. We hypothesized that features of the Martian dichotomy could be explained by a degree-one overturn event that left dense, initially cold silicate material stably stratified at the core-mantle boundary. In particular, we proposed that the dichotomy in observed crustal magnetization between the strongly magnetized southern hemisphere and the weakly magnetized northern hemisphere could be explained by a degree-one pattern in core heat flow following mantle overturn. Such a heat flow had been shown in previous dynamo models to result in a hemispherical dynamo wherein magnetic field strength would be highly asymmetric across the equator.

Based on modeling results and theoretical discussion, we concluded that large-wavelength (i.e. degree-one) overturn is unlikely in a system where viscosity and density vary gradually with depth. Large-wavelength instabilities are likely when the unstable layer is thick and has a high viscosity contrast with the underlying low-density layer. However, the predicted density profile of a fractionally crystallized magma ocean is more gradual. Any particular unstable layer would be thin and show little viscosity contrast with neighboring layers. This arrangement encourages short- rather than long-wavelength instabilities to be the dominant morphology of overturn. For the density profile assumed in this study, we therefore determined that mantle overturn as a hypothesized mechanism to explain the hemispherical dichotomy, and in particular the magnetic field dichotomy, was not supported. However, we also noted that overturn timescales, though dependent on poorly constrained parameters and in particular viscosity, could have proceeded as quickly as three million years. Our work therefore does not preclude the later occurrence of a degree-one convection pattern which would still have time to account for the hemispherical dichotomy.

5.1 Future Work

Modeling work in a field as expansive as planetary science - particularly of subjects where direct observation is expensive, difficult and rare - is inherently open-ended. This dissertation has lain the groundwork for future investigation into planetesimal solidification-driven dynamos, and also investigated and weighed in on certain scenarios of the thermochemical lunar dynamo hypothesis and the Martian hemispherical dynamo hypothesis. Future models should continue to explore the wide potential parameter space in search of an explanation for observations of meteorites, the Moon, and Mars. Future laboratory and exploratory work can be done to constrain and refine inputs to these models.

Regarding the solidification, structure, and remanent magnetic field of asteroidal cores, there are many future avenues of exploration. This study relies on a crude one-dimensional model with parameterized convection. Future work could seek to

more accurately understand the nature of convection, the three-dimensional structure of dendritic growth, and their interplay. Future modeling of planetesimal core solidification could also explore the effect of a more complicated chemical composition. The introduction of phosphorous, for example, could result in immiscible and thus chemically isolated convection zones. The stability of dendrites could be better understood by extending beyond the basic Rayleigh-Taylor instability estimate presented here. The expected effect on trace element fractionation of these processes and those described in this dissertation should be explored and compared with meteoritic evidence. The process and resulting features of thermal contraction as a planetesimal cools could be examined in order to make predictions about the structure of M-type asteroids. Experimental work into dendritic growth in a system approximating metal meteoritic composition and material strength could refine models. Finally, further exploration in the Asteroid Belt will provide us a wealth of information on the true nature and variety of core processes.

Although there are candidate explanations for the "high-field" epoch of the lunar dynamo, there is still no explanation for the potential "low-field" epoch and no overarching framework to explain the evolution of the lunar field through its history. Promising future work could investigate the possibility of a basal magma ocean in the lunar context. As noted in Chapter 3, a high density contrast in the mantle due to the overturn of a fractionally crystalized magma ocean could result in a relatively immobile lower mantle with a high concentration of incompatible radiogenic elements. This lower mantle would likely melt. Such a scenario was ignored in this work since our mantle model was not prepared to correctly predict behavior of a molten region. However, due to its high density, the melt would likely remain in situ as a convecting liquid layer until radiogenic heating fell sufficiently, and sufficient cooling occurred. The layer would also contain a high concentration of alkalines that raise electrical conductivity. It is therefore plausible that a liquid lower mantle could itself drive a dynamo field. Due to the significantly larger length-scales and proximity to the surface, such a dynamo may be able to reproduce the large magnetic field magnitudes observed during the high-field epoch. Furthermore, such a scenario would inhibit heat

flow from the core during that epoch, potentially delaying and extending core cooling and solidification across later lunar history. A core dynamo could then be responsible for the later weak field. This unified explanation would be an elegant solution to the lunar magnetic field problem, and should be explored.

Finally, more modeling should investigate the means by which a dynamo field could explain the observed crustal magnetization on Mars. While the idea of an exogenous formation mechanism for the crustal dichotomy (i.e., a giant impact in the northern hemisphere) has gained credibility, it is not clear this can explain the magnetization dichotomy. On the other hand, we demonstrated than an upper mantle Rayleigh-Taylor instability alone may not be able to produce a core heat flux pattern necessary for a hemispherical dynamo. Future work could examine the potential for a giant impact - effectively a degree-one forcing - to kick-start long-wavelength mantle activity.

Bibliography

Acuña, M.H., et al., 2002. NEAR magnetic field observations at 433 Eros: First measurements from the surface of an asteroid. Icarus 155, 220-228.

Anderson, W.W., Ahrens, T.J., 1994. An equation of state for liquid iron and implications for the Earth's core. J. Geophys. Res., Solid Earth 99, 4273-4284.

Anderson, O.L, 1998. The Grüneisen parameter for iron at outer core conditions and the resulting conductive heat and power in the core. Phys. Earth Planet. Inter. 109, 179-197.

Andrews-Hanna, J.C., Zuber, M.T., Banerdt, W.B., 2008. The Borealis basin and the origin of the Martian crustal dichotomy. Nature 453, 1212-1215.

Alfe, D., Gillan, M.J., 1998. First-principles simulations of liquid Fe-S under Earth's core conditions. Physical Review B 58, 8248-8256.

Arzi, A.A., 1978. Critical phenomena in the rheology of partially melted rocks. Tectonophysics 44, 173-184.

Assael, M.J., et al., 2006. Reference data for the density and viscosity of liquid aluminum and iron. J. Phys. Chem. Ref. Data 35, 285-300.

Blanco-Cano, X., Omidi, N., Russell, C.T., 2003. Hybrid simulations of solar wind interaction with magnetized asteroids: Comparison with Galileo observations near Gaspra and Ida. J. Geophys. Res. 108, 1216.

Bland, P.A., et al., 2014. Pressure-temperature evolution of primordial solar system solids during impact-induced compaction. Nature Commun. 5, 5451.

Borg, L.E., Nyquist, L.E., Taylor, L.A., Wiesmann, H., and Shih, C.-Y., 1997. Constraints on Martian differentiation processes from Rb-Sr and Sm-Nd isotopic analyses of the basaltic shergottite QUE 94201. Geochim. Cosmochim. Acta 61, 49154931

Braginsky, S.I., Roberts, P.H., 1995. Equations governing convection in Earth's core and the geodynamo. Geophys. Astrophys. Fluid Dynamics 79, 1-97.

Brearley, A.J., Krot, A.N., 2012. Metasomatism in the early solar system: The record from chondritic meteorites. In Metasomatism and the Chemical Transformation of Rock (Harlov D. E. and Austrheim H., eds.), pp. 659-789. Springer-Verlag, Berlin.

Bryson, J., et al., 2015. Long-lived magnetism from solidification-driven convection on the pallasite parent body. Nature 517, 472-475.

Buchwald, V.F., 1971. The Cape York shower, a typical group IIIA iron meteorite, formed by directional solidification in a gravity field. Meteoritics 6, 252-253.

Buchwald, V.F., 1975. Handbook of Iron Meteorites, 2. Univ. of California, Berkeley.

Buffett, B. A., Huppert, H.E., Lister, J.R., Woods, A. W., 1996. On the thermal evolution of the Earth's core. J. Geophys. Res. 101, 7989-8006.

Buffett, B.A., 2002. Estimates of heat flow in the deep mantle based on the power requirements for the geodynamo. Geophys. Res. Lett. 29, 1566.

Bullard, E.C., Gellman, H., 1954. Homogeneous dynamos and terrestrial magnetism. Philosoph. Trans. Royal Soc. London A 247, 213-278.

Burke, B.F., Franklin, K.L., 1955. Observations of a variable radio source associated with the planet Jupiter. J. Geophys. Res. 60, 213-217.

Canup, R.M., Asphaug, E., 2001. Origin of the Moon in a giant impact near the end of the Earth's formation. Nature 412, 708-712.

Carporzen, L., et al., 2011. Magnetic evidence for a partially differentiated carbonaceous chondrite parent body. Proc. Natl Acad. Sci. 108, 6386-6389.

Cebron, D., Hollerbach, R., 2014. Tidally driven dynamos in a rotating sphere. Astrophys. J. 789, L25:1-5

Cebron, D., et al., 2014. Dynamo driven by inertial instabilities, application to the Moon. AGU abstract, GP54A-03.

Chabot, N.L., Campbell, A.J., Jones, J.H., Humayun, M., Agee, C.B., 2003. An experimental test of Henry's Law in solid metal-liquid metal systems with implications for iron meteorites. Met. and Planet. Sci. 38, 181-196.

Chabot, N.L., Jones, J.H., 2003. The parameterization of solid metal-liquid metal partitioning of siderophile elements. Met. and Planet. Sci. 38, 1425-1436.

Chabot, N.L., 2004. Sulfur contents of the parental metallic cores of magmatic iron meteorites. Geochim. Cosmochim. Acta 68, 3607-3618.

Chabot, N.L. Haack, H., 2006. Evolution of asteroidal cores. In: Lauretta, D.S., McSween, H.Y. (Eds.), Meteorites and the Early Solar System II. University of Arizona Press, Tucson, 747-771.

Chan, K.H., Zhang, K., Li, L., Liao, X., 2007. A new generation of convection-driven spherical dynamos using EBE finite element method. Phys. Earth Planet. Inter. 163, 1-4.

Christensen, U.R., 1984. Convection with pressure- and temperature- dependent non-Newtonian rheology. Geophys. J. R. Astr. Soc. 77, 343-384.

Christensen, U.R., Yuen, D.A., 1985. Layered convection induced by phase transitions. J. Geophys. Res. 90, 291-300.

Christensen, U.R., Olson, P., Glatzmaier G., 1999. Numerical modeling of the geodynamo: A systematic parameter study. Geophys. J. International 138, 393-409.

Christensen, U.R., Aubert, J., 2006. Scaling properties of convection-driven dynamos in rotating spherical shells and application to planetary magnetic fields. Geophys. J. Int. 166, 97-114.

Christensen, U.R., Wicht, J., 2007. Numerical dynamo simulations. In: Olson, P.L. (Ed.), Treatise on Geophysics, vol. 8. Elsevier, pp. 245-282

Christensen, U.R., 2010. Dynamo scaling laws and applications to the planets. Space Sci. Rev. 152, 565-590.

Christensen, U.R., 2015. Iron snow dynamo models for Ganymede. Icarus 247, 248-259.

Connerney, J.E.P., et al., 2005. Tectonic implications of Mars crustal magnetism. Proceedings of the National Academy of Sciences 102(42), 14970-14975.

Connerney, J.E.P., 2007. Planetary magnetism. In: Spohn, T. (Ed.), Treatise on Geophysics, vol. 10. Elsevier, pp. 243-280.

Conrad, C.P., Molnar, P., 1996. The growth of Rayleigh-Taylor-type instabilities in the lithosphere for various rheological and density structures. Geophys. J. Int. 129, 95-112.

Conzelmann, V., 1994. Die thermische Evolution des Mondes und sein Magnetfeld. Diploma thesis, Institut fur planetologie, Munster.

Costa, V.A.F., 2002. A time scale-based analysis of the laminar convective phenomena. Int. J. Therm. Sci 41, 1131-1140.

Cournede, C., et al., 2015. An early solar system magnetic field recorded in CM chondrites. Earth Planet. Sci. Lett. 410, 62-74.

Cowling, T.G., 1934. The magnetic field of sunspots. Monthly Notices R. Astron. Soc. 34, 39-48.

Crutcher, R.M., 2012. Magnetic fields in molecular clouds. Annu. Rev. Astron. Astrophys. 50, 29-63.

Davaille, A., 1999. Simultaneous generation of hotspots and superswells by convection in a heterogeneous planetary mantle. Nature 402, 756-760.

de Koker, N., Steinle-Neumann, G., Vlček, V., 2012. Electrical resistivity and thermal conductivity of liquid Fe alloys at high P and T, and heat flux in Earth's core. Proc. Natl Acad. Sci. 109, 4070-4073.

de Pater, I., Lissauer, J.J., 2015. Planetary Sciences. Cambridge University Press, Cambridge.

Debaille, V., Yin, Q.Z., Brandon, A.D., Jacobsen, B., 2008. Martian mantle mineralogy investigated by the 176Lu-176Hf and 147Sm-143Nd systematics of shergottites. Earth Planet. Sci. Lett. 269, 186-199.

Desai, P.D., 1986. Thermodynamic properties of iron and silicon. J. Phys. Chem. Ref. Data 15, 967-983.

Dobson, D.P., et al., 2000. In situ measurement of viscosity of liquids in the Fe-FeS system at high pressures and temperatures. American Mineralogist 85, 1838-1842.

Dwyer, C.A., Stevenson, D.J., Nimmo, F., 2011. A long-lived lunar dynamo driven by continuous mechanical stirring. Nature 479, 212-214.

Elkins-Tanton, L.T., Parmentier, E.M., Hess, P.C., 2003. Magma ocean fractional crystallization and cumulate overturn in terrestrial planets: Implications for Mars. Meteorol. Planet. Sci. 38, 1753-1771.

Elkins-Tanton, L.T., Zaranek, S.E., Parmentier, E.M., Hess, P.C., 2005. Early magnetic field and magmatic activity on Mars from magma ocean cumulate overturn. Earth Planet. Sci. Lett. 236, 1-12.

Elkins-Tanton, L.T., 2008. Linked magma ocean solidification and atmospheric growth for Earth and Mars. Earth Planet. Sci. Lett. 271, 181-191.

Elkins-Tanton, L.T., Weiss, B.P., Zuber M.T., 2011. Chondrites as samples of differentiated planetesimals. Earth Planet. Sci. Lett. 305, 1-10.

Elkins-Tanton, L.T., Burgess, S., Yin, Q.-Z., 2011. The lunar magma ocean: Reconciling the solidification process with lunar petrology and geochronology. Earth and Plan. Sci. Lett. 304, 326-336.

Evans, A. J., Zuber, M. T., Weiss, B. P., Tikoo, S. M., 2014. A wet, heterogeneous lunar interior: Lower mantle and core dynamo evolution. J. Geophys. Res. 119, 1061-1077.

Fei, Y., Prewitt, C. T., Mao, H.-K., Bertka, C., 1995. Structure and density of FeS at high pressure and high temperature and the internal structure of Mars. Science 268, 1892-1894.

Fu, R.R., et al., 2012. An ancient core dynamo in asteroid Vesta. Science 338, 238-241.

Fu, R.R., Weiss, B.P., 2012. Detrital remanent magnetization in the solar nebula. J. Geophys. Res. 117, E02003.

Fu, R.R., et al., 2014. Solar nebula magnetic fields recorded in the Semarkona meteorite. Science 346, 1089-1092.

Fuller, M., Cisowski, S. M., 1987. Lunar paleomagnetism. In: Jacobs, J. A. (Ed.), Geomagnetism 2. Academic Press, Orlando, pp. 307-455.

Fulton, C.H., 1910. Principles of metallurgy: an introduction to the metallurgy of the metals. Plimpton Press, Norwood.

Garcia, R.F., Gagnepain-Beyneix, J., Chevrot, S., Lognonné, P., 2011. Very preliminary reference Moon model. Phys. Earth Planet. Inter. 188, 96-113.

Garcia, R.F., Gagnepain-Beyneix, J., Chevrot, S., Lognonné, P., 2012. Erratum to "Very preliminary reference Moon model". Phys. Earth Planet. Inter. 202-203, 89-91.

Glatzmaier, G.A., Roberts, P.H., 1995. A three-dimensional convective dynamo solution with rotating and finitely conducting inner core and mantle. Phys. Earth Planet. Inter. 91, 63-75.

Gonnermann, H.M., Manga, M., Jellinek, A.M., 2002. Dynamics and longevity of an initially stratified mantle. Geophys. Res. Lett. 29, doi:10.1029/2002GL014851

Green, D.H., Ware, N.G., Hibberson, A., Major, A., 1971. Experimental petrology of Apollo 12 mare basalts, Part 1, sample 12009. Earth and Plan. Sci. Lett. 13, 85-96.

Grott, M., Knollenberg, J., Krause, C., 2010. Apollo lunar heat flow experiment revisited: A critical reassessment of the in situ thermal conductivity determination, J. Geophys. Res. 115, E11005.

Haack, H., Scott, E.R.D., 1992. Asteroid core crystallization by inward dendritic growth. J. Geophys. Res. 97, 14727-14734.

Haq, B.U., et al., 1990. Proc ODP Init. Repts. 122, College Station, TX (Ocean Drilling Program).

Hauck, S.A., Aurnou, J.M., Dombard, A., 2006. Sulfur's impact on core evolution and magnetic field generation on Ganymede. J. Geophys. Res. 111, E09008.

Hess, P.C., Parmentier, E.M., 1995. A model for the thermal and chemical evolution of the Moon's interior: implications for the onset of mare volcanism. Earth Planet. Sci. Lett. 134, 501-514.

Hiesinger, H., Head III, J.W., Wolf, U., Jaumann, R., Neukum, G., 2003. Ages and stratigraphy of mare basalts in Oceanus Procellarum, Mare Nubium, Mare Cognitum, and Mare Insularum. J. Geophys. Res. 108(E7), 5065.

Hirth, G., Kohlstedt, D.L., 1996. Water in the oceanic upper mantle: implications for rheology, melt extraction and the evolution of the lithosphere. Earth Planet. Sci. Lett. 144, 93-108.

Hirth, G., Kohlstedt, D.L., 2003. Rheology of the upper mantle and the mantle wedge: A view from the experimentalists. Inside the subduction factory. Geophysical Monograph 138, 83-105.

Hixson, R.S., Winkler, M.A., Hodgdon, M.L., 1990. Sound speed and thermophysical properties of liquid iron and nickel. Phys. Rev. B 42, 6485-6491.

Jellinek, A.M., Manga, M., 2002. The influence of a chemical boundary layer on the fixity, spacing and lifetime of mantle plumes. Nature 41, 760-763.

Jing, Z., et al., 2014. Sound velocity of Fe-S liquids at high pressure: Implications for the Moon's molten outer core. Earth Planet. Sci. Let. 396, 78-87.

Jones, J.H., 1986. A discussion of isotopic systematics and mineral zoning in the shergottites: Evidence for a 180 Myr igneous crystallization age. Geochim. et Cosmochim. Acta 50, 969-977.

Karato, S.-I., Wu, P., 1993. Rheology of the upper mantle: A synthesis. Science 260, 771-778.

Karato, S-I., 2013. Geophysical constraints on the water content of the lunar mantle and its implications for the origin of the Moon. Earth and Plan. Sci. Lett. 384, 144-153.

Ke, Y., Solomatov, V.S., 2006. Early transient super plumes and the origin of the Martian crustal dichotomy. J. Geophys. Res. 111, E10001, doi:10.1029/2005JE002631.

Ke, Y., Solomatov, V.S., 2009. Coupled core-mantle thermal evolution of early Mars. J. Geophys. Res. 114, E07004, doi:10.1029/2008JE003291.

Khan, A., Pommier, A., Neumann, G. A., Mosegaard, K., 2013. The lunar moho and the internal structure of the Moon: A geophysical perspective. Tectonophysics 609, 331-352.

Kivelson, M.G., et al., 1995. Solar wind interaction with small bodies. 2. What can Galileo's detection of magnetic rotations tell us about Gaspra and Ida. Adv. Space Res. 16, 47-57.

Konrad, W., Spohn, T., 1997. Thermal history of the Moon - Implications for an early core dynamo and post-accretional magmatism. Adv. Space Res. 19, 1511-1521.

Labrosse, S., Poirier, J.-P., Le Mouël, J.-L., 2001. The age of the inner core. Earth and Plan. Sci. Lett. 190, 111-123.

Labrosse, S., 2003. Thermal and magnetic evolution of the Earth's core. Phys. Earth Planet. Inter. 140, 127-143.

Laneuville, M., Wieczorek, M. A., Breuer, D., Tosi, N., 2013. Asymmetric thermal evolution of the Moon. J. Geophys. Res. Planets 118, 1435-1452.

Laneuville, M. et al., 2014. A long-lived lunar dynamo powered by core crystallization. Earth and Planet. Sci. Lett. 401, 251-260.

Langseth, M. G., Keihm, S. J., Peters, K., 1976. Revised lunar heat-flow values. Proc. Lunar Sci. Conf., 7th, 3143-3171.

Le Bars, M., Wieczorek, M. A., Karatekin, O., Cebron, D., Laneuville, M., 2011. An impact-driven dynamo for the early Moon. Nature 479, 215-218.

Leng, W., Zhong, S., 2011. Implementation and application of adaptive mesh refinement for thermochemical mantle convection studies. Geochem. Geophys. Geosyst. 12, Q04006, doi:10.1029/2010GC003425.

Lister, J. R., Buffett, B. A., 1995. The strength and efficiency of thermal and compositional convection in the geodynamo. Phys. Earth Planet. Inter. 91 17-30.

Lister, J. R., 2003. Expressions for the dissipation driven by convection in the Earth's core. Phys. Earth Planet. Inter. 140, 145-158.

Marsh, B.D., 1995. Solidification fronts and magmatic evolution. Mineral. Mag. 60, 5-40.

Martin, D., Nokes, R., 1989. A fluid-dynamic study of crystal settling in convecting magmas. J. Petrol. 30, 1471-1500.

McKenzie, D., 2011. Compaction and crystallization in magma chambers: towards a model of the Skaergaard intrusion. J. Petrol. 52, 905-930.

Meyer, J., Elkins-Tanton, L. T., Wisdom, J., 2010. Coupled thermal-orbital evolution of the early Moon. Icarus 208, 1-10.

Mitchell, D. S., Halekas, J. S., Lin, R. P., Frey, S., Hood, L. L., Acuna, M. H., Binder, A., 2008. Global mapping of lunar crustal magnetic fields by Lunar Prospector. Icarus 194, 401-409.

Monteux, J., Jellinek, A.M., Johnson, C.L., 2011. Why might planets and moons have early dynamos? Earth Planet. Sci. Let. 310, 349-359.

Moskovitz, N.A., Walker, R.J., 2011. Size of the group IVA iron meteorite core: constraints from the age and composition of Muonionalusta. Earth Planet. Sci. Lett. 308, 410-416.

Murthy, V. R., Hall, H. T., 1970. The chemical composition of the Earth's core: Possibility of sulphur in the core. Phys. Earth Planet. Inter. 2, 276-282.

Nasch, P.M., Steinemann, S.G., 1995. Density and thermal expansion of molten manganese, iron, nickel, copper, aluminum and tin by means of the gamma-ray attenuation technique. Phys. Chem. Liq. 29, 43-58.

Nimmo, F., 2007. Thermal and compositional evolution of the core. Treatise on Geophysics, vol. 8. Elsevier, Amsterdam.

Nimmo, F., 2009. Energetics of asteroid dynamos and the role of compositional convection. Geophys. Res. Lett. 36, L10201.

Nishida, K., Terasaki, H., Ohtani, E., Suzuki, A., 2008. The effect of sulfur content on density of the liquid Fe-S at high pressure. Phys. Chem. Miner. 35, 417-423.

Olson, P., Christensen, U.R., 2006. Dipole moment scaling for convection-driven planetary dynamos. Earth Planet. Sci. Lett. 250, 561-571.

Parmentier, E.M., Zhong, S., Zuber, M.T., 2002. Gravitational differentiation due to initial chemical stratification: Origin of lunar asymmetry by the creep of dense KREEP. Earth Planet. Sci. Lett. 201, 473-480.

Pauer, M., Breuer, D., 2008. Constraints on the maximum crustal density from gravity topography modeling: Applications to the southern highlands of Mars. Earth Planet. Sci. Lett. 276, 253-261.

Rasmussen, J. L., Warren, P. H., 1985. Megaregolith thickness, heat flow, and the bulk composition of the Moon. Nature 313, 121-124.

Richter I., et al., 2001. First direct magnetic field measurements of an asteroidal magnetic field: DS1 at Braille. Geophys. Res. Lett. 28, 1913-1916.

Richter, I., et al., 2012. Magnetic field measurements during the Rosetta flyby at asteroid (21)Lutetia. Planet. Space Sci. 66, 155-164.

Righter, K., Hervig, R.J., Kring, D.A., 1998. Accretion and core formation on Mars: Molybdenum contents of melt inclusion glasses in three SNC meteorites. Geochim. et Cosmochim. Acta 62, 2167-2177.

Roberts, J.H., Zhong, S., 2006. Degree-1 convection in the Martian mantle and the origin of the hemispheric dichotomy. J. Geophys. Res. 111, E06013, doi:10.1029/2005JE002668.

Roberts, P.H., 2007. Theory of the geodynamo. In: Olson, P.L. (Ed.), Treatise on Geophysics, vol. 8. Elsevier, pp. 67-105.

Roberts, P. H., Aurnou, J. M., 2012. On the theory of core-mantle coupling. Geophys. Astrophys. Fluid Dynamics 106, 157-230.

Riner, M. A., Bina, C. R., Robinson, M. S., Desch, S. J., 2008. Internal structure of Mercury: implications of a molten core. J. Geophys. Res.113, E08013.

Runcorn, S.K., 1975a. An ancient lunar magnetic dipole field. Nature 253, 701-703

Runcorn, S.K., 1975b. On the interpretation of lunar magnetism. Phys. Earth. Planet. Inter. 10, 327-335.

Russell, C.T., 1993. Planetary Magnetospheres. Reports on Progress in Physics, 56, 687-732.

Ryder, G., 1982. Lunar anorthosite 60025, the petrogenesis of lunar anorthosites, and the bulk composition of the Moon. Geochimica et Cosmochimica Acta 46, 1591-1601.

Scheinberg, A., Elkins-Tanton, L.T., Zhong, S.J., 2014. Timescale and morphology of Martian mantle overturn immediately following magma ocean solidification. J. Geophys. Res. Planets 119, 454-467.

Scheinberg, A., Fu, R.R., Elkins-Tanton, L.T., Weiss, B.P., 2015. Asteroid differentiation: Melting and large-scale structure. In: Michel, P., DeMeo, F.E., Bottke W., (Eds.), Asteroids IV, in press. University of Arizona Press, Tucson.

A. Scheinberg, K. Soderlund, G. Schubert. Magnetic field generation in the lunar core: The role of inner core growth. Icarus, in press.

Shea, E.K., et al., 2012. A long-lived lunar core dynamo. Science 335, 453-456.

Sohl, F., Spohn, T., 1997. The interior structure of Mars: Implications from SNC meteorites. J. Geophys. Res. 102(E1), 1613-1635.

Solomatov, V.S., 2000. Fluid dynamics of a terrestrial magma ocean. In: Canup, R. M., Righter, K., (Eds.), Origin of the Earth and Moon. University of Arizona Press, Tucson.

Solomon, S., 1979. Formation, history, and energetics of cores in the terrestrial planets. Phys. Earth Planet. Int. 19, 168-182.

Stanley, S., Elkins-Tanton, L. T., Zuber, M. T., Parmentier, E. M., 2008. Mars' paleomagnetic field as the result of a single-hemisphere dynamo. Science 321, 1822-1825.

Stegman, D. R., Jellinek, A. M., Zatman, S.A., Baumgardner, J. R., Richards, M. A., 2003. An early lunar core dynamo driven by thermochemical mantle convection. Nature 421, 143-146.

Sterenborg, M.G., Crowley, J.W., 2013. Thermal evolution of early solar system planetesimals and the possibility of sustained dynamos. Phys. Earth Plan. Int. 214, 53-73.

Stevenson, D.J., Spohn, T., Schubert, G., 1983. Magnetism and thermal evolution of the terrestrial planets. Icarus 54, 466-489.

Stevenson, D.J., 2003. Planetary magnetic fields. Earth Planet. Sci. Lett. 208, 1-11.

Strom, R.G., Schaber, G.G., Dawson, D.D., 1994. The global resurfacing of Venus. J. Geophys. Res. 99, 10899-10926.

Suavet, C. et al., 2013. Persistence and origin of the lunar core dynamo. Proc. Natl. Acad. Sci. U.S.A. 110, 8453-8458.

Suckale, J., Elkins-Tanton, L.T., Sethian, J.A., 2012. Crystals stirred up: 2. Numerical insights into the formation of the earliest crust on the Moon. J. Geophys. Res. 117, E08005.

Sumita, I., Yoshida, S., Kumazawa, M., Hamano, Y., 1996. A model for sedimentary compaction of a viscous medium and its application to inner-core growth. Geophys. J. Int. 124, 502-524.

Takahashi, F., Tsunakawa, H., 2009. Thermal core-mantle coupling in an early lunar dynamo: Implications for a global magnetic field and magnetosphere of the early Moon. Geophys. Res. Lett. 36, L24202.

Tarduno, J. A., et al., 2012. Evidence for a dynamo in the main group pallasite parent body. Science, 338, 939-942.

Tian, B., Stanley, S., Tikoo, S.M., Weiss, B.P., 2014. A precession-driven lunar dynamo. AGU abstract, GP54A-04.

Tikoo, S.M., et al., 2014. Decline of the lunar core dynamo, Earth Planet. Sci. Lett. 404, 89-97.

Tonks, W.B., Melosh, H.J., 1993. Magma ocean formation due to giant impacts. J. Geophys. Res. 98, 5319-5333, doi:10.1029/92JE02726.

Toramaru, A., Fujii, N., 1986. Connectivity of melt phase in a partially molten peridotite. J. Geophys. Res. 91, 9239-9252.

Tosi, N., Plesa, A.-C., Breuer, D., 2013. Overturn and evolution of a crystallized magma ocean: A numerical parameter study for Mars. J. Geophys. Res. Planets 118, 1512-1528, doi:10.1002/jgre.20109.

Touloukian, Y.S., Powell, R.W., Ho, C.Y., Klemens, P.G., 1971. Thermophysical Properties of Matter. Volume 1. Thermal Conductivity - Metal Elements and Alloys. New York: IFI/Plenum.

Treiman, A. H., Gleason, J. D., Bogard, D.D., 2000. The SNC meteorites are from Mars. Planet. Space Sci. 48, 1213-1230.

Tsunakawa, H., et al., 2010. Lunar magnetic field observation and initial global mapping of lunar magnetic anomalies by MAP-LMAG onboard SELENE (Kaguya). Space Sci. Rev. 154, 219-251.

van Keken, P. E., King, S. D., Schmeling, H., Christensen, U.R., Neumeisters, D., Doin, M.-P., 1997. A comparison of methods for the modeling of thermochemical convection. J. Geophys. Res. 102, 22477-22496.

Van Orman, J.A., 2004. On the viscosity and creep mechanism of Earth's inner core. Geophys. Res. Lett. 31, L20606.

Vilim, R., Stanley, S., Elkins-Tanton, L.T., 2013. The effect of lower mantle metallization on magnetic field generation in rocky exoplanets. Astrophys. J. Lett. 768, L30.

Weber, R., Lin, P. Y., Garnero, E., Williams, Q., Lognonne, P., 2011. Seismic detection of the lunar core. Science 331, 309-312.

Weiss, B.P., et al., 2008. Magnetism on the aigrette parent body and the early differentiation of planetesimals. Science 322, 713-716.

Weiss, B.P., Gattacceca, J., Stanley, S., Rochette, P., Christensen, U.R., 2010. Paleomagnetic records of meteorites and early planetesimal differentiation. Space Sci. Rev. 152, 341-390.

Weiss, B.P., Elkins-Tanton, L.T., 2013. Differentiated planetesimals and the parent bodies of chondrites. Annu. Rev. Earth Planet. Sci. 41, 529-560.

Weiss, B. P., Tikoo, S. M., 2014. The lunar dynamo. Science 346, 1246753.

Wetherill, G.W., 1990. Formation of the Earth. Ann. Rev. Earth Planet. Sci. 18, 205-256.

Wetherill, G.W., Inaba, S., 2000. Planetary accumulation with a continuous supply of planetesimals. Space Sci. Rev. 92, 311-320.

Wicht, J., et al., 2007. The origin of Mercury's internal magnetic field. Space Sci. Rev. 132, 261-290.

Wieczorek, M.A., et al., 2006. The constitution and structure of the lunar interior. Rev. Mineral. Geochem. 60, 221-364.

Wieczorek, M.A., Weiss, B.P., Stewart, S.T., 2012. An impactor origin for lunar magnetic anomalies. Science 335, 1212-1215.

Williams, J.P., Nimmo, F., 2004. Thermal evolution of the Martian core: Implications for an early dynamo. Geology 32, 97-100.

Williams, Q., 2009. Bottom-up versus top-down solidification of the cores of small solar system bodies: constraints on paradoxical cores. Earth Planet. Sci. Lett. 284, 564-569.

Williams, J.G., et al., 2014. Lunar interior properties from the GRAIL mission. J. Geophys. Res. Planets 119, 1546-1578. doi:10.1002/2013JE004559

Yang, J, Goldstein, J.I., Scott, E.R.D., 2008. Metallographic cooling rates and origin of IVA iron meteorites. Geochim. Cosmochim. Acta 72, 3043-3061.

Yang, J., Goldstein, J.I., Michael, J.R., Kotula, P.G., Scott, E.R.D., 2010. Thermal history and origin of the IVB iron meteorites and their parent body. Geochim. Cosmochim. Acta 74, 4493-4506.

Young, H.D., 1991. University physics, 8th ed. New York: Addison-Wesley.

Yunker, M.L., Van Orman, J.A., 2007. Inter diffusion of solid iron and nickel at high pressure. Earth Planet. Sci. Lett. 254, 203-213.

Zaranek, S., Parmentier, E.M., 2004. Convective cooling of an initially stably stratified fluid with temperature dependent viscosity. J. Geophys. Res. 109 B3, B03409.

Zebib, A., Schubert, G., Dein, J.L., Paliwal, R.C., 1983. Character and stability of axisymmetric thermal convection in spheres and spherical shells. Geophys. Astrophys. Fluid Dyn. 23, 1-42.

Zhan, X., Zhang, K., Zhu, R., 2011. A full-sphere convection-driven dynamo: Implications for the ancient geomagnetic field. Phys. Earth Planet. Inter. 187, 328-335.

Zhang, Y., 2008. Geochemical kinetics. Princeton University Press.

Zhang, N., Parmentier, E. M., Liang, Y., 2013. A 3-D numerical study of the thermal evolution of the Moon after cumulate mantle overturn: The importance of rheology and core solidification. J. Geophys. Res. Planets 118, 1789-1804.

Zhong, S., McNamara, A., Tan, E., Moresi, L., Gurnis, M., 2008. A benchmark study on mantle convection in a 3-D spherical shell using CitcomS. Geochem. Geophys. Geosyst. 9, Q10017.

Zhong, S., Zuber, M.T., 2001. Degree-1 convection mantle convection and the crustal dichotomy on Mars. Earth Planet. Sci. Lett. 189, 75-84.

Zhong, S., Hager, B.H., 2003. Entrainment of a dense layer by thermal plumes. Geophys. J. Int. 154, 666-676.

Ziegler, L.B., Stegman, D.R., 2013. Implications of a long-lived basal magma ocean in generating Earth's ancient magnetic field. Geochem. Geophys. Geosys. 14, 4735-4742.

Zuber, M., 2001. The crust and mantle of Mars. Nature 412, 220-226.